View metadata, citation and similar papers at core.ac.uk

brought to you by CORE

provided by The Research Repository @ WVU (West Virginia University)

Graduate Theses, Dissertations, and Problem Reports

2000

Development and application electrochemical and spectrophotometric methods based upon AC potential modulation for characterization of hybrid bilayer membranes and electroactive self -assembled monolayers supported on gold electrodes

Dmitri A. Brevnov
West Virginia University

Follow this and additional works at: https://researchrepository.wvu.edu/etd

Recommended Citation

Brevnov, Dmitri A., "Development and application electrochemical and spectrophotometric methods based upon AC potential modulation for characterization of hybrid bilayer membranes and electroactive self -assembled monolayers supported on gold electrodes" (2000). *Graduate Theses, Dissertations, and Problem Reports*. 1228.
https://researchrepository.wvu.edu/etd/1228

This Dissertation is protected by copyright and/or related rights. It has been brought to you by the The Research Repository @ WVU with permission from the rights-holder(s). You are free to use this Dissertation in any way that is permitted by the copyright and related rights legislation that applies to your use. For other uses you must obtain permission from the rights-holder(s) directly, unless additional rights are indicated by a Creative Commons license in the record and/ or on the work itself. This Dissertation has been accepted for inclusion in WVU Graduate Theses, Dissertations, and Problem Reports collection by an authorized administrator of The Research Repository @ WVU. For more information, please contact researchrepository@mail.wvu.edu.

Development and Application Electrochemical and Spectrophotometric Methods Based upon AC Potential Modulation for Characterization of Hybrid Bilayer Membranes and Electroactive Self-Assembled Monolayers Supported on Gold Electrodes

Dmitri A. Brevnov

Dissertation Submitted to the
College of Arts and Sciences at West Virginia University
in partial fulfillment of the requirements for the degree of
Doctor of Philosophy
in Chemistry

Harry O. Finklea, Ph. D., Chair,
Larry E. Banta, Ph. D.,
Fred L. King, Ph. D.,
Ronald B. Smart, Ph. D.,
William J. Wonderlin, Ph. D.

Department of Chemistry
Morgantown, West Virginia
2000

Keywords: AC Voltammetry, Second Harmonic AC Voltammetry, Electrochemically Modulated Electroreflectance, Faradaic Admittance, Kinetics of Heterogeneous Electron Transfer, Melittin, Alkanethiols, Uncompensated Resistance

Copyright 2000 Dmitri A. Brevnov

ABSTRACT

Development and Application Electrochemical and Spectrophotometric Methods Based upon AC Potential Modulation for Characterization of Hybrid Bilayer Membranes and Electroactive Self-Assembled Monolayers Supported on Gold Electrodes

Dmitri A. Brevnov

Applications of the electrochemical method, AC Voltammetry (ACV), and its modifications based upon monitoring *ac* current as a function of *ac* potential modulation are described. The first chapter involves investigating the effect of a short peptide, melittin, on both hybrid bilayer membrane (HBM) dielectric properties and HBM resistance to heterogeneous electron transfer. These effects are discussed in terms of three possible mechanisms by which melittin may affect HBMs. In the second chapter, a modification of ACV, second harmonic ACV, is considered. A data processing method is suggested to analyze data collected at high perturbation frequencies at which the effect of uncompensated resistance cannot be neglected. In the third chapter, application of the spectroelectrochemical modification of ACV, Electrochemically Modulated Reflectance ACV, is discussed. The electromodulation reflectance coefficient, a ratio of *ac* electroreflectance to both DC electroreflectance and *ac* interfacial potential, is shown to be the most useful quantity to represent *ac* electroreflectance data. The same kinetic information on the surface faradaic reactions is available from electrochemical and spectroelectrochemical data. In the final chapter, ACV is applied to determine the rate of electron transfer kinetics for a redox couple attached via short alkanethiols (C_5, C_7, C_{10}) to a gold electrode. The semilog plot of standard rate constant vs. the number of methylene units remains linear down to the shortest used chain length (C_5).

Посвящается моему отцу

Бревнову Анатолию Павловичу

Acknowledgments

The first project reported in this dissertation was initiated in October 96, when a second year graduate student came to the Prof. Finklea's electrochemical laboratory and asked about a possible research project in the area of ion transport across membranes. The answer was "Let's combine my expertise and your interest." I believe that four scientific publications that constitute four chapters of this dissertation are a direct result of this combination. Therefore, I would like to express my gratitude to my adviser, Prof. Harry O. Finklea, for sharing with me his expertise in chemistry and, at the same time, letting me pursue my interests in graduate studies and research.

I would like to thank Prof. Larry Banta for suggesting a topic for my research proposal. Appreciation is also expressed to Prof. William Wonderlin for reviewing my first publication and Prof. Kenneth Showalter for encouraging my application for graduate studies at West Virginia University. In addition, I would like to thank all members of my Committee Profs. Finklea, Banta, King, Smart and Wonderlin for critically reviewing my research proposal and my dissertation.

Finally, I express my thanks to my lab mates Kwansik, Mark, Rich, Rob and Teresa for adding fun in my life and constantly reminding me that being a graduate student does not mean spending all time in a laboratory.

Table of Contents

List of Figures

List of Tables

Table of Abbreviations

ACV	AC Voltammetry
CPE	Constant Phase Element
CV	Cyclic Voltammetry
EIS	Electrochemical Impedance Spectroscopy
EMR ACV	Electrochemically Modulated Reflectance AC Voltammetry
GPIB	General Purpose Instrument Bus
HBM	Hybrid Bilayer Membranes
LIA	Lock-in Amplifier
SAM	Self Assembled Monolayer
SH ACV	Second Harmonic AC Voltammetry

Table of Symbols

α	transfer coefficient,
Γ_{total}	total concentration of adsorbed redox species, (mole/cm^2)
ϵ	HBM dielectric constant,
ϵ_0	dielectric constant of free space,
θ_{red}	electrode coverage of the reduced form of an adsorbed redox couple, (mol)
θ_{total}	total electrode coverage of an adsorbed redox couple, (mol)
X	electromodulation reflectance coefficient in the frequency domain, (V^{-1})
$\chi(E_{dc},\lambda)$	electromodulation reflectance coefficient in the time domain, (V^{-1})
ω	angular frequency, (rad/s)
A	HBM membrane or electrode area, (cm^2)
C	double layer, SAM or HBM capacitance, (F)
C_a	adsorption capacitance for an adsorbed redox couple, (F)
D	diffusion coefficient, (cm^2/s)
d	HBM thickness, (m)
$E^{0'}$	formal potential for an adsorbed redox couple, (V)
$E_{1/2}$	half-wave potential for a freely diffusing redox couple, (V)
E_{dc}	DC potential, (V)
f	perturbation frequency, (Hz)
F	faradaic constant,
k	absorption coefficient,
k^0	standard rate constant for a freely diffusing redox couple, (cm/s)
k_s	standard rate constant for an adsorbed redox couple, (s^{-1})
n	number of electrons transferred in a faradaic reaction,
$\boldsymbol{n}$	the number of methylene units in alkanethiols,
Q	admittance of CPE (Constant Phase Element), (S)
R_a	adsorption resistance for an adsorbed redox couple, (Ω)
R_u	uncompensated resistance, (Ω)
$Y^{faradaic}(\omega)$	faradaic admittance, (S)
$Y^{inter}(\omega)$	interfacial admittance, (S)
$Y^{measured}(\omega)$	measured admitance, the same as total cell admittance, (S)
$Y^{totalcell}$	total cell admittance, the same as measured admittance, (S)
Z_f	faradaic impedance for a freely diffusing redox couple, (Ω)
$Z^{faradaic}$	faradaic impedance for an adsorbed redox couple, (Ω)
φ	faradaic admittance phase.

Introduction

This dissertation consists of four chapters. The emphasis is placed on development and applications of one electrochemical method, AC Voltammetry (ACV), to characterize the dielectric properties of thin organic films, such as hybrid bilayer membranes (HBMs) and self-assembled monolayers (SAMs), and their resistance to heterogeneous electron transfer between either soluble or adsorbed redox couples and gold electrodes to which these films are attached.

In Chapter One, ACV is used to investigate the effect of melittin on the heterogeneous electron transfer across HBMs for three different redox couples. The action of melittin is discussed in terms of three possible mechanisms including the formation of channels and large pores. Since ACV is not capable of providing the desired spatial resolution to characterize sub-micro scale pores in HBMs, a modification of ACV, Second Harmonic ACV (SH ACV) is examined in Chapter Two in order to establish the potentiality of this method to improve the spatial resolution. At high frequencies necessary to extract a higher spatial resolution, the faradaic admittance, $Y^{faradaic}$, measurements by SH ACV are distorted by the effect of non-faradaic elements. Although a data collection and processing method is suggested to obtain $Y^{faradaic}$ in the presence of the non-faradaic elements, the complexity of this method outweigh the amount of new kinetic information. Therefore, SH ACV was not further investigated in this dissertation.

Chapter Three deals with another modification of ACV, Electrochemically Modulated Electroreflectance ACV (EMR ACV), which is a spectrophotometric method

also based upon *ac* potential modulation. EMR ACV is shown to result in the same kinetic information as ACV for an electroactive SAM, when a ratio of *ac* electroreflectance to DC electroreflectance is normalized the interfacial *ac* potential. EMR ACV may be superior to ACV in separating two faradaic processes that occur at the same thermodynamic and kinetic scales. However, for the simple one electron faradaic reaction for the redox couples covalently attached to gold electordes, ACV is a less instrumentally complex method to obtain $Y^{faradaic}$ information. Thus, ACV is exclusively used in Chapter Four to investigate the rate of heterogeneous electron transfer as a function of chain length for short chain alkanethiols.

Chapter One

AC Voltammetry studies of the effect of melittin on heterogeneous electron transfer across a hybrid bilayer membrane (HBM) supported on a gold electrode.

1. Review of the phospholipid bilayer membranes supported on solid surfaces

Various model membrane systems have been used in the past to study the physical properties of cellular membranes. Among them, phospholipid or hybrid (phospholipid / alkanethiol) bilayers supported on flat inorganic solids have recently attracted a lot of attention.[1] In contrast to other planar model membranes, they are much less fragile and have longer life time (from days to weeks). In addition, the proximity of the conducting or insulating support surface enables the application of several surface-sensitive techniques: ellipsometry, surface plasmon spectroscopy, impedance spectroscopy, Fourier Transform infrared spectroscopy and others.

Bilayer membranes supported on solids are of scientific and practical interest for several reasons.[1] First, they provide a natural environment for the immobilization of proteins under non-denaturing conditions. Therefore, the function of the membrane proteins can be studied under conditions close to those existing in the cellular membrane. Second, electrical, optical or piezoelectrical detection of ligand binding to the receptors incorporated in the membrane can be used for the biosensor design.

A biosensor is an analytical device that combines a biological or biologically derived sensing unit with a transducer, which converts the sensing event to a signal.[2]

Although the biosensors including the phospholipid membranes have been the focus of a lot of research for many years, a practical device has been reported only recently.[3] This biosensor consists of the bilayer phospholipid membrane tethered to a gold support with a well-defined ionic reservoir between the membrane and the support. The conductance of the ionic channels formed by gramicidin is switched on or off by the presence of analytes. Two deals between pharmaceutical companies and Australia's Cooperative Research Center for Molecular Engineering and Technology at which this biosensor was developed indicate that this device may have a bright future.[4]

Three types of supported membranes[1] can be generally assembled: (i) bilayers with the inner monolayer fixed to the support, (ii) freely supported bilayers separated from the support by ultrathin water layers, and (iii) bilayer membranes resting on ultrathin, soft hydrated polymer films. The second type has a great advantage since it provides the aqueous reservoir between the support and the bilayer similar the natural conditions for the membrane proteins.

Three approaches have been used to assemble the supported bilayer of the second type. The first is based upon the electrostatic interaction between the charged monolayer adsorbed on the gold electrodes and the oppositely charged polar head groups of the inner layer of the bilayer membranes.[5] The second approach has been developed by a group at the University of Leeds.[6,7] A synthetic molecule composed of the three units (a thiol group for self-assembly on gold, a short chain ethyleneoxy derivative to provide a hydrophilic region between the membrane and a gold support, and a cholesterol derivative, which inserts and "anchors" the bilayer) has been used in this project. The

third approach has been used by the above mentioned Australian group.[3] A synthetic lipid performing the same three roles (attachment to a gold surface, control of the aqueous space and anchoring the bilayer membrane) has been employed to create a prototype for the biosensor.[8]

Although the supported bilayer membranes separated from the solid support by the aqueous reservoir have a great scientific and practical potential in biomimetic chemistry and biophysics, the bilayer membranes with the inner layer being fixed on a support have also been a subject of intensive investigation. They may consist of two different layers (alkanethiols and phospholipids); in this case, they are usually called hybrid bilayer membranes (HBMs). Research projects involving the electrochemical application of HBMs can be divided in two major groups.

The first group deals with the immobilization of the electrochemically active proteins into HBMs, with the electron transfer between the redox sites in these proteins and the metal electrodes occurring either directly or via a mediator. For example, Hawkridge published papers on cytochrome *c* immobilized in the HBMs that "is able to directly transfer electrons with the electrode and to mediate electron transfer between solution resident cytochrome c, its native redox partner, and the electrode".[9] Laval reported that " *Escherichia coli* pyruvate oxidase (Pox), a peripheral membrane enzyme, was incorporated into the supported bilayer."[10] The enzyme activity "was detected by the electrocatalytic current produced when substrate and the electron acceptor, ferricinium methanol, were present in solution". In order to provide the reversibility of ferrocene electrochemistry, artificial defects were introduced into the supported bilayer membrane.

In the second group, ion channel forming peptides are inserted into HBMs, thus allowing the modification of the HBM permeability. Fritsch described a strategy for incorporating Gramicidin D in the HBMs.[11] Seifert reported adsorption of vesicles containing the ion translocating proteins, such as bacteriorhodopsin, Na,K-ATPase, H,K-ATPase and Ca-ATPase on the gold electrode coated with alkanethiols.[12] It was shown that bacteriorhodopsin incorporated in HBMs generates current transients upon the light illumination. Dong reported incorporation of a naturally existing antibiotic compound, monensin, in the HBMs and demonstrated that the selectivity order for alkali-metal ions is $Na^+ > K^+ > Rb^+$.[13] Plant published papers on the effect of melittin on the HBMs electrical properties.[14,15] Her work will be discussed later in section 3. Vogel described incorporation of ganglioside in HBMs and its interaction with cholera toxin.[16] The binding events were detected by Impedance Spectroscopy and Surface Plasmon Resonance Spectroscopy.

The driving force behind the protein incorporation in HBMs is the potential applicability of these HBMs in biosensor design. The most significant sensitivity limitation of the biosensor design results from the relatively small amount of energy associated with molecular (ligand-receptor) interactions, which indicates that many binding events are necessary to provide a useful signal.[17] This limitation in signal magnitude can be overcome by allowing the chemical interaction to modulate a large amount of supplied or stored energy. For example, the energy stored in the living cells as a transmembrane potential can be dissipated as a response of a single molecule binding

with the membrane proteins. Although the magnitude of this interaction is small, it results in a very high flux of ions across the membrane (up to million ions per second). This type of amplification is at the heart of the biological systems and has been proposed for design of artificial biosensors capable of detecting picomolar concentrations.

The research project reported in Chapter One of this dissertation involves the design and electrochemical characterization of HBMs. Therefore, the methods for their construction and the electrochemical methods used for their characterization will be considered in more detail.

1.1. Methods for deposition of bilayer membranes with the inner layer being fixed on a support

Two basic deposition procedures have been reported. In the Langmuir-Blodgett procedure, a monolayer of amphiphilic molecules is transferred from the water-air interface to a solid slide when it is either immersed or withdrawn from a solution.[18] If the slide surface is initially hydrophilic, the emersion results in the polar groups of the monolayer being attached to the slide. The second immersion differs from the first in that the slide is now hydrophobic, and the second monolayer is attached with the polar group oriented in the opposite direction to the polar group in the first layer. This technique has certain drawbacks regarding the incorporation of proteins into the membrane. They do not tolerate being transferred into monolayers where some of their domains may become directly exposed to air.

The second procedure involves the deposition of a layer of alkanethiols on the gold surface.[19,20] Thiols are known to adsorb spontaneously on the noble metal surfaces with a result being a well organized system: self-assembled monolayers (SAMs). The hydrophobic surface of a SAM is used next to deposit the second layer consisting of phospholipids. Deposition can be done by either the liposome fusion method[21] or the painting method.[22,23] In the first method, a solution containing liposomes (vesicles formed by phospholipid bilayers dispersed in aqueous media) is added to the solution containing the electrode with a SAM. The liposome fusion results from the thermodynamically favorable interactions between the alkyl chains of the alkanethiols and the phospholipid molecules. The liposome fusion may also be initiated by osmotic stress if the aqueous solution used for liposome preparation has a higher ionic strength that the solution in which fusion takes place. In the second method, a drop of organic solvent containing phospholipids is painted on the electrode with a SAM. The membrane produced after evaporation of the solvent contains an unknown amount of organic solvent. Both methods result in a supported HBM.

1.2. Electrochemical methods used for the hybrid bilayer membrane characterization

Different spectroscopic, microscopic and surface science methods have been used to follow the formation and to characterize HBMs. This review will be restricted only to the electrochemical methods. They can be divided into two categories. The first category

employs the correlation between the interfacial capacitance and the membrane thickness and dielectric constant. This group of methods provides only a generic picture of the membrane dielectric properties. In the second group of methods, faradaic reactions (i.e., heterogeneous electron transfer between soluble redox couples and the metal electrodes) are used to characterize the membrane insulating properties on the micro scale.

If no faradaic reactions takes place, a simple electrical circuit model for the electrode modified with the HBM is a series combination of the uncompensated resistance (R_u) and the membrane capacitance (C). This capacitance can be found by either the slow scan cyclic voltammetry (CV) or low frequency electrochemical impedance spectroscopy (EIS). The second technique enables one to detect the deviations in the interfacial properties from the pure capacitor behavior more easily. It is usually appropriate to substitute the capacitive model ($Y=j\omega C$) with a more realistic model of the constant phase element (CPE) ($Q=Q_0(j\omega)^{\chi}$, where Y and Q are capacitor and CPE admittances, ω is angular frequency, χ is less than 1 and Q_0 is the pre-exponential factor analogous to the double layer capacitance C). Although the experimental data do not always fit to the simple model (R_uC), the measured capacitance is often used to find the thickness of the dielectric film according to the following formula, if some knowledge exists about the membrane area (A) and the membrane dielectric constant ϵ:

$$d=\epsilon\epsilon_o A/C \qquad (1.1)$$

where ϵ_o is the dielectric constant of free space and *d* is the membrane thickness.

The hybrid bilayer structural micro defects can be probed by using the faradaic reactions. The interpretation of these experiments (mainly Cyclic Voltammetry (CV) and Electrochemical Impedance Spectroscopy (EIS) done at the formal potential of a redox couple) is relatively complicated because of the following reasons. The gold electrode with HBMs most closely resembles a micro or nano array electrode with the membrane defects corresponding to the active sites. Therefore, nonlinear diffusion toward these sites has to be considered for the valid interpretation of electrochemical data. A model for the microarray electrode and its characterization by means of EIS has been proposed by Finklea and Rubinstein.[24] The paper also describes how to interpret linear scan voltammograms using the same model. Three parameters of this model are R_a, the radius of the microelectrode site, R_0, the radius of the inactive area and θ, the coverage of the blocking layer. When 1- θ is small (less than 0.1), then

$$1 - \theta = R_a^2/R_0^2 \qquad (1.2)$$

The important contribution of this model is its capability of discriminating three frequency regions. The high-frequency case corresponds to isolated diffusion profiles for each active site. At the intermediate frequency region, there is a partial overlap of the diffusion layers between individual microelectrodes that becomes complete at the low frequency case. Given EIS data measured over a wide range of frequencies, it is possible to calculate the three microarray electrode parameters under the assumption of uniform

active site distribution. The typical R_a values obtained by this method are 1-10 um in SAMs of dodecanethiols on gold.

At the same time, a typical premise in electrochemical characterization of microarray electrodes is that the redox couples such as $Ru(NH_6)^{+2/+3}$ and water-soluble ferrocene derivatives demonstrate reversible kinetics on a bare Au electrode, with the charge transfer resistance being calculated from the theory. Unfortunately, adsorption either of an oxidized or reduced form, which is believed to be necessary for the fast heterogeneous electron transfer,[25] has been mostly ignored in previous studies. Thus, it is possible that the faradaic process cannot be modeled as a simple equivalent circuit containing the Warburg Impedance element and charge transfer resistance element. Consequently, the rate of the faradaic reaction is faster than that corresponding to the assumed charge transfer resistance. As a result, underestimation of the electron transfer rate may lead to overestimation of the size of the HBM defects, since diffusion to HBM pinholes and the electron transfer may be considered as two processes occurring sequentially. An analogous situation existed in electrochemical kinetics when the rates of homogeneous reactions were determined from the CEC (Chemical Electrochemical Chemical) mechanism under the assumption of the faradaic process reversibility.[26] The underestimation of the faradaic reaction rate leads to higher estimates of the homogeneous rates than those determined by nonelectrochemical methods.

In conclusion, both the capacitance and faradaic admittance measurements provide useful information on the HBM electrical properties. However, the combined use of different electrochemical, spectroscopic or microscopic methods would produce a

better picture of the HBM physical properties.

1.3. Review of prior electrochemical characterization of HBM

Offenhausser performed the capacitance measurements by means of EIS in order to follow the sequential formation of SAM and HBM.[27] The impedance data at high frequencies were modeled as a simple series R_uC circuit. Data at low frequencies that could not be analyzed in term of the R_uC circuit were ignored. The SAM and HBM specific capacitances were used to determine the thickness of the dielectric medium. The reported specific capacitance of a $C_{11}H_{23}SH$ SAM was about 1.3 uF/cm^2. The specific capacitance of the lipid layer was calculated to be 1.4 uF/cm^2 according to the following formula:

$$C_{lipid}^{-1} = C_{HBM}^{-1} - C_{SAM}^{-1} \tag{1.3}$$

This formula assumes that two layers of the HBM act as two capacitors in series. The structural defects of the samples were examined by heterogeneous electron transfer between ferrocenecarboxylic acid and the gold electrode by means of CV. Although no EIS data was reported in the presence of the faradaic process, the HBM was claimed to be "essentially free of measurable pinholes" if the length of the alkane chains of alkanethiols exceeded 7 methylene units.

Dong characterized the HBM by means of EIS at the presence of equal amounts of

both ferri/ferrocyanide at the formal potential of this redox couple.[23] The equivalent circuit model used for the data analysis was $R_u(RQ)$, where (RQ) is a parallel combination of the membrane resistance and CPE. The specific resistances of these HBM were claimed to be in the usual range for the bilayer lipid membranes. However, it is necessary to stress that "the charge transfer resistance of any electrochemical reaction at a membrane-coated electrode is not equivalent to the resistance of the membrane itself"[28], which is defined as the resistance toward the non-electrochemically active ion flux driven by the electrochemical potential gradient. Table 1.1 summarizes the most typical results obtained with the HBMs.

Table 1.1. Electrochemical properties of HBMs.

Author	Specific Capacitance uF cm^{-2}	Electrolyte composition	Specific Resistance Ohm cm^{-2} at E_{dc} (V) vs. Ag/AgCl	Redox couple
Dong[23]	0.5	0.5 M KCl	$7*10^8$ at 0.22	5 mM of both $Fe(CN)_6^{-3}$ and $Fe(CN)_6^{-4}$
Plant[14,15]	1.0	150 mM NaCl	$5*10^6$ at −0.55	1mM of $Fe(CN)_6^{-3}$
Offenhausser[27]	0.7	0.1 M NaCl	n/a	
Fritsch[11]	2.8	0.1 M KNO_3	n/a	

Gaub performed the electrochemical characterization of both SAMs and HBMs by

CV with ferrocyanide.[22] The results and conclusions were similar to those reported by Offenhausser. In particular, the effective suppression of the faradaic currents was observed. Tunneling via the HBMs was claimed to be the mechanism of the electron transfer via the HBMs.

Both Vogel[16] and Sackmann[29] reported HBM characterization by EIS in the absence of the faradaic reactions. More complicated equivalent circuits, such as $R_u(RQ)(RQ)$, were used for data analysis over the whole investigated frequency range. Despite a better fit of the experimental data to the suggested equivalent circuits, the physical origins of all circuit elements is not absolutely clear. A possible explanation is that each parallel combination of a resistor and CPE corresponds to one dielectric layer in the HBMs.

2. Review of the state of mellitin in solution and its effect on electrical properties of HBM

The emphasis in this research project is placed on modification of the HBM electrochemical properties upon addition of melittin. Therefore, the state of melittin in solution and its interaction with the cellular membranes are considered in more detail.[30,31]

A 26 aminoacid peptide, mellitin, is a major component of the venom of the European honey bee *Apis mellifera*. The voluminous research on melittin has been reviewed by Dempsey.[30] Extensive quotes are given from this review to describe the state of melittin in solution and its action on membranes.

" ... numerous studies have been undertaken to determine the nature of the interaction of mellitin with membranes, both with the aim of understanding the molecular mechanisms of mellitin-induced hemolysis and as a model for studying the general features of the structures of membrane proteins and their interaction with lipids in membranes. It is probably uncontroversial to state that the mechanism of membrane lysis has been proven and that there is no consensus on the nature of interaction of mellitin with membrane lipids... A reason, more specific to mellitin, is that the peptide has several actions on membranes and these activities are not necessarily related; mellitin may interact with membranes in different ways, depending on the lipid composition of the bilayer, peptide concentration, bulk solution pH, the presence or absence of a membrane potential, and the hydration level of the bilayer. In addition to its hemolytic activity, mellitin induces voltage-dependent ion-conductance across planar lipid bilayers."

"In common with other membrane-binding peptides and membrane proteins, melittin is predominantly hydrophobic." Because of its basic groups, "the peptide has a net charge of +6... Despite its high proportion of hydrophobic side-chains, melittin is very soluble in water" and may adopt "different conformations and aggregation states depending on several factors including peptide concentration, pH, ionic strength and the nature of the negative counterion. Depending on the factors listed above, melittin is either monomeric in water or associated as a tetrameric aggregate."

"The conformational and aggregational properties of melittin in water result from two opposite forces; promoting self-association is the hydrophobic effect that acts to sequester non-polar amino acids in the interior of proteins (or molecular aggregates) and opposing self-association are the high positive-charge density of melittin and the entropic term associated with the formation of secondary structure in the self-associated tetramer. Factors that suppress charge strongly promote self-association. High ionic strength and addition of the phosphate buffer lead to self-association. Likewise, titration of the amino groups of melittin by increasing pH results in suppression of positive charge density and promotes self-association of melittin."

"The characteristic effect of melittin on cell membrane is its hemolytic activity. At concentrations of 1ug/mL (0.3 uM) and higher melittin binds rapidly to erythrocytes and induces the release of hemoglobin into extracellular medium. It has been shown that the binding of melittin to erythrocytes as a monomer is necessary for the expression of hemolytic activity. Phosphate suppresses hemolysis to an extent that correlates with its effect on inducing tetramerization of melittin; complete suppression of hemolysis occurs at 0.5 M phosphate."

In addition to its hemolytic activity, "in black lipid membrane, melittin induces conductance changes in response to an applied potential when the potential is negative on the opposite side of the membrane to which melittin is added. The voltage-dependent increase in conductance is consistent with the formation of channels allowing ion migration, in response to a voltage-dependent reorientation of melittin in the membrane. The ability of melittin to induce enhanced ion permeability" has been proposed as "a plausible mechanism for hemolysis by the colloid osmotic mechanism."

In conclusion, "there is considerable interest in the mechanism of melittin-induced hemolysis. Hemolysis results from the perturbation of bilayer lipid organization due to the presence of the amphipathic helix in the head group region of the bilayer, or due to the formation of ion-permeable channels in the manner of the voltage-gated 'pore'." The third explanation is that hemolysis maybe "a result of the ability of the peptide to micellize discs of membranes leaving holes through which the cell contents may diffuse. Each of these mechanisms is consistent with an osmotic lysis mechanism as long as the initial perturbation results in enhanced permeability to ions (and water) before release of intracellular hemoglobin".

3. Review of Plant's work on the effect of melittin on HBM

The research project reported in the first chapter of this dissertation was initiated in November 96, after Prof. Finklea and the author had visited the Biotechnology Laboratory (Biomolecular Materials) at National Institute of Standards and Technology and talked to the group leader Dr. Plant. One of Plant's research project was aimed at the study of the effect of melittin on the electrical properties of a HBMs.[14,15] Fusion of the phospholipid vesicles to alkanethiol monolayers on gold was used to create the HBM. The electrochemical characterization of SAMs and HBMs was performed by means of CV and EIS. A lower value of the HBM specific capacitance in comparison than that of a SAM was indicative of deposition of the second dielectric layer. In addition, it was

shown that the heterogeneous electron transfer between $Fe(CN)_6^{-3/-4}$ and the gold electrode via the HBM was highly attenuated and was claimed to occur by a tunneling mechanism because of the exponential dependence of the charge transfer resistance vs. overpotential. Plant reported the HBM electrochemical characteristics under the following conditions: the working electrode area 0.32 cm^2, electrolyte composition 20 mM Tris, 150 mM NaCl, 5 mM EDTA, pH 7.4. The HBM resistance measurements were performed with 1 mM $Fe(CN)_6^{-3}$ in 1 M KCl at −0.55 V vs. Ag/AgCl reference electrode.

Table 1.2. Plant's SAM and HBM electrochemical properties.[15]

Layer	Resistance (MΩ)	Specific capacitance (uF/cm^2)
Decanethiol	0.11±0.1	1.6±0.1
Decanethiol+PhLipid (C18)	1.5±0.2	1.06±0.01
Decanethiol+Lipid+melittin	0.11	1.05

The major emphasis in Plant's papers was placed on the effect of melittin on the HBM electrical properties. It was determined by CV and EIS that melittin dramatically enhances the heterogeneous electron transfer across HBM between anionic $Fe(CN)_6^{-3/-4}$ in a Tris buffer and the gold electrode. "Cyclic Voltammetry shows that the rate of electron transfer through the bilayer is greatly increased, approaching the magnitude of the current that is observed for the monolayer".[15] EIS data collected at significant overpotentials (more than 500 mV negative with respect to the formal potential) suggested that the HBM equivalent circuit is a parallel combination of the membrane capacitance and the charge

transfer resistance (the membrane resistance according to the terminology used by Plant). In contrast, after the melittin addition, the charge transfer process could not be modeled as a resistor. A capacitive component suggested that the charge transfer is partially limited by the diffusion-controlled transport of $Fe(CN)_6^{-3/-4}$ to the HBM defects.

At the same time, "incubation of melittin with the bilayer in the presence of a high concentration of phosphate ion resulted in little increase in the $Fe(CN)_6^{-3/-4}$ response." It was found that "the capacitance of the bilayer was not significantly affected by addition of mellitin" and that "these bilayers are sufficiently flexible to accommodate the pore-forming protein". Plant's research project was limited to a single redox couple and the interpretation of EIS data did not allow her to make a definite conclusion on the melittin action on the HBM. In the discussion section, Plant wrote that "it is possible that with further analysis, these data [EIS data on HBM in the presence of melittin] may provide information on the diffusion-controlled transport of electroactive ions in the membrane in the presence of a pore-forming protein."

4. Development and application of AC Voltammetry (ACV)

Although many electrochemical techniques have been developed to obtain quantitative information on electrode processes, those employing the sinusoidal type perturbation have a number of instrumental and data processing advantages. The corrections for both the limited bandwidth of the potentiostat power amplifier and the

electrochemical cell time constant associated with the uncompensated resistance and the double layer capacitance can be performed more easily in the frequency domain than in the time domain. In addition, the lock-in amplification enables one to limit the signal bandwidth to a single frequency and, thus, improve the signal-to-noise ratio. Finally, with the sinusoidal perturbation, the theory of electrochemical processes becomes relatively simple.

In a typical experiment, a small amplitude ac potential perturbation $/V/\sin(\omega t)$ is superimposed with a DC potential. Thus, there are two techniques: Electrochemical Impedance Spectroscopy (EIS), when ω is varied and the DC potential is kept constant, and AC Voltammetry (ACV), when ω is constant and the DC potential is linearly scanned or stepped in a predetermined way. Therefore, these two techniques may be considered to provide two orthogonal slices on the four dimensional plot with the impedance data being a function of two independent variables: thermodynamic - the DC potential, and kinetic - the angular frequency ω.

EIS has been well developed and is very common. The optimization programs (for example, Equivalent Circuit®) are used to obtain the optimum fit of the measured EIS data to a model circuit. This electrochemical method allows one to separate electrode processes occurring with different time constants at the same DC potential. In many cases, however, the processes that constitute the total faradaic reaction tend to occur at slightly different DC potentials. For example, the charge transfer process may be preceded or followed by adsorption of reduced or oxidized forms. As a result, the charge transfer and adsorption processes may be separated on the DC potential scale by 50-100

mV and EIS data collected at a single DC potential may tend to be overweighted toward only one process. Some uncertainty, therefore, exists with the accurate determination of all faradaic process components by this method.

ACV affords a better way to analyze the complicated faradaic processes. In particular, corrections for both R_u and interfacial dielectric properties do not require any assumption of an equivalent circuit corresponding to the faradaic process. Therefore, any peculiarities of the faradaic process (e.g., adsorption of freely diffusing, electrochemically active species, kinetic heterogeneity for the strongly adsorbed redox couples) may be more easily detected by this method. The development and applications of ACV and its modifications (Second Harmonic ACV and Electrochemically Modulated Reflectance ACV) will be reported in this and following chapters.

5. Objectives of this research project

The overall goal of this project is to investigate the effect of melittin upon both the HBM capacitance and the heterogeneous electron transfer of three selected redox couples across the HBM by means of AC Voltammetry (ACV). ACV was chosen as the electrochemical method because of the wealth of information it provides on both non-faradaic and faradaic processes. The selected redox reactants include a cationic species, $Ru(NH_3)_6^{3+}$, a neutral species, hydroxymethylferrocene, $FcCH_2OH$, and an anionic species, $Fe(CN)_6^{3-}$.

The deposition of the SAM of dodecylthiol and the sequential deposition of the

second phospholipid layer, via the vesicle fusion, result in the formation of a low dielectric constant barrier, a hybrid bilayer membrane (HBM), which greatly attenuates the heterogeneous electron transfer from kinetically fast redox species ($Ru(NH_3)_6^{3+}$ and $FcCH_2OH$) and a redox couple that demonstrates quasi-reversible kinetics ($Fe(CN)_6^{3-}$). The electrochemical properties of HBM, capacitance and charge transfer impedance, are modified by the addition of melittin. Because of the high positive charge on melittin, electrostatic attraction of $Fe(CN)_6^{3-}$ towards the HBM could account for the enhanced permeability of the HBM in the presence of melittin. This research project was initiated in order to probe this issue.

6. Experimental Section

Chemicals. 1-Dodecanethiol ($C_{12}H_{25}SH$) was purchased from Aldrich. 1,2-Dioleoyl-*sn*-glycero-3-phosphocholine was purchased from Avanti Polar-Lipids, Inc. Melittin was purchased from Sigma. All chemicals were used as received.

Preparation and pretreatment of gold electrode. The gold rod electrode was prepared by melting pieces of gold wire in a cylindrical crucible and letting the melt cool down slowly. One end of the gold electrode was oriented in a holder via X-ray back-scattering and polished with alumina powders in order for the polished surface to have predominantly the Au(111) crystallographic orientation. The geometric electrode area was circa 0.1 cm^2. Two electrode cleaning procedures were used before the deposition of SAMs. The first procedure involved electrode oxidation with a controlled current density

of 0.1 A/cm^2 in a dilute solution of $HClO_4$. The resulting brown gold oxide coating was stripped in a dilute solution of HCl in a sonicator. Finally, the electrode was heated in a gas-air flame. In the second procedure, the gold electrode was treated with a hot (100 °C) mixture of 30% H_2O_2 and H_2SO_4 *(caution!)* and subsequently heated in a gas-air flame. The cleanliness of the gold electrode was established by performing a CV experiment in dilute H_2SO_4. The sharp current rise at about +1.1 V vs. SCE corresponding to the formation of a gold oxide was indicative of the clean electrode surface.

Hanging meniscus configuration, electrochemical cell and electrolyte composition. The hanging meniscus configuration was chosen in order to define the contact area of the gold electrode without the use of insulation or o-rings.[32] A standard three-compartment electrochemical cell was used in all experiments. A high surface area platinum mesh counter electrode and a SCE reference electrode were used. To minimize R_u, a quasi-reference platinum wire electrode was positioned close to the meniscus. The quasi-reference electrode was connected parallel with the SCE via a 2 µF capacitor. The gold electrode was immersed in the electrolyte solution and slightly pulled up in order to create the hanging meniscus configuration. Thus, only the predominantly single crystal gold surface was in contact with the electrolyte. For all electrochemical measurements and vesicle preparation, the electrolyte solution was 0.15 M NaCl, 5 mM EDTA, 20 mM TRIS, pH 7.1 (adjusted with HCl). The purpose of EDTA was to suppress phospholipase activity in the melittin mixture. The concentration of either $Ru(NH_3)_6^{3+}$ or $Fe(CN)_6^{3-}$ was 1 mM in all experiments. Due to a limited solubility of $FcCH_2OH$, its concentration was about 0.2 mM.

Deposition of SAM and HBM. The cleaned gold electrode was immersed overnight in a 0.05% solution of 1-dodecanethiol in hexane. Before being immersed in the aqueous electrolyte, the gold electrode was rinsed with hexane and dried in a stream of argon to remove residual hexane. After electrochemical characterization of the SAM, a solution of phospholipid vesicles was added to the cell. The vesicles were prepared according to the following procedure.[15] A few mL of phospholipid solution (10 mg/mL) in chloroform was placed in a test tube and the chloroform was evaporated under a stream of Ar. The sample was then placed under vacuum for several hours to remove residual chloroform. The film of phospholipid was resolubilized in 50 µl of isopropanol. This solution was injected into 1 mL of the electrolyte solution with vigorous agitation. The resulting translucent solution was injected into the electrochemical cell. The deposition of the second layer was performed overnight with the gold electrode being constantly immersed in the solution. Before HBM characterization, excess vesicles were washed away with the fresh electrolyte solution. Melittin was added to the electrochemical cell with a final concentration of 1-5 µM. Before electrochemical measurements, melittin was allowed to equilibrate with HBMs for 1-2 hours. At no point was the gold electrode face with a HBM allowed to leave the electrolyte. This proved to be a particular problem in the hanging meniscus configuration. Loss of wetting contact resulted in loss of the phospholipid layer (as determined by capacitance measurements).

Experimental Setup for electrochemical experiments: data collection and processing.

EIS experiments were performed using an EG&G M273 potentiostat and an

EG&G 5210 Lock-in Amplifier (LIA) controlled via the GPIB interface with EIS M398 software. No software calibration was used to correct for the limited bandwidth of the I/E converter. EIS was mainly used to find the uncompensated resistance at frequencies between 10 kHz and 100 kHz.

Because of the requirement of sampling both the cell *ac* voltage and *ac* current and the availability of only a single input channel on the LIA 5210, ACV experiments were performed with a second LIA 5210. The potentiostat was programmed from the front panel to apply a DC potential scan of 10 mV/sec. One of the LIAs generated the *ac* potential which was applied to the *ac* input on the rear panel of EG&G M273 and, at the same time, provided a phase-locked TTL signal to drive the second LIA. A typical total cell *ac* potential was 5 mV rms. Both the *ac* potential and the *ac* current measurements were performed in respect to the same reference phase. The time constants on LIAs were set to 30 ms; a higher time constant resulted in electrochemical data convoluted with the frequency response function of the lowpass filters. A data acquisition board CIO/DASH 16/330 and a signal conditioning board CIO-SSH16 (Computer Board) together with a Quick Basic® program were used to sample five channels: the DC potential, and the real and imaginary parts of both the *ac* current and the *ac* potential. More than 1000 samples were collected and averaged in a period of 0.1 second to generate a single point.

ACV data are reported in three formats. The first is the total cell admittance, *Y*, (the ratio of *ac* current to *ac* potential) as a function of DC potential. The second is the interfacial admittance vs. DC potential. The interfacial admittance is calculated as the reciprocal value of the total cell impedance minus the uncompensated resistance (R_u).[33]

In the third format, data are represented as the faradaic admittance vs. DC potential. The faradaic admittance is calculated as the interfacial admittance minus the CPE admittance. The CPE admittance is found by the first or second-order extrapolation of the interfacial admittance from a DC potential before the faradaic wave to a DC potential after the faradaic wave. This procedure is applied to both the real and imaginary parts of the interfacial admittance.

The last electrochemical method employed in this research project, cyclic voltammetry, was performed with the EG&G M273 potentiostat and Headstart® software.

7. Results and Discussion

7.1. ACV results for the bare gold electrode

The ACV behavior of the three selected redox couples on the bare gold electrode are examined first to assess their kinetic and adsorptive behavior. Figure 1.1 demonstrates the total cell admittance, the interfacial admittance and the faradaic admittance for 1 mM $Ru(NH_3)_6^{3+}$ at 100 Hz. Slight hysteresis between the forward and reverse scans is attributed to slow reconstruction processes on the gold electrode surface.[34] The shapes of the faradaic admittance peaks can be modeled as a single hyperbolic function.[35] If the faradaic process is *ac* reversible, both the real and imaginary parts are proportional to $1/cosh^2(0.5 \times RT(E_{dc} - E_{1/2})/(nF))$, where all variables have their

usual electrochemical meanings. The frequency dependence of the faradaic admittance phase can be used to determine the standard rate constant. For $Ru(NH_3)_6^{3+}$ with the electrolyte composition as specified in the experimental section, the real and imaginary parts are approximately equal to each other up to 1 kHz. The phase, which is defined as *arctan(imag(Y)/real(Y))*, is close to 45°. This behavior is indicative of the *ac* reversibility of this faradaic process over this frequency range.[35] At higher perturbation frequencies, the faradaic admittance data become very sensitive to small variations of R_u and, therefore, are not sufficiently reliable for kinetic analysis.

Figure 1.2 demonstrates the interfacial admittance for the neutral $FcCH_2OH$. The shape of the faradaic wave is distorted in a manner indicative of neutral ferrocene adsorption. There is a shoulder in the imaginary part of the faradaic admittance at potentials positive of the half-wave potential (+0.19 V). However, like $Ru(NH_3)_6^{3+}$, the ferrocene faradaic reaction is *ac* reversible at 100 Hz. The faradaic admittance phase is approximately 45°. Similar to the faradaic reaction for $Ru(NH_3)_6^{3+}$, faradaic admittance data collected at perturbation frequencies higher than 1 kHz are not reliable for kinetic analysis.

In contrast to both of these redox couples, the phase of faradaic admittance for $Fe(CN)_6^{3-}$ determined at the same frequency and with the same electrolyte is significantly less than 45°. Despite some uncertainty about the correction for the double layer admittance (not shown in Figure 1.3), the real part of the faradaic admittance is noticeably larger than the imaginary part. The qualitative conclusion is that the rate of this faradaic reaction is substantially slower than that of $Ru(NH_3)_6^{3+}$. In addition, the shape of the

faradaic wave is distorted and a single hyperbolic function can no longer be used to model both components of the faradaic wave. This fact complicates quantitative determination of the standard rate constant.

The overall conclusion from ACV experiments on the bare gold electrode is that both faradaic reactions for $Ru(NH_3)_6^{3+}$ and $FcCH_2OH$ are *ac* reversible up to 1 kHz and are faster than that for $Fe(CN)_6^{3-}$ which is *ac* quasi-reversible. Due to dependence of the faradaic process upon adsorption of both the non-electrochemically and electrochemically active species, this conclusion is only valid for the chosen electrolyte conditions. The kinetic status of the faradaic reactions is usually sensitive to variations in electrolyte composition. For example, a decrease in pH from 7.1 to 6.1 slows down the faradaic process for $Ru(NH_3)_6^{3+}$. This fact manifests itself as a decrease of the faradaic admittance phase from 45° to a lower value and the faradaic process becomes *ac* quasi-reversible.

7.2. ACV results for SAMs and HBMs

The interfacial admittances for $Ru(NH_3)_6^{3+}$, $FcCH_2OH$ and $Fe(CN)_6^{3-}$, respectively, are demonstrated for SAMs (Figures 1.4A, 1.5A, 1.6A) and HBMs (Figures 1.4B, 1.5B, 1.6B). The sequential deposition of SAMs and HBMs decreases the interfacial admittance at DC potentials where no faradaic reaction takes place. At high frequencies, the dielectric barrier can be modeled as a pure capacitance, whereas, at low frequencies, a more appropriate model is the CPE. Despite this complication, the interfacial specific capacitance (normalized to the gold electrode geometric surface area, *A*, 0.1 cm^2) can be

defined at a given frequency as:

$$C = imag(Y)/\omega/A \qquad (1.4)$$

Table 1.3 summarizes the experimental data as determined from a single experiment for each particular system. All interfacial capacitances are reported with two significant figures, with the experimental error being less than 1%. However, the measurements, for example, for a number of SAMs demonstrate that Q_0 can vary around 5%.

Table 1.3. Interfacial capacitances (μF/cm^2) at a frequency of 100 Hz determined from a single experiment for each particular system.

Redox Couple	E_{dc} (V)	Bare Au	SAM	HBM	HBM +mellitin	[melittin][a]
$Ru(NH_3)_6^{3+}$	0.0	80	1.4	0.90	1.1	1
$FcCH_2OH$	0.0	24	1.3	1.0	1.6	3
$Fe(CN)_6^{3-}$	0.4	70	1.2	1.0	2.0	5

[a] Micromolar concentrations (μM) of melittin in contact with the HBM.

All three SAMs and three HBMs have comparable specific capacitances. The decrease in the specific capacitances from SAMs to HBMs is less than the decrease that is expected if the thickness of the dielectric barrier is roughly doubled. This observation may be explained by variations in the electrode area accessible to the electrolyte because

of a change in wetting properties of the gold electrode in the hanging meniscus configuration. The deposition of the SAM results in the hydrophobic surface. In contrast, the HBM has a hydrophilic surface due to the phospholipid head group. Thus, the wetted surface area may increase in the presence of the HBM, and the interfacial capacitance may be larger than expected.

Deposition of the SAM greatly attenuates the faradaic admittances (compare Figures 1.1B, 1.2 and 1.3 with Figures 1.4A, 1.5A, 1.6A). The real parts of the faradaic admittances for $Ru(NH_3)_6^{3+}$ and $FcCH_2OH$ are larger than their imaginary parts. In addition, the imaginary part is shifted to more negative potentials for $Ru(NH_3)_6^{3+}$ in Figure 1.4A and to more positive potentials for $FcCH_2OH$ in Figure 1.5A. The faradaic processes appear to become *ac* quasi-reversible.[35] However, the process for $Ru(NH_3)_6^{3+}$ is still DC-reversible, because little hysteresis appears between the forward and reverse scans in Figure 1.4A. Previous work shows that electrodes coated with SAMs behave like microarray electrodes.[24] The microarray model accounts for the apparent *ac* quasi-reversibility (i.e., diminished standard rate constant). However, attempts to fit the faradaic admittances in Fig. 1.4A to the equations for *ac* quasi-reversible systems[35] reveal discrepancies in peak height and width. The poor fits may be attributed to nonlinear diffusion effects associated with microarray electrodes. Therefore, the shape of the faradaic wave should be properly described by expressions applicable for the CEC mechanism that is the electrochemical analogue of the microarray electrode. However, no attempts were undertaken to analyze the faradaic admittance waves quantitatively according to the microarray model.

Analysis of the faradaic admittance for $FcCH_2OH$ is further complicated by adsorption. The adsorption wave seen at the bare gold electrode also shows up with the SAM at a potential 90 mV more positive than the half-wave potential (+0.2 V). Also, adsorption of neutral ferrocene on the SAM/Au interface results in hysteresis between the forward and reverse scans. The forward scan from −0.1 V results in higher faradaic admittance data than the reverse scan. Switching the initial potential to +0.4 V results in significantly less pronounced hysteresis because the cationic ferricenium form has less tendency to adsorb on the SAM/Au interface.

Figure 1.6A demonstrates that the faradaic reaction for $Fe(CN)_6^{3-}$ is more dramatically attenuated by the presence of SAM in comparison with the other two redox couples. No faradaic wave can be seen for $Fe(CN)_6^{3-}$ at its half-wave potential. Only a pseudo-exponential rise in the real component of the faradaic admittance is detected at high overpotentials (negative of 0.0 V). This behavior becomes more visible at lower frequencies (a few Hz), when the real and imaginary parts of the interfacial admittance have comparable magnitudes. As noted by Plant,[15] the SAM impedance data collected over a wide frequency range at the high negative overpotentials can be modeled by a $R_u(QR_{ct})$ equivalent circuit.

The deposition of HBMs further attenuates the faradaic processes for all three redox couples (Figures 1.4B-1.6B). In particular, the imaginary parts of the faradaic admittance near the half-wave potentials become almost negligible and the phase of the faradaic admittances approaches zero. This behavior suggests that the density of defects is reduced during the deposition of the phospholipid layer, perhaps because the

phospholipid layer can span existing defects in the SAM. Hysteresis between the forward and reverse scans in Figure 1.4B shows that the faradaic process exhibits DC quasi-reversibility even at the DC potential scan rate of 10 mV/sec.[35] The almost complete attenuation of faradaic admittance for $FcCH_2OH$ and the slight hysteresis between forward and reverse scans can be rationalized as a reduction in defect density and a reduction in adsorption of neutral ferrocene at the HBM/Au interface (possibly because of the polar head groups on the surface of the HBM). For $Fe(CN)_6^{3-}$, only a pseudo-exponential rise in the real part of the faradaic admittance at high overpotentials is observed (Figure 1.6B). The impedance data for $Fe(CN)_6^{3-}$ collected over a wide frequency range at DC potentials negative to 0 V can be fitted by the $R_u(QR_{ct})$ equivalent circuit. At −0.1 V vs. SCE, the systems in Figures 1.6A and 1.6B yield R_{ct} values of $2.8\times10^5\ \Omega$ in the presence of the SAM and $9.0\times10^5\ \Omega$ in the presence of the HBM. The R_{ct} values are comparable to those reported by Plant.[15]

In summary, the appearance of the faradaic waves near the half-wave potentials for kinetically fast $Ru(NH_3)_6^{3+}$ and $FcCH_2OH$ demonstrate that defects are present in both SAMs and HBMs. It is unlikely, particularly in the case of the HBMs, that the electron transfer occurs by tunneling across the surface coating. The presence of the imaginary part of the faradaic admittance at frequencies lower than 100 Hz (data not shown) is indicative of the faradaic process being under the mixed diffusion/kinetic control. The nearly absent faradaic response for $Fe(CN)_6^{3-}$ on a SAM- or HBM-coated electrode results from significantly slow kinetics for $Fe(CN)_6^{3-}$ at a bare gold electrode. Therefore, the SAM and HBM defects can only be detected by kinetically fast $Ru(NH_3)_6^{3+}$ and

$FcCH_2OH$.

7.3. ACV results for HBMs with melittin

Melittin has an effect on both the HBM dielectric properties and the rate of the faradaic reactions across HBMs. Figures 1.4C, 1.5C, 1.6C demonstrate an increase in the interfacial admittance (for both the real and imaginary components) at DC potentials where no faradaic reaction takes place, in comparison with data shown in Figures 1.4B, 1.5B, 1.6B. The increase in interfacial admittance is consistent with partitioning of cationic melittin into the HBMs. Partitioning of melittin into the HBM not only results in an increase the magnitude of the CPE Q_0, but also results in a decrease of exponent n, as determined by analyzing ACV data acquired over a range of frequencies. The exponent drops down from almost unity (0.99) for the pure HBM to 0.8-0.9 for the HBM with melittin. Penetration of water into the HBM is one rationale for this observation.[36,37] The specific HBM capacitance as defined by Eq. 1.4 is also increased (HBM+Melittin, Table 1.3). As evident from Table 1.3, a higher concentration of melittin results in a higher value of the specific HBM capacitance. These results are in contrast to the lack of capacitance changes during melittin adsorption reported by Plant.[14,15]

Adsorption of melittin almost completely shuts down the faradaic reaction for cationic $Ru(NH_3)_6^{3+}$ (Fig. 1.4B and 1.4C), has little effect on neutral $FcCH_2OH$ (Fig. 1.5B and 1.5C) and dramatically enhances the faradaic reaction for anionic $Fe(CN)_6^{3-}$ (Fig. 1.6B and 1.6C).[14,15] In particular, the faradaic admittance for $Fe(CN)_6^{3-}$ in Figure 1.6C

has both real and imaginary components at the half-wave potential for this redox couple. The presence of hysteresis between the forward and reverse scans indicates that diffusion of ferricyanide to the electrode is a significant component of the current.

There are three conceivable mechanisms by which melittin may affect the permeability of the bilayer. The first is an electrostatic effect. The cationic melittin would generate a positive charge on the surface of the bilayer that repels cations (like $Ru(NH_3)_6^{3+}$) and attracts anions (like $Fe(CN)_6^{3-}$). Consequently, transport of charged redox couples by pre-existing defects in the bilayer should be very sensitive to the presence of melittin in or on the bilayer. Experiments with SAMs show that changing the surface charge on the SAM (e.g. via an ionizable functional group) can have a dramatic effect on the apparent permeability of a SAM to a charged redox couple.[19] Second, melittin may form pores of molecular dimensions with selectivity for anions. It is known that melittin induces voltage-dependent anion-selective channels in lipid bilayers.[38,39] Finally, melittin may induce sufficiently large pores capable of transporting proteins (as in hemolysis).

The loss of permeability of the HBM towards $Ru(NH_3)_6^{3+}$ is consistent with a large electrostatic effect. Transport of the cationic redox couple by pre-existing defects is strongly inhibited by an increase in the positive surface charge of the HBM (Fig. 1.4B and 1.4C). The loss of permeability does not support or eliminate the formation of anion-selective channels. It does suggest the absence of formation of large pores, although even in protein-size pores, the reduction of $Ru(NH_3)_6^{3+}$ concentration near the electrode would inhibit faradaic currents via this mechanism.

The absence of any increased permeability of the HBM towards $FcCH_2OH$ indicates that melittin does not create pores large enough to permit this molecule to penetrate the bilayer. Because ferrocene is kinetically fast, any formation of large pores (such as must occur during hemolysis) would have a pronounced effect on the apparent permeability of the HBM to $FcCH_2OH$. These results do not support or eliminate the existence of channels, since the hydrophobic ferrocene molecule may prefer to partition into less hydrophilic parts of the HBM.

The effect of melittin on $Fe(CN)_6^{3-}$ permeability through the HBM is less easy to interpret. Cationic melittin should greatly enhance the surface concentration of ferricyanide relative to the bulk concentration, thus increasing the faradaic current by existing defects in the HBM. Likewise, the presence of ferricyanide channels formed by melittin would account for the observed results. These results do not discriminate between the electrostatic mechanism (pre-existing defects) and the channel mechanism (new pores formed by melittin). The same conclusions can be made from a CV (Fig. 1.7) taken on the same system shown in Figure 1.6C (ferricyanide and melittin present). The CV exhibits a plateau feature with currents much smaller than the diffusion-limited currents to bare gold electrode. On the return scan, significant anodic currents are evident. This CV is consistent with the micro-array model in which the active sites for electron transfer are widely separated, but with some overlap of the diffusion profiles.

The permeability of the HBM to ferricyanide in the presence of melittin (Fig. 1.6C) is dramatically greater than even the permeability of the SAM (Fig. 1.6A). Again, this observation alone is not sufficient to clearly distinguish between the two

mechanisms. In addition, it is necessary to point out that enhanced transport is not the only possible explanation for the dramatic increase. Any mechanism that accelerated the rate of electron transfer between the ferricyanide and the electrode would also account for the observed results. However, the means by which the rate of electron transfer can be accelerated is not immediately apparent in this system.

It must be emphasized that the observed effect of melittin on heterogeneous electron transfer across HBMs is not necessarily correlated with melittin activity in the cellular membranes. In the latter case, there is a well-defined aqueous reservoir on both sides of a membrane composed of two layers of mobile phospholipids. To simulate this situation on the electrode, the bilayer would have to be suspended above the electrode.[3]

8. Conclusions

The sequential deposition of the SAM and HBM on the gold electrode creates a dielectric barrier that greatly attenuates the rate of heterogeneous electron transfer between soluble redox couples and the gold electrode. The faradaic reactions occur via the HBM defects that can be detected by using the kinetically fast redox couples, $Ru(NH_3)_6^{3+}$ and $FcCH_2OH$. Faradaic current of the kinetically slower redox couple $Fe(CN)_6^{3-}$ is reduced to a small leakage current at large negative overpotentials. The adsorption of cationic melittin affects both the HBM dielectric properties and the rate of the faradaic reactions. The capacitance of the HBM is increased. Under conditions of the experiments reported in this paper, the apparent permeability of the HBM is enhanced for

the negatively charged $Fe(CN)_6^{3-}$, reduced for the positively charged $Ru(NH_3)_6^{3+}$ and not visibly affected for the neutral $FcCH_2OH$. These results are attributed to the absence of large pore formation by the melittin, the electrostatic repulsion of cations and attraction of anions, and the possible formation of anion-selective channels in the HBM. The latter two mechanisms cannot be distinguished.

Acknowledgment

The author acknowledges discussions with Dr. Anne L. Plant on the melittin effect on HBMs and on a method for the HBM preparation. Also, thanks are due to Prof. Arthur S. Pavlovic for the X-ray back-scattering experiments.

References

1. E. Sackman, Science 43 (1996) 271.
2. M. Rouhi, C&EN, June 23 (1997) 36.
3. B. A. Cornel, V. L. B. Braach-Maksvytis, L. G. King, P. D. Osman, B. Raguse, L. Wieczorek, R. J. Pace, Nature 387 (1997) 580.
4. A. Downard, Analytical Chemistry News & Features December 1 (1998) 774.
5. A. Janshoff, J. Wegener, C. Steinem, M. Sieber, H.-J. Galla, Acta Biochimica Polonica 43 (1996) 339.
6. L. Williams, S. Evans, T. Flynn, A. Marsh, P. Knowles, R. Bushby, N. Boden, Langmuir 13 (1997) 751.
7. Y. Cheng, N. Boden, R. Bushby, S. Clarkson, S. Evans, P. Knowles, A. March, R. Miles, Langmuir 14 (1998) 839.
8. B. Raguse, V. Braach-Maksvytis, B. Cornell, L. King, P. Osman, R. Pace, L. Wieczorek, Langmuir 14 (1998) 648.
9. J. Cullison, F. Hawkridge, Langmuir 10 (1994) 877.
10. O. Pierrat, N. Lechat, C. Bourdillon, J.-M. Laval, Langmuir 13 (1997) 4112.
11. J. Ha, C. Henry, I. Fritsch, Langmuir 14 (1998) 5850.
12. K. Seifert, K. Fendler, E. Bamberg, Biophys. J. 64 (1993) 384.
13. J. Li, L. Ding, E. Wang, S. Dong, J. Electroanal. Chem., 414 (1996) 17.
14. A. Plant, Langmuir 9 (1993) 2764.
15. A. Plant, M. Gueguetchkeri, W. Yap, Biophysical J. 67 (1994) 1126.
16. S. Terrettaz, T. Stora, C. Duschl, H. Vogel, Langmuir 9 (1993) 1361.
17. M. Thompson, U. Krull, Anal. Chem. 63 (1991) 393A.
18. Langmuir-Blodgett Films, G. Roberts, (Ed.), Plenum Press, New York and London, 1990.
19. H. O. Finklea, in A. J. Bard, I. Rubinstein (Eds.), Electroanalytical Chemistry, Marcel Dekker, vol. 19, New York, 1996 p. 109.
20. Th. Wink, S. van Zuilen, A. Bult, W. Bennekom, Analyst 122 (1997) 43R.

21. E. Kalb, S. Frey, L. Tamm, Biochim. Biophys. Acta 1103 (1992) 307.
22. E. Florin, H. Gaub, Biophysical J. 64 (1993) 375.
23. L. Ding, J. Li, S. Dong, E. Wang, J. Electroanal. Chem. 416 (1996) 105.
24. H. O. Finklea, D. A. Snider, J. Fedyk, E. Sabatini, Y. Gafni, I. Rubinstein, Langmuir 9 (1993) 3660.
25. S. Blankenborg, M. Sluyters-Rehbach, J. H. Sluyters, J. Electroanal. Chem., 349 (1993) 255.
26. H. Strehlow, W. Knochew, Fundamentals of chemical relaxation, Verlag Chemie, NY, 1977.
27. S. Lingler, I. Rubinstein, W. Knoll, A. Offenhausser, Langmuir 13 (1997) 7085.
28. B. Lindholm-Sethson, Langmuir 12 (1996) 3305.
29. M. Stelzle, G. Weissmuller, E. Sackmann, J. Phys. Chem. 97 (1993) 2974.
30. C. Dempsey, Biochim. Biophys. Acta, 1031 (1990) 143.
31. M. Sansom, Current Opinion in Colloid & Interface Science, 3 (1998) 518.
32. D. Dickertmann, F. D. Koppitz, J. W. Schultze, Electrochim. Acta 21 (1976) 967.
33. R_u is sensitive to the height of the electrolyte meniscus, and must be measured every time the meniscus is formed.
34. A. Hamelin, J. Electroanal. Chem. 142 (1982) 299.
35. A. M. Bond, R. J. O'Halloran, I. Ruzic, D. E. Smith, Anal. Chem. 48 (1976) 872.
36. M. Bachar, O. M. Becker, J. Chem. Phys. 111 (1999) 8672.
37. S. Berneche, M. Nina, B. Roux, Biophys. J. 75 (1998) 1603.
38. M. T. Tosteson, D. C. Tosteson, Biophys. J. 36 (1981) 109.
39. M. T. Tosteson, D. C. Tosteson, Biophys. J. 45 (1984) 112.

Figure 1.1 (a). Total cell admittance for a bare electrode in the presence of 1 mM $Ru(NH_3)_6^{3+}$ at f = 100 Hz. The forward scan, initiated at +0.05 V, has lower values for both real and imaginary parts at DC potentials positive of the half-wave potential and higher values at DC potentials negative of the half-wave potential.

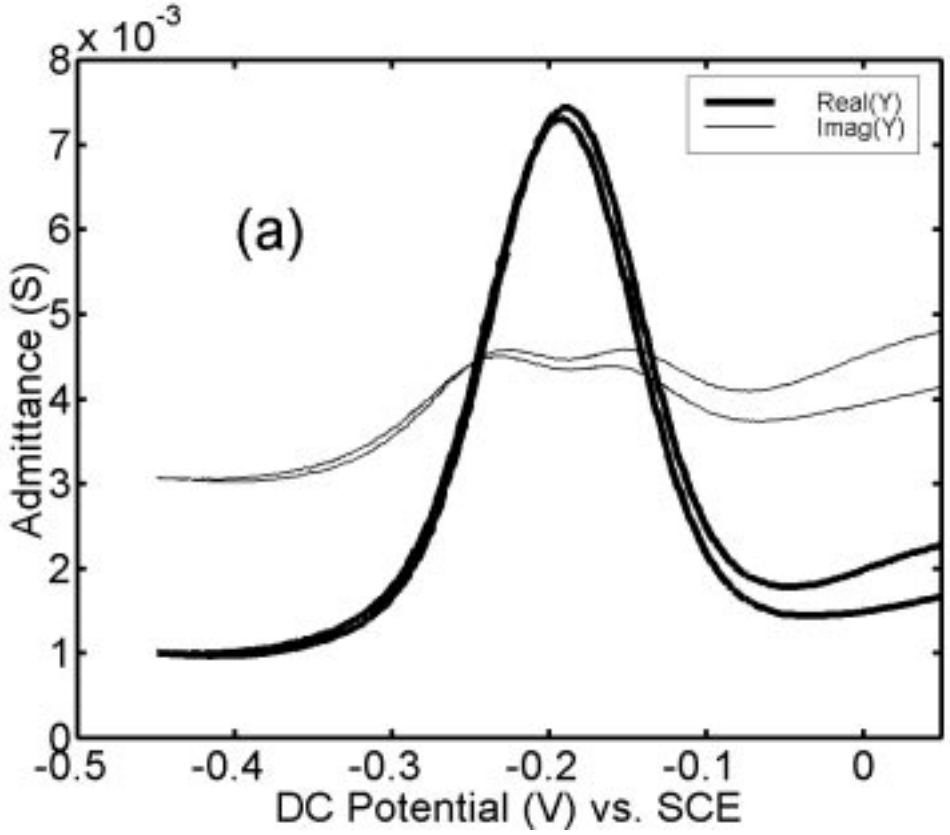

Figure 1.1 (b) Interfacial admittance for a bare electrode in the presence of 1 mM $Ru(NH_3)_6^{3+}$ at f = 100 Hz after correction for R_u (60 Ω).

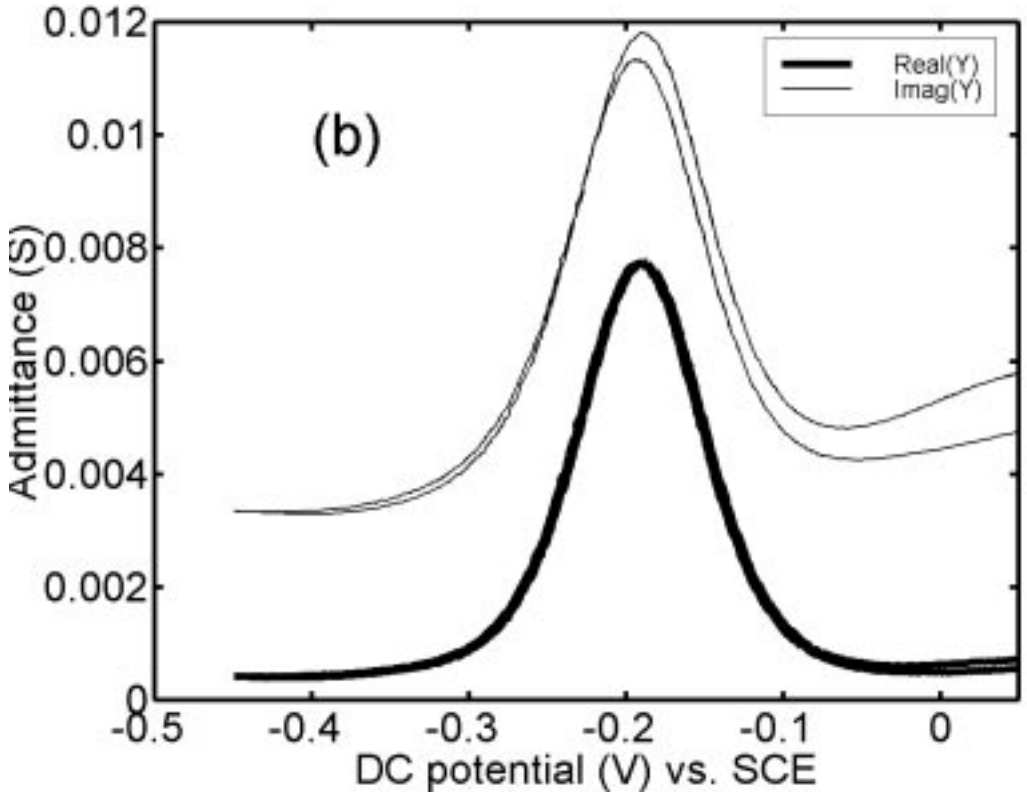

Figure 1.1 (c) Faradaic admittance for a bare electrode in the presence of 1 mM $Ru(NH_3)_6^{3+}$ at f = 100 Hz after baseline correction of CPE admittance.

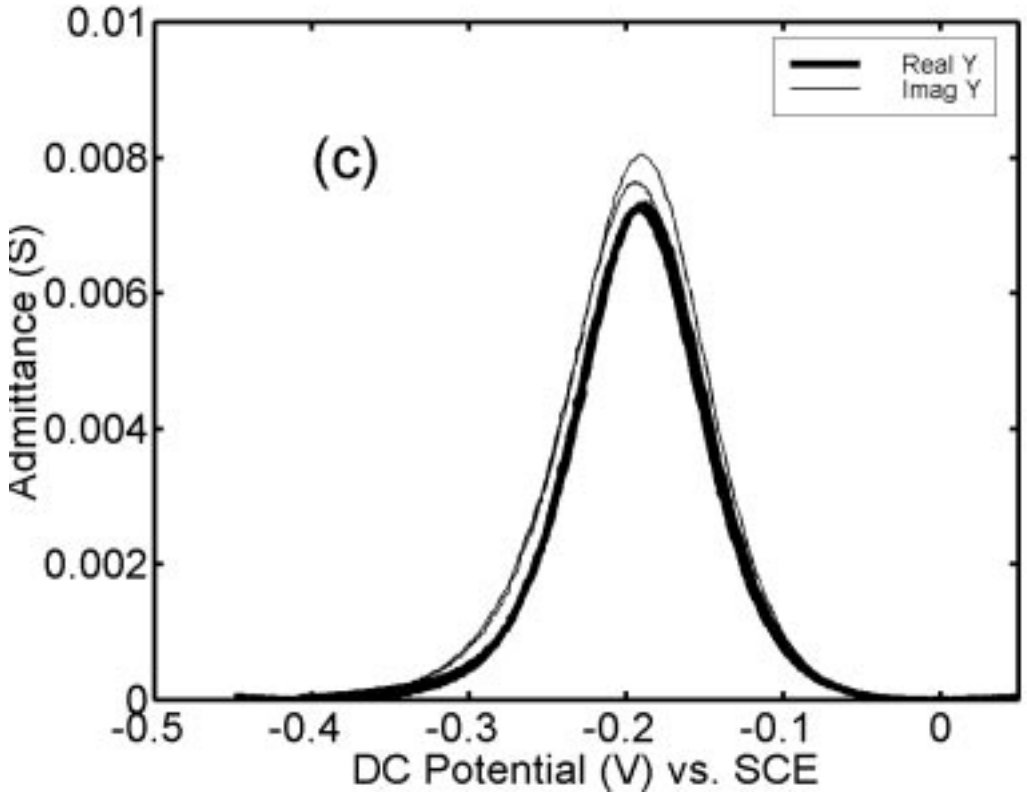

Figure 1.2. Interfacial admittance (corrected for R_u (92 Ω)) for a bare electrode in the presence of 0.2 mM $FcCH_2OH$ at f = 100 Hz. The forward scan, initiated at –.1 V, has lower values for both real and imaginary parts at DC potentials negative of the half-wave potential and higher values at DC potentials positive of the half-wave potential.

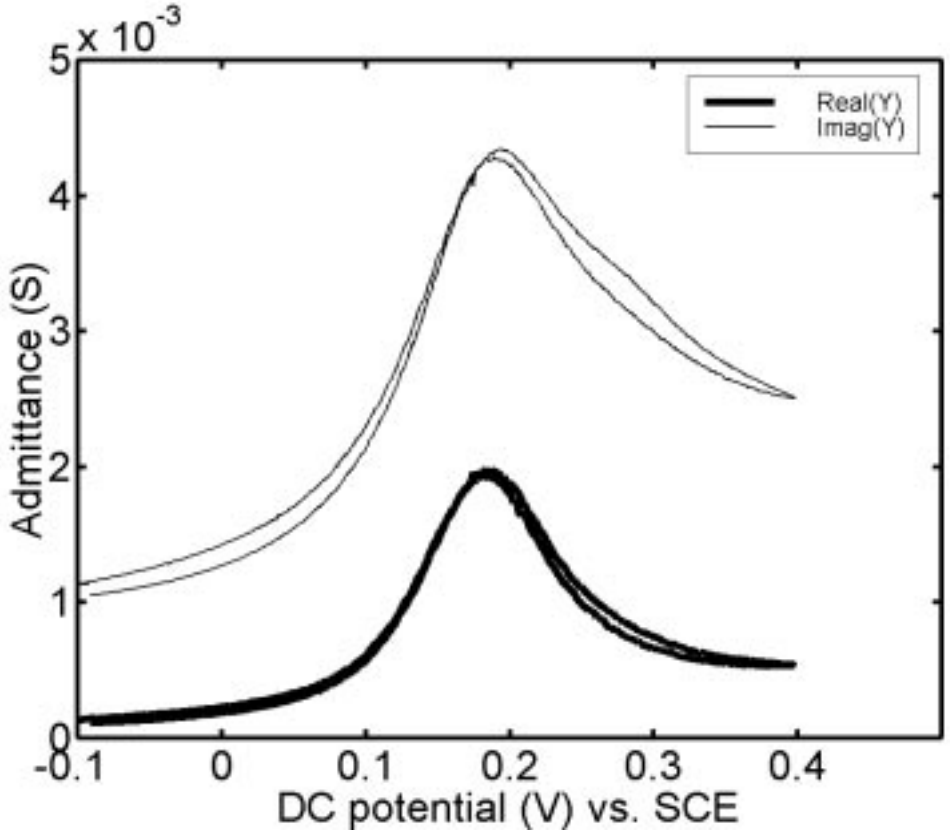

Figure 1.3. Interfacial admittance (corrected for R_u (56 Ω)) for a bare electrode in the presence of 1 mM $Fe(CN)_6^{3-}$ at f = 100 Hz. The forward scan, initiated at +0.4 V, has lower values for both real and imaginary parts at DC potentials positive of +0.35 V and higher values at DC potentials negative of the half-wave potential.

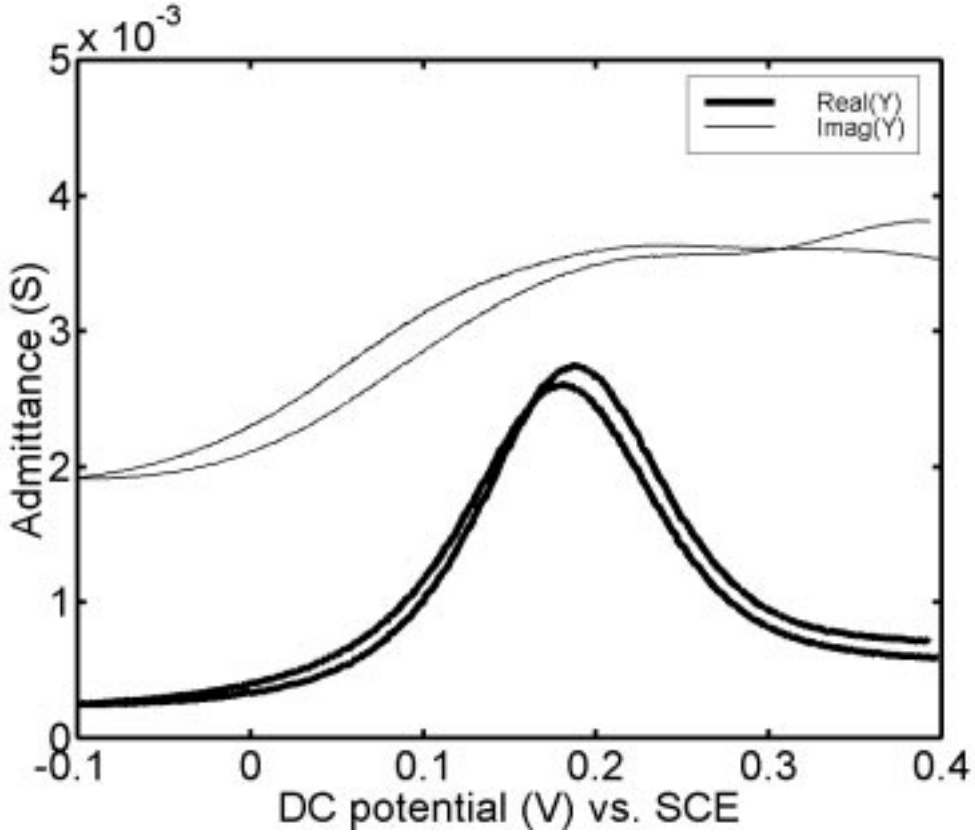

Figure 1.4 (a). Interfacial admittance for a SAM-coated electrode in the presence of $Ru(NH_3)_6^{3+}$ at f = 100 Hz. The forward scan, initiated at 0.05 V, has lower values for both real and imaginary parts at DC potentials positive of the half-wave potential and higher values at DC potentials negative of the half-wave potential.

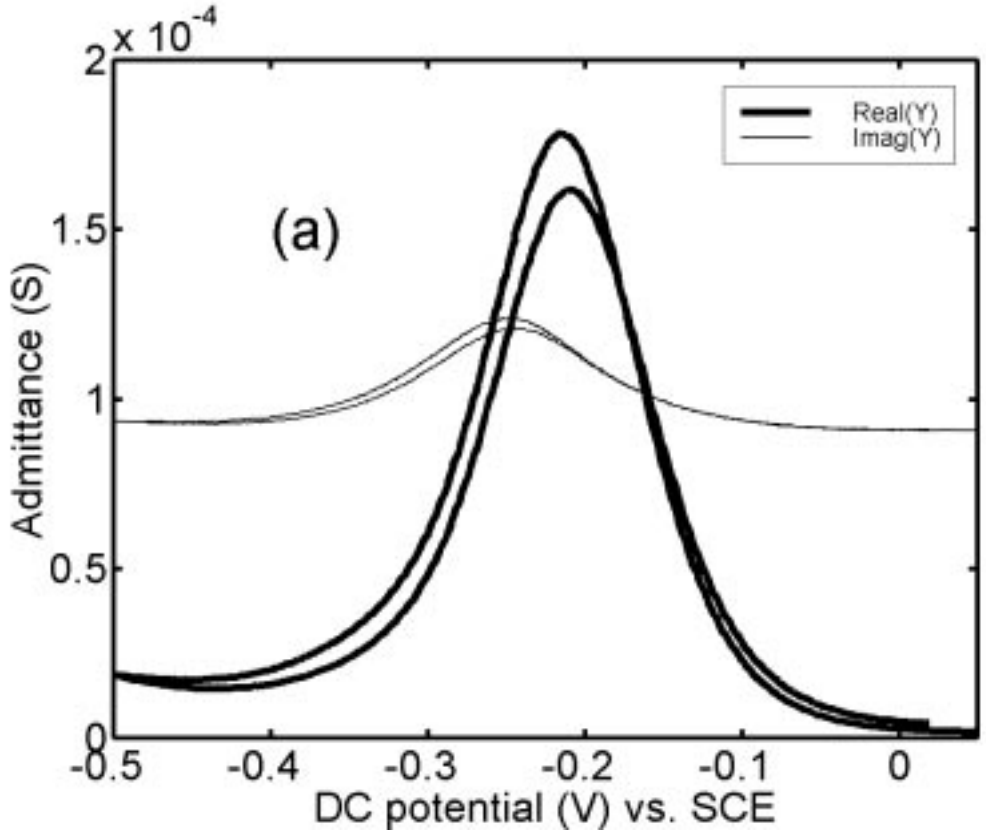

Figure 1.4 (b) Interfacial admittance for a HBM-coated electrode in the presence of $Ru(NH_3)_6^{3+}$ at f = 100 Hz.

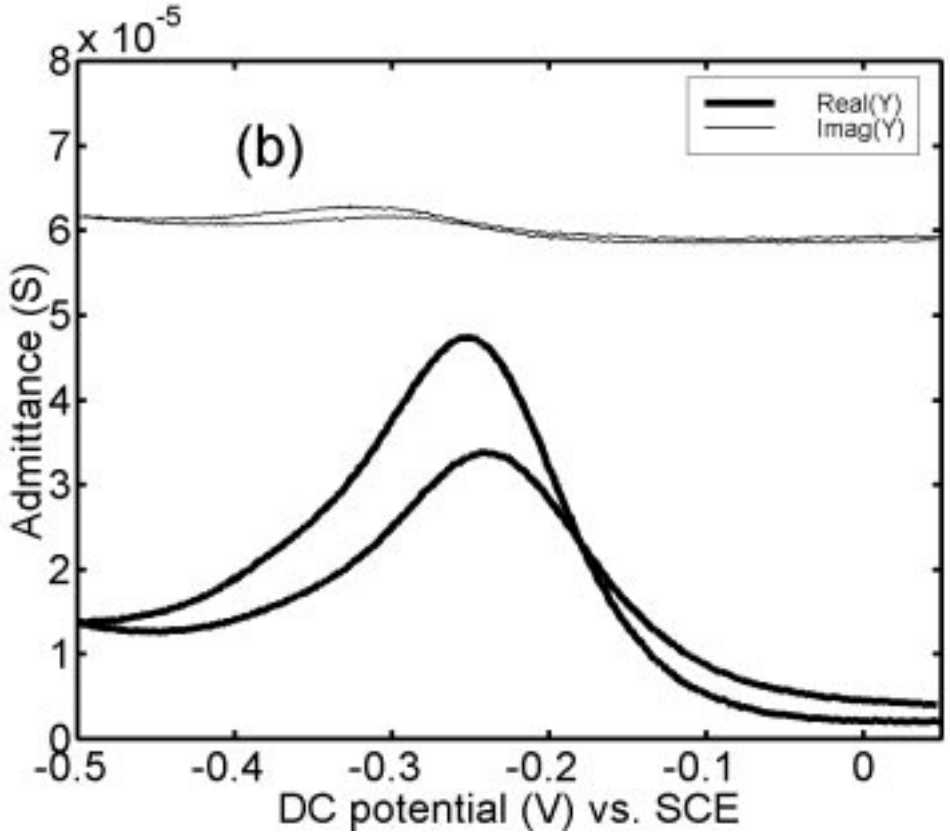

Figure 1.4 (c) Interfacial admittance for a HBM-coated electrode in the presence of 1 µM melittin and $Ru(NH_3)_6^{3+}$ at f = 100 Hz.

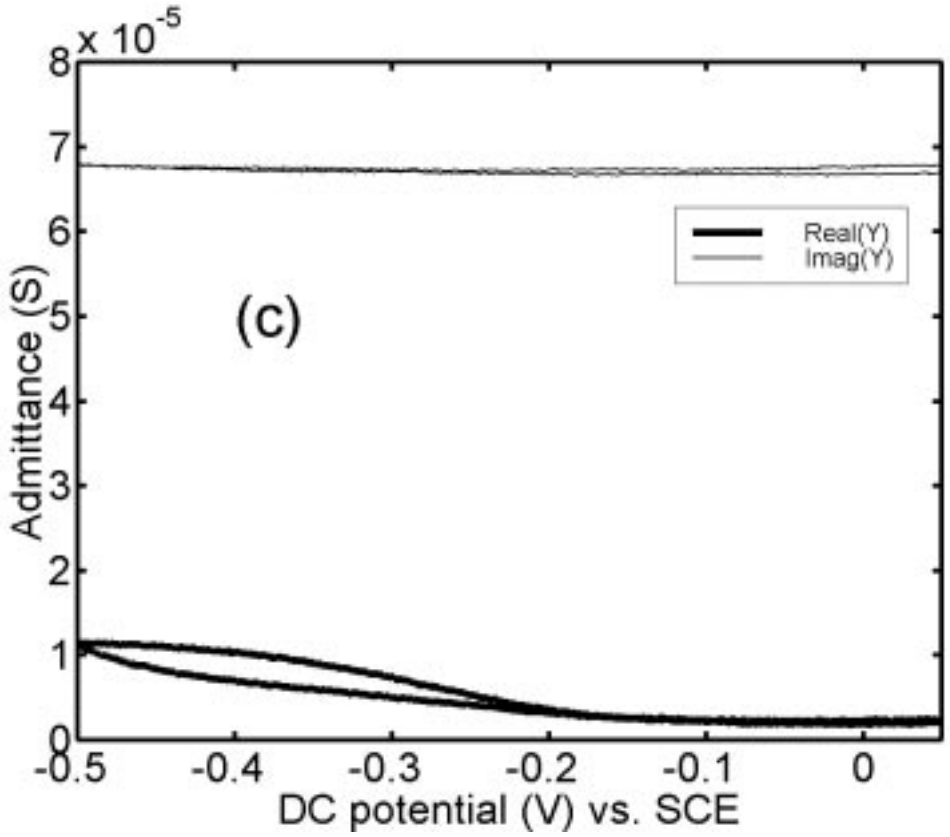

Figure 1.5 (a). Interfacial admittance for a SAM-coated electrode in the presence of $FcCH_2OH$ at f = 100 Hz. The forward scan, initiated at −0.1 V, has higher values for both real and imaginary parts at DC potentials positive of the half-wave potential.

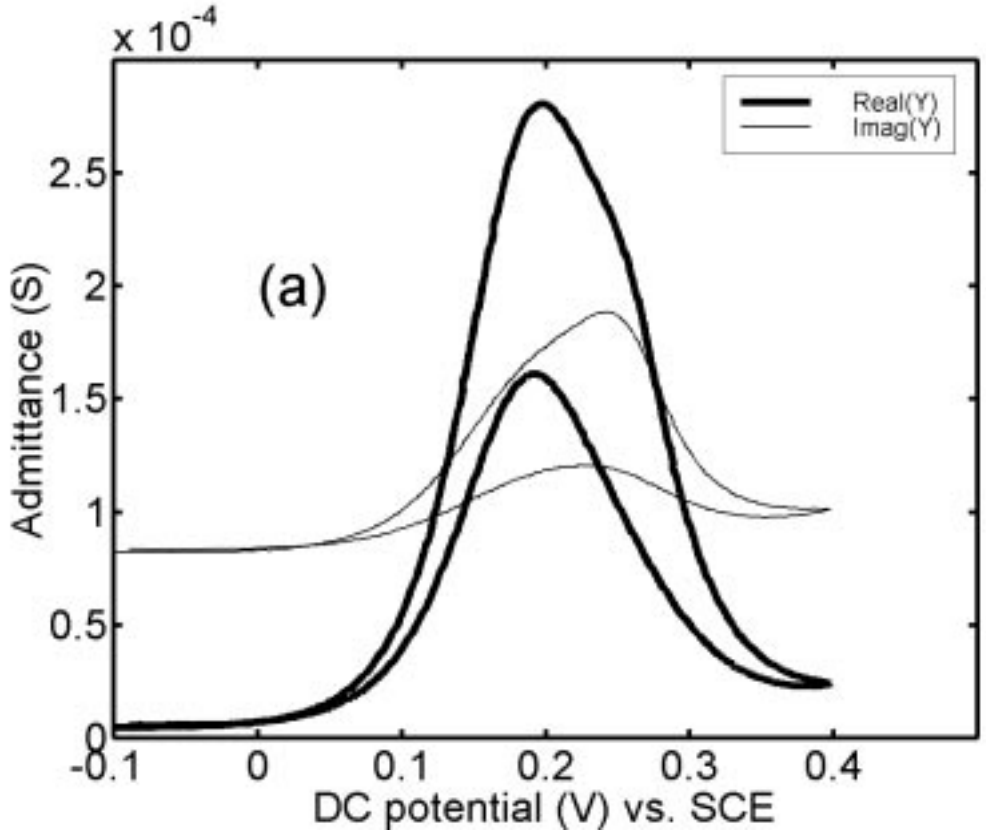

Figure 1.5 (b). Interfacial admittance for a HBM-coated electrode in the presence of $FcCH_2OH$ at f = 100 Hz.

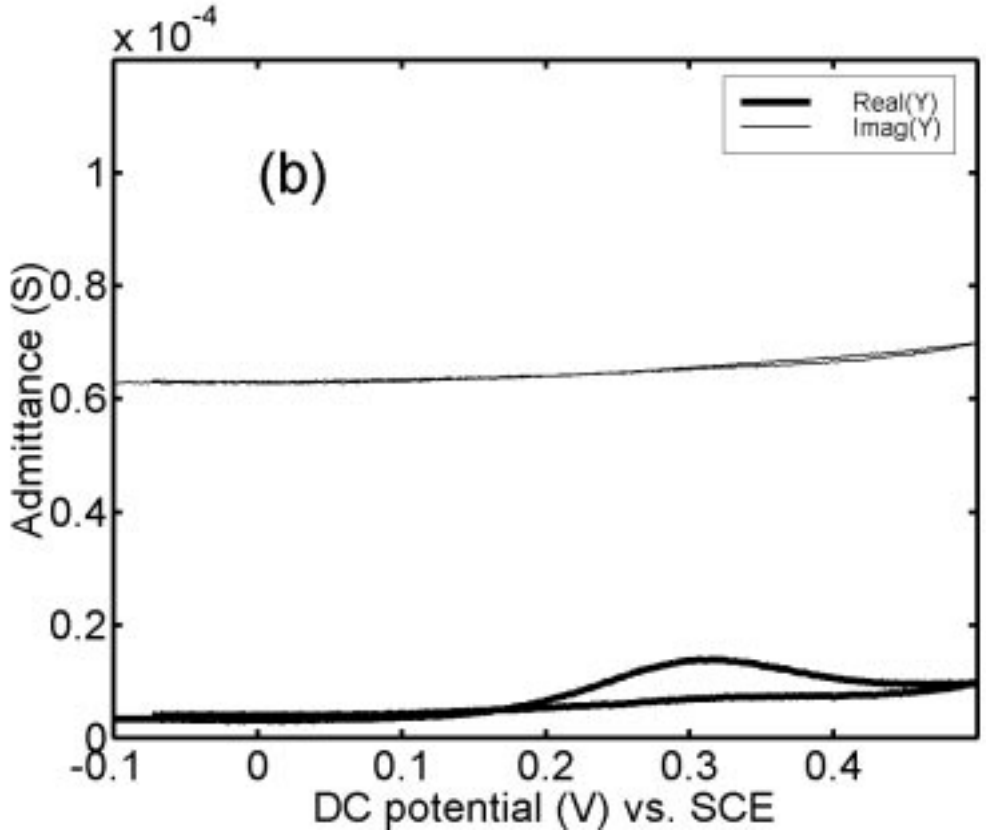

Figure 1.5 (c). Interfacial admittance for a HBM-coated electrode in the presence of 3 μM melittin and $FcCH_2OH$ at f = 100 Hz.

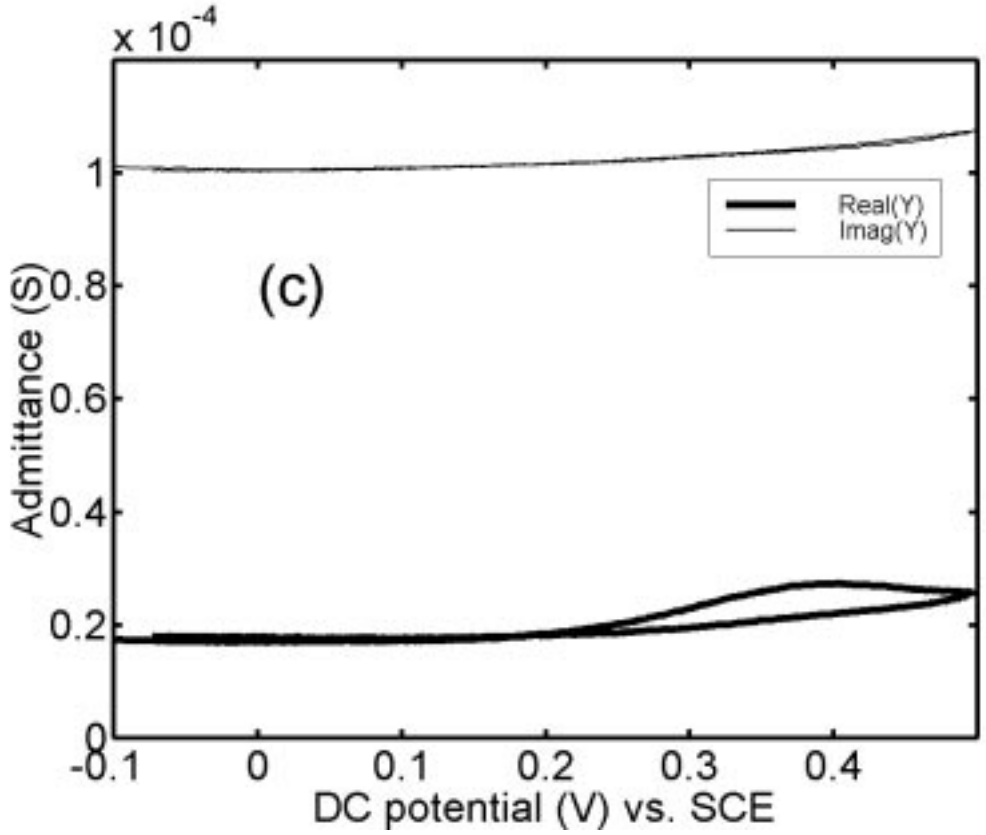

Figure1.6 (a). Interfacial admittance for a SAM-coated electrode in the presence of $Fe(CN)_6^{3-}$ at f = 100 Hz. The real part is plotted twice. In the second line, it is multiplied by 10 in order to show more clearly a pseudo-exponential rise at DC potentials negative of 0 V.

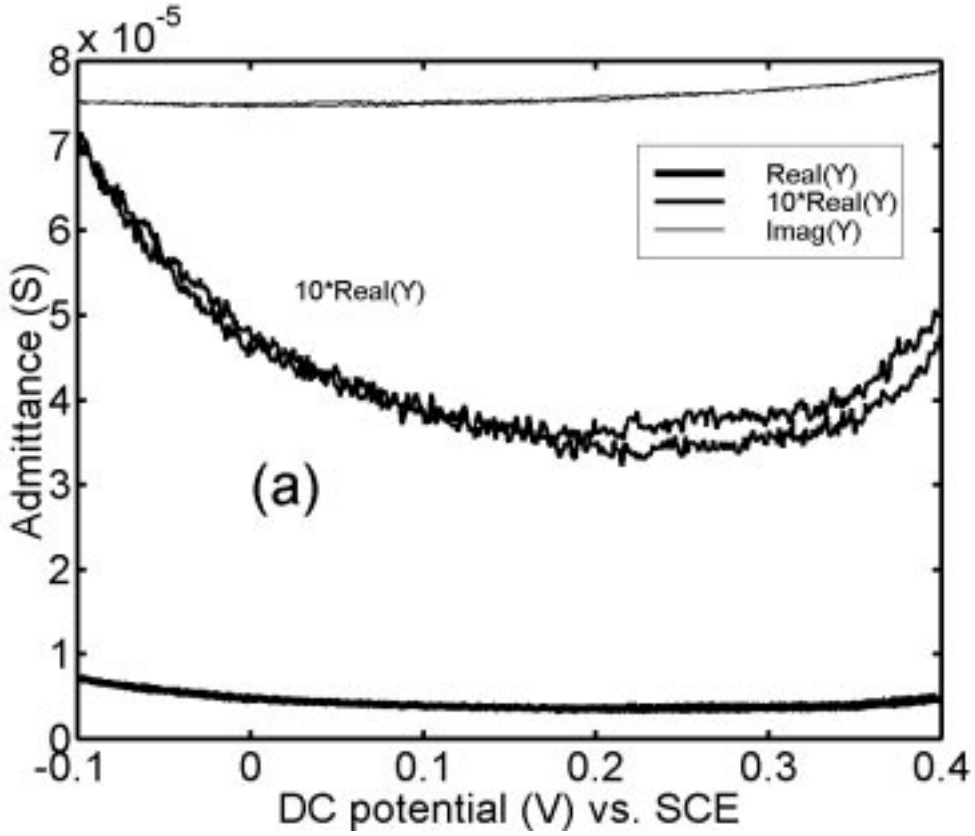

Figure 1.6 (b) Interfacial admittance for a HBM-coated electrode in the presence of $Fe(CN)_6^{3-}$ at f = 100 Hz. The real part is plotted twice. In the second line, it is multiplied by 10 in order to show more clearly a pseudo-exponential rise at DC potentials negative of 0 V.

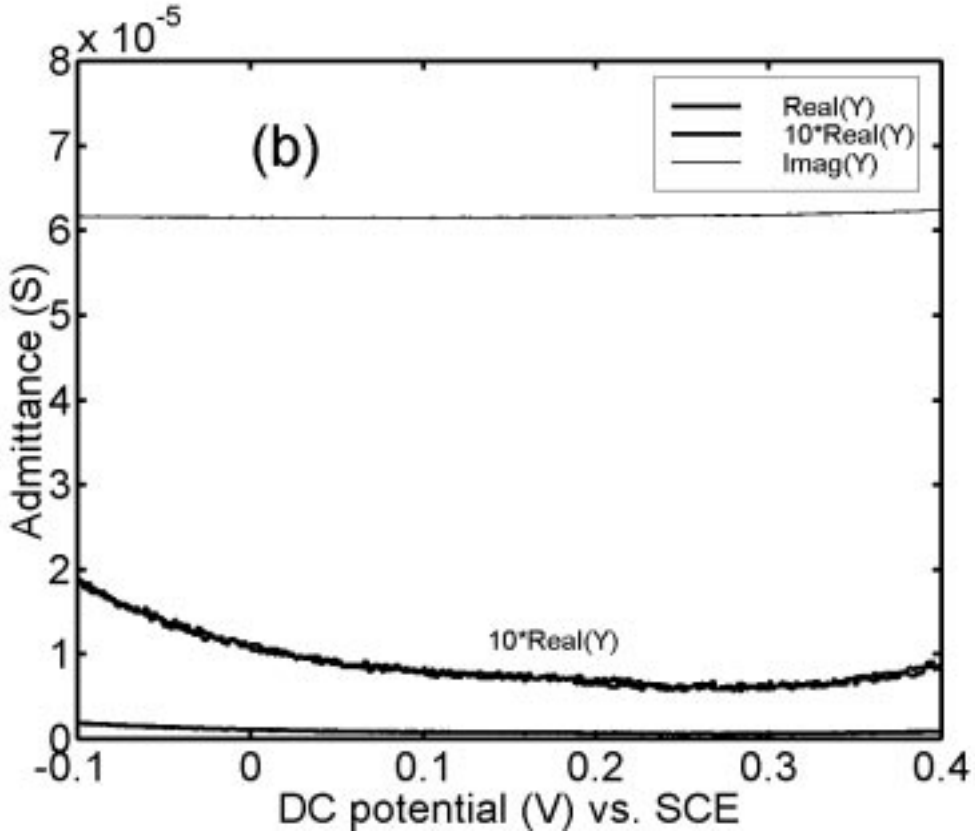

Figure 1.6 (c) Interfacial admittance for a HBM-coated electrode in the presence of 3 μM melittin and $Fe(CN)_6^{3-}$ at f = 100 Hz.

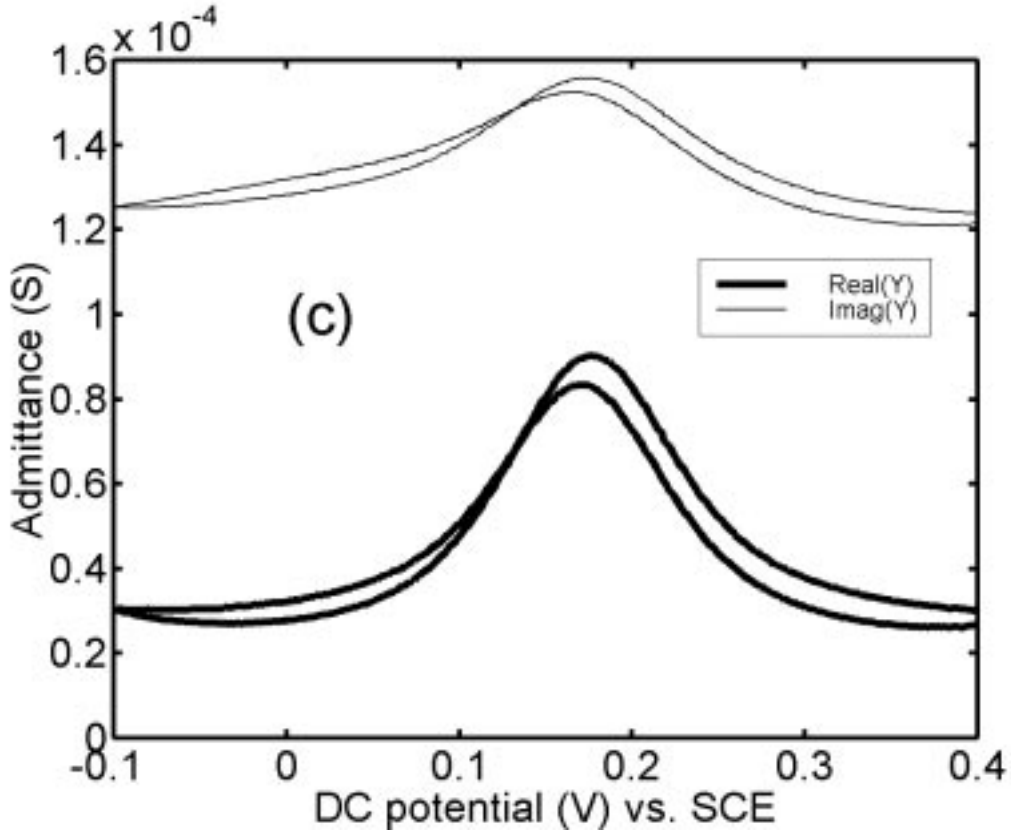

Figure 1.7. Cyclic voltammograms of a HBM-coated electrode in 1 mM $Fe(CN)_6^{3-}$ before melittin addition (bold line; medium line currents multiplied by 10), and after addition of 5 µM melittin (light line). Scan rate 0.1 V/s.

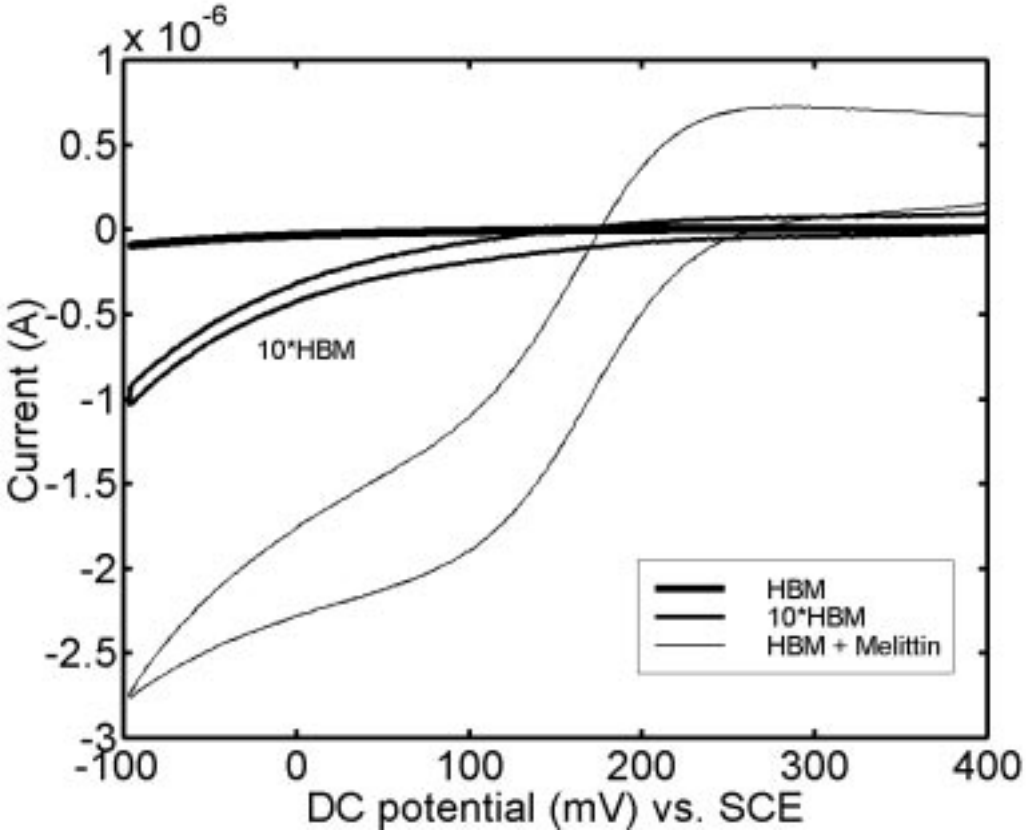

Chapter Two

Second harmonic AC Voltammetry study of a fast faradaic process in the presence of uncompensated resistance

1. Introduction to second harmonic AC Voltammetry (SH ACV)

Electrochemical methods employing the superposition of a DC potential and a sinusoidal potential perturbation $\Delta E\sin(\omega t)$ are widely used. In a typical electrochemical impedance spectroscopy (EIS) experiment, the DC potential is kept constant and the angular frequency ω of the *ac* potential perturbation is varied. The cell impedance, the ratio of *ac* potential to *ac* current, is obtained as a function of frequency. This method allows one to separate electrode processes occurring with different time constants. A method complementary to EIS, AC Voltammetry (ACV), combines a DC potential scan and a single frequency *ac* potential perturbation. Thus, after corrections for the uncompensated resistance and the double layer admittance, the DC potential dependence of the faradaic admittance can be found.

Both methods, EIS and ACV, assume that the electrochemical cell behaves as a linear system, e.g., the system generates a measurable *ac* current only at the perturbation frequency and the amplitude of the *ac* current is proportional to the *ac* potential amplitude. This assumption is usually valid if the potential amplitude does not exceed $5/n$ mV RMS, where n is the number of electrons transferred in the redox reaction.

However, if a larger amplitude *ac* potential is applied to the electrochemical cell, the nonlinear faradaic element also generates a DC rectification current and current at higher harmonic frequencies ($2\omega, 3\omega, ...$). A number of theoretical treatments of the nonlinear faradaic response has appeared over the last 40 years. The theory for the second harmonic (2ω) ACV (SH ACV) for the reversible and quasi-reversible cases for both freely diffusing redox species and systems with coupled first-order homogeneous chemical reactions was developed by Smith.[1,2] More complicated cases of diffusion and charge transfer accompanied by adsorption were considered by Sluyters and Sluyters-Rehbach.[3] A recent paper published by Harrington considered a case when only adsorption and charge transfer occur.[4] Interest in applying SH ACV to study fast electrode kinetics has been based on the fact that, at a given frequency, SH ACV is claimed to be more sensitive to the kinetic status of the faradaic process than its fundamental counterpart first harmonic ACV (FH ACV). In addition, it is often assumed that the nonlinear faradaic response can be studied free from interference by non-faradaic electrode processes.[4] However, SH ACV is a rarely used electrochemical method and the potential benefits of SH ACV over FH ACV remain mostly unrealized because of the complexity of data collection and data analysis.

2. Objectives of this research project

The overall goal of the research project reported in Chapter Two is to consider the feasibility of SH ACV employment for the analysis of kinetically fast faradaic processes.

The enthusiastic initiation of this project was stimulated by the potential of SH ACV to characterize sub-micro defects in SAMs and HBMs and sub-millisecond kinetics in electroactive SAMs.

However, the preliminary experiments revealed a disagreement between the experiment and theory for the faradaic admittance obtained by SH ACV. The literature review[5-8] and following method development demonstrated that SH ACV measurements were distorted by the ohmic potential (*iR*) drop. Therefore, it could not be assumed that the measured SH current was representative of the pure faradaic response. This assumption is valid only if either complete positive feedback compensation is achieved[5,6] or very low perturbation frequencies are used.[7,8] At the same time, research on kinetically fast faradaic processes requires application of high perturbation frequencies at which complete positive feedback compensation is difficult.

It was first noticed by McKubre that all previous theoretical treatments of the nonlinear faradaic response suffer from a major deficiency.[9] The nonlinear faradaic impedance element is contained within a circuit comprising other linear (electrolyte resistance) and slightly nonlinear (double layer capacitance) terms. Therefore, analysis of the electrical circuit with an internal current source at 2ω has to be performed in order to correlate the measured SH current with the SH current generated by the nonlinear faradaic element. Furthermore, the SH current generated by the nonlinear faradaic element must be normalized to the square of the interfacial potential that is usually different from the measured cell potential because of the *iR* drop.

The emphasis in Chapter Two is placed on the development of both theoretical

background and experimental procedure in order to implement the above ideas. The experimental setup and software program for instrument control and data acquisition were developed for simultaneous recording of both the FH and SH ACVs. This arrangement permitted us to compare kinetic faradaic information obtained by these two methods and to estimate the reliability of the SH ACV data analysis in the presence of *iR* drop.

3. Second Harmonic Faradaic Response

A generic electrical circuit (Figure 2.1) that is frequently used to model the impedance behavior of a 3-electrode cell consists of three elements: faradaic impedance (Z_f), the constant phase element (CPE), which is used instead of the double layer capacitance, and the uncompensated resistance (R_u). The faradaic impedance element is a series combination of the Warburg (diffusion) element and the charge transfer resistance. The CPE admittance is defined as $Q=Q_0(j\omega)^{\chi}$, where Q_0 is a CPE constant and χ is less than unity.

Initially, we consider an idealized electrochemical cell in which Z_f is the only nonlinear element (specifically, the CPE is assumed to be a linear element). Because of the large amplitude of the interfacial potential $E^{inter}(\omega)$, the nonlinear Z_f generates the SH current $I^{far}(2\omega)$. The voltage node analysis with the current source at 2ω instead of the faradaic impedance element allows us to correlate the measured SH current $I^{measured}(2\omega)$ with the SH current $I^{far}(2\omega)$ generated by Z_f (see Figure 2.1). For the interfacial node, we

can write:

$$I^{far}(2\omega) = I^{measured}(2\omega) + I^{CPE}(2\omega) \tag{2.1}$$

where $I^{CPE}(2\omega)$ is the SH current that flows through the CPE out of the interfacial node. At the same time,

$$E^{inter}(2\omega) = E^{measured}(2\omega) + I^{measured}(2\omega) \times R_u \tag{2.2}$$

where $E^{inter}(2\omega)$ is the SH interfacial potential. Therefore,

$$I^{CPE}(2\omega) = E^{inter}(2\omega) \times Q(\omega\times 2) =$$
$$= E^{measured}(2\omega) \times Q(\omega\times 2) + I^{measured}(2\omega) \times R_u \times Q(\omega\times 2) \tag{2.3}$$

Substitution of Eq. 2.3 into Eq. 2.1 and rearrangement yield Eq. 2.4:

$$I^{far}(2\omega) = I^{measured}(2\omega) \times (1 + R_u \times Q(\omega\times 2)) + E^{measured}(2\omega) \times Q(\omega\times 2) \tag{2.4}$$

$Q(\omega\times 2)$ is the CPE admittance determined from a FH ACV experiment with a perturbation frequency twice that used in Eq. 2.4, ω. It is assumed that the CPE found from FH ACV experiments can be used for analysis of the SH ACV experiments. $E^{measured}(2\omega)$ arises from the potentiostat's inability to accurately control the *ac* potential

applied to the cell in the presence of the SH current. This effect is more noticeable at higher perturbation frequencies. $E^{measured}(2\omega)$ may also arise from the second harmonic distortion of an oscillator used to generate the *ac* potential. The dual origin of $E^{measured}(2\omega)$ complicates the data analysis. The problem is avoided if the contribution of the second term in Eq. 2.4, $E^{measured}(2\omega)\times Q(\omega\times 2)$, to $I^{far}(2\omega)$ is negligible.

The SH current, $I^{far}(2\omega)$, is proportional to the square of the interfacial potential, $E^{inter}(\omega)$, because of the Taylor's series expansion. Thus, the SH faradaic admittance, $Y^{far}(2\omega)$, is defined as:

$$Y^{far}(2\omega) = I^{far}(2\omega) / (E^{inter}(\omega))^2 / \sqrt{2} \qquad (2.5)$$

The $\sqrt{2}$ factor results from the fact that a Lock-in Amplifier reports data as RMS values whereas $Y^{far}(2\omega)$ is defined in terms of amplitude. The interfacial potential is found from the FH ACV experiment as:

$$E^{inter}(\omega) = E^{measured}(\omega) - I^{measured}(\omega) \times R_u \qquad (2.6)$$

$E^{measured}(\omega)$ is the FH potential difference between the working and reference electrodes (usually the output of the electrometer connected to the reference electrode). $E^{measured}(\omega)$ may be different from the *ac* potential applied to the cell because of a limited bandwidth of the potentiostat power amplifier. The sign in front of the $I\times R_u$ term in Eq. 2.6 differs from the sign in Eq. 2.2 because of the different origins of the current in two cases.

$I^{measured}(\omega)$ is the FH current signal obtained from the current follower in the potentiostat.

Eqs. 2.4-2.6 allow one to determine $Y^{far}(2\omega)$ assuming that Z_f is the only nonlinear element. However, a real electrochemical cell usually contains a CPE that demonstrates slight nonlinearity because of the dependence of Q_0 on the DC potential. Therefore, the background corrected SH faradaic admittance, $Y^{cor,\,far}(2\omega)$, can be obtained by subtracting the contribution from the nonlinear CPE element from $Y^{far}(2\omega)$ data. The CPE component is assumed to follow a first order extrapolation of the $Y^{far}(2\omega)$ signal from a DC potential before the faradaic wave to a DC potential after the faradaic wave. This step is performed on both real and imaginary components of $Y^{far}(2\omega)$.

In summary, this section contains equations that can be used to determine the SH faradaic admittance, $Y^{cor,far}(2\omega)$, from the SH measurements in the presence of R_u. In order to apply these equations and to find $Y^{cor,far}(2\omega)$, four quantities, the FH and SH potential and current, $E^{measured}(\omega)$, $I^{measured}(\omega)$, $E^{measured}(2\omega)$ and $I^{measured}(2\omega)$, must be determined. In addition, R_u from high frequency experiments and the CPE admittance $Q(\omega\times 2)$ from FH ACV with a frequency twice that applied to generate four quantities above must be known. It is also necessary to monitor $E^{measured}(2\omega)$ and to demonstrate that the contribution of the second term in Eq. 2.4 is negligible.

4. Experimental Section

Chemicals, gold electrode and electrochemical cell. Electrochemical experiments were performed with 1 mM $Ru(NH_3)_6^{3+}$ in 1 M Na_2SO_4 and 30 mM TRIS buffer, pH

adjusted to 6.5 with H_2SO_4. The gold electrode was prepared by melting a piece of gold wire in the Bunsen burner to form a bead. The electrode was flame-annealed just prior to the experiment. The estimated geometric area of the bead gold electrode was 0.1 cm^2. Electrochemical experiments were performed in a three-compartment electrochemical cell with a high surface area platinum mesh electrode and a SCE reference electrode.

Experimental Setup for first and second harmonic experiments and data collection. The FH and SH experiments were performed simultaneously by using an EG&G 273 potentiostat and EG&G 7220 DSP and 5210 Lock-in Amplifiers (LIA). These instruments were controlled via the GPIB interface using a C++ program. The program incorporated the device-level functions (NI-488.2M National Instruments Corporation software for instrument control) and three sets of commands specific for each instrument. The program performed the setting of all operating parameters for all three instruments according to data in an input file. The collected data were recorded in an output file for further processing.

Figure 2.2 demonstrates the experimental setup. The potentiostat was set up to apply a DC potential. The 7220 DSP LIA was set up to generate a *ac* potential applied to the *ac* input on the rear panel of EG&G 273 and, at the same time, to provide a TTL signal to drive the 5210 LIA. The amplitude of $E^{measured}(\omega)$ was typically 8 mV RMS. Under this condition, $E^{inter}(\omega)$ was high enough to generate $I^{measured}(2\omega)$ without significant generation of signals at higher even harmonics. The DSP 7220 LIA and 5210 LIA were set up for the SH and FH measurements, respectively. Use of two LIAs afforded a considerable reduction of the experimental time necessary to make the FH and SH

measurements, since each LIA remained tuned to its frequency, ω or 2ω. The EG&G 273 *ac* multiplex output was switched sequentially between *ac* current and *ac* potential. Therefore, at each DC potential, four quantities, the FH and SH potential and current, were determined: $E^{measured}(\omega)$ and $E^{measured}(2\omega)$ first, and then $I^{measured}(\omega)$ and $I^{measured}(2\omega)$. Measurements were performed in respect to the same reference phase. The time constants on the DSP 7220 LIA and 5210 LIA were 500 and 300 ms, respectively. Measurements were performed after signals settled down for a time period equal to 7 time constants. 30 samples were collected and averaged to get a single data point. In order to compensate for the LIA oscillator nonideality (SH distortion specified -70 dB), a differential input (the potentiostat electrometer output minus the LIA oscillator output) was used to measure the SH potential $E^{measured}(2\omega)$. This compensation is valid only if the doubled perturbation frequency is lower than the cut-off frequency of the potentiostat power amplifier. The FH and SH measurements were repeated over a DC potential range with a DC potential step being 5 mV.

Data processing, representation and comparison of experimental FH and SH Faradaic admittance with theory. FH ACV data are reported in three formats. The first is the measured admittance, $Y^{measured}(\omega)$, (the ratio of $I^{measured}(\omega)$ to $E^{measured}(\omega)$) as a function of DC potential. The second is the interfacial admittance, $Y^{inter}(\omega)$, vs. DC potential. $Y^{inter}(\omega)$ is calculated as follows:

$$Y^{inter}(\omega) = ((E^{measured}(\omega) / I^{measured}(\omega)) - R_u)^{-1} \quad (2.7)$$

In the third format, data are represented as faradaic admittance, $Y^{far}(\omega)$, vs. DC potential. $Y^{far}(\omega)$ is calculated as $Y^{inter}(\omega)$ minus the CPE admittance. The CPE admittance is found by the first or second-order extrapolation of $Y^{inter}(\omega)$ from a DC potential before the faradaic wave to a DC potential after the faradaic wave. The DC potential range should extend at least 200 mV beyond the half-wave potential in both directions in order to define the CPE admittance. This procedure is applied to both the real and imaginary parts of $Y^{inter}(\omega)$.

The collected SH ACV data, $I^{measured}(2\omega)$ and $E^{measured}(2\omega)$, were processed according to Eqs. 2.4-2.6. The experimental FH and SH faradaic admittances were compared with the theory according to the expressions published by Smith.[5,10] The published equations for the SH faradaic admittance define its absolute value and cotangent. Since cotangent has the same value in two opposite quadrants, there is some ambiguity with the signs of the real and imaginary parts of the SH faradaic admittance. The real part was defined to be positive at DC potentials negative of the half-wave potential and to be negative at DC potentials positive of the half-wave potential. The opposite convention was used by Smith.[10]

The minimized function was the sum of squared differences between the experimental data (real and imaginary parts of the FH or SH faradaic admittance) and theoretical values at the same DC potentials. The optimization parameters for the FH data were the half-wave potential ($E_{1/2}$, V), the product of the electrode area and redox species bulk concentration ($A \times C$, mole/cm), and the standard rate constant (k^0, cm/s). The optimization function for the FH data was found to be insensitive to the value of the

transfer coefficient ($0.3 \leq \alpha \leq 0.7$). Therefore, the transfer coefficient was not used as an optimization parameter and was assumed to be 0.4 based on the results of SH ACV experiments. In contrast to the FH case, the optimization program for the SH data included the transfer coefficient as an optimization parameter. The diffusion coefficient (D) was assumed to be 7×10^{-6} cm^2/s for both oxidation states.[11]

R_u measurements. R_u measurements were performed at frequencies between 10 kHz and 100 kHz at DC potentials where there was no faradaic reaction. At this frequency range, R_u is equal to the real component of the total cell impedance. The measurements were performed using an EG&G 273 potentiostat and an EG&G 5210 LIA controlled via the GPIB interface using EIS M398 software.

5. Results and discussion

5.1. FH Faradaic Admittance

Figures 2.3, 2.4, 2.5 show FH measured admittance $Y^{measured}(\omega)$, FH interfacial admittance $Y^{inter}(\omega)$ and FH faradaic admittance $Y^{far}(\omega)$ collected with 1600 Hz perturbation frequency. As can be seen on these plots, corrections for both R_u (12.2 Ω) and CPE admittance are important to obtain the faradaic admittance wave. The optimization results for 1600 Hz and a number of other frequencies are summarized in Table 2.1. The $Y^{far}(\omega)$ fit over a frequency range from 100 Hz to 1600 Hz results in the same value of $E_{1/2}$ and similar values of $A\times C$ and k^0. Data at frequencies lower than 100

Hz do not carry any kinetic information, e.g., the system is close to *ac* reversibility and the phase of faradaic admittance approaches 45°. At frequencies higher than 1600 Hz, a small uncertainty in the value of R_u results in a large uncertainty in $Y^{far}(\omega)$.

Table 2.1. FH faradaic admittance fit results

frequency / Hz	$E_{1/2}$ / V	$A \times C \times 10^8$ / mole/cm	k^0 / cm/s
100	-.291	7.39	0.577
200	-.291	7.35	0.520
400	-.291	7.23	0.518
800	-.291	7.17	0.604
1600	-.291	7.07	0.596
average	-.291	7.24±0.13	0.56±0.04

In addition to the $Y^{far}(\omega)$ fit at a single frequency, the linear dependence of the cotangent of the faradaic admittance phase at $E_{dc} = E_{1/2}$ vs. $\sqrt{\omega}$ can be used to find k^0 according to the following equation.[1]

$$Real\,(Y^{far}(\omega))/Imag\,(Y^{far}(\omega)) = Cotangent\,[\theta] = 1 + \sqrt{(D \times \omega/2)}/k^0 \qquad (2.8)$$

Figure 2.6 demonstrates the experimental data and results of the linear regression analysis. k^0 is determined to be 0.60±0.05 cm/s which is consistent with Table 2.1. Finally, it is important to mention that the electrolyte composition was carefully chosen to minimize the redox couple adsorption. Under the other conditions, for example, at pH

higher than 7.5 the faradaic admittance cannot be modeled according to the same theoretical equations[5] because of the shoulder appearing at a DC potential about 30 mV more positive of $E_{1/2}$.

5.2. SH Faradaic Admittance

Figures 2.7 and 2.8 demonstrate measured SH data $I^{measured}(2\omega)$ and $E^{measured}(2\omega)$ collected simultaneously with the data in Figure 2.3. Figure 2.9 shows $I^{far}(2\omega)$ calculated according to Eq. 2.4. A comparison between Figures 2.7 and 2.8 allows us to conclude that the contribution of the second term in Eq. 2.4 is negligible. $Q(\omega\times 2)$ is about two times larger than the CPE admittance shown at Figure 2.4, because $Q(\omega\times 2)$ is determined at the frequency twice of that used in the FH ACV experiment (Figure 2.4). Therefore, the product of $E^{measured}(2\omega)\times Q(\omega\times 2)$ is at least 50 times less than $I^{measured}(2\omega)$. The first term in Eq. 2.4, $I^{measured}(2\omega)\times(1+R_u\times Q(\omega\times 2))$, defines the shape of $I^{far}(2\omega)$.

The FH interfacial potential, $E^{inter}(\omega)$, is calculated according to Eq. 2.6 and shown in Figure 2.10. Division of $I^{far}(2\omega)$ by $((E^{inter}(\omega))^2\times\sqrt{2})$ results in $Y^{far}(2\omega)$ (Figure 2.11). Finally, a small background component due to the slight CPE nonlinearity is subtracted to obtain $Y^{cor,far}(2\omega)$ as demonstrated in Figure 2.12. As can be seen from these plots, the shapes of the initial $I^{measured}(2\omega)$ (Figure 2.7) and final $Y^{cor,far}(2\omega)$ (Figure 2.12) data are dramatically different. The shape of $Y^{cor,far}(2\omega)$ is qualitatively similar to that predicted for the *ac* quasi-reversible case, e.g., the absolute value of the imaginary component is larger than the absolute value of the real component and the real and

imaginary components have opposite signs.

As with $Y^{far}(\omega)$ data, $Y^{cor,far}(2\omega)$ data were fitted to the theoretical expressions for the *ac* quasi-reversible case.[5,11] The optimization results ($A\times C$, k^0, α) over a range of frequencies are summarized in Table 2.2. $E_{1/2}$ was found to be the same as in FH ACV and is not shown in Table 2.2. The high sensitivity of SH ACV to the kinetic status of the faradaic process allows the determination of the transfer coefficient (α).

Although there is a good qualitative agreement between experimental and theoretical $Y^{cor,far}(2\omega)$ data, the quantitative analysis does not yield exactly the same information on the faradaic process as analysis of FH ACV. The product of $A\times C$ ($7.69\pm0.07\times10^{-8}$ mole/cm) is about 5% higher than that found by FH ACV ($7.24\pm0.13\times10^{-8}$ mole/cm). The value of k^0 determined by SH ACV (0.49±0.02 cm/s) is about 9% smaller from that determined by FH ACV (0.56±0.04 cm/s).

Table 2.2. SH faradaic admittance fit results

frequency / Hz	$A\times C\times10^8$ / mole/cm	k^0 / cm/s	α
100	7.73	0.466	0.28
200	7.60	0.479	0.33
400	7.78	0.477	0.38
800	7.67	0.505	0.41
1600	7.66	0.517	0.44
average	7.69±0.07	0.49±0.02	0.38±0.07

Despite the slight discrepancies, the overall conclusion is the suggested procedure

to process the SH data in the presence of uncompensated resistance is valid because FH and SH results are essentially the same. Nevertheless, it would be worthwhile to point out to two sources for the slight discrepancy. First, the theoretical expressions for the FH and SH faradaic admittance used in this paper are valid if the faradaic process is controlled only by diffusion and the charge transfer. Even though the electrolyte composition was carefully chosen to minimize adsorption of $Ru(NH_3)_6^{3+}$, the discrepancy between the FH and SH faradaic admittance may be due to small adsorption effects detected by SH ACV because of its higher sensitivity to the kinetic status of the faradaic process. Second, the linear or second order background correction for the CPE admittance in FH ACV may affect the accuracy of the faradaic admittance data. In addition, the linear background correction for the slightly nonlinear CPE used to convert the $Y^{far}(2\omega)$ (Figure 2.11) to $Y^{cor,far}(2\omega)$ (Figure 2.12) may also introduce some uncertainty.

The suggested procedure to process the SH data was also applied to a dummy cell *R(CD)* with 15 Ω resistor (*R*), 1 μF capacitor (*C*) and a diode (*D*). The FH and SH diode admittance were determined to be real (positive) and imaginary (negative), respectively. Both FH and SH diode admittance were determined to be frequency (up to 1 kHz) and perturbation amplitude (8-10 mV RMS) independent.

6. Conclusions

It has been previously demonstrated that SH faradaic admittance measurements can be obtained free from interference from non-faradaic elements only if either complete positive feedback compensation or low perturbation frequencies (*iR* drop is insignificant) are used. A data processing procedure is suggested in this research project to analyze SH data collected at high perturbation frequencies and in the presence of *iR* drop. The procedure is validated by comparisons of the product $A \times C$ and the standard rate constant k^0 computed independently from FH and SH simultaneous experiments. The high sensitivity of SH ACV to the kinetic status of the faradaic process allows one to determine additional kinetic information (the transfer coefficient) that is not obtainable in this case from FH ACV. However, the complexity of the experimental setup and data processing for SH ACV make FH ACV a preferred method to analyze faradaic processes, especially if a faradaic process is a combination of mass transfer, adsorption and coupled chemical and charge transfer reactions.

References

1. D. E. Smith, in: A. J. Bard (Ed.), Electroanalytical Chemistry, Marcel Dekker, vol. 1, New York, 1966, pp. 1-155.
2. T. G. McCord, D. E. Smith, Anal. Chem. 40 (1968) 1959.
3. M. Sluyters-Rehbach and J. H. Sluyters, in: B. E. Conway, J. O'M. Bockris, E. Yeager and S. Sangarapani (Eds.), Comprehensive Treatise of Electrochemistry, vol. 9, Plenum, New York, 1984, p. 177.
4. D. A. Harrington, Can. J. Chem. 75 (1997) 1508.
5. T. G. McCord, D.E. Smith, Anal. Chem. 40 (1968) 289.
6. C. Senarathe, K. Hanck, J. Electroanal. Chem. 338 (1992) 31.
7. L. Meszaros, G. Meszaros, B. Lengyel, J. Electrochem. Soc. 141 (1994) 2068.
8. R. W. Bosch, W. F. Bogaerts, J. Electrochem. Soc. 143 (1996) 4033.
9. M. C. H. McKubre, B. Syrett, in: G. C. Moran, P. Labine (Eds.), Corrosion Monitoring in Industrial Plants using Nondestructive Testing and Electrochemical Methods, American Society for Testing and Materials, Philadelphia, 1986, pp. 433-458.
10. A. M. Bond, R. J. O'Halloran, I. Ruzic, D. E. Smith, Anal. Chem. 48 (1976) 872.
11. S. Licht, V. Cammarata, M. S. Wrighton, J. Phys. Chem. 94 (1990) 6133.

Figure 2.1. A generic electrical circuit: R_u, uncompensated resistance, CPE, constant phase element, Z_f, faradaic impedance. $E^{measured}(2\omega)$ is the SH measured potential between the reference and working electrodes. $I^{measured}(2\omega)$ is the SH measured current which flows through the uncompensated resistance; it is the current detected by the current follower of the potentiostat. $I^{far}(2\omega)$ is the SH faradaic current generated by the nonlinear faradaic element. $E^{inter}(\omega)$ is the FH interfacial potential which appears across the parallel combination of CPE and Z_f. The object of the SH experiment is to determine both $I^{far}(2\omega)$ and $E^{inter}(\omega)$.

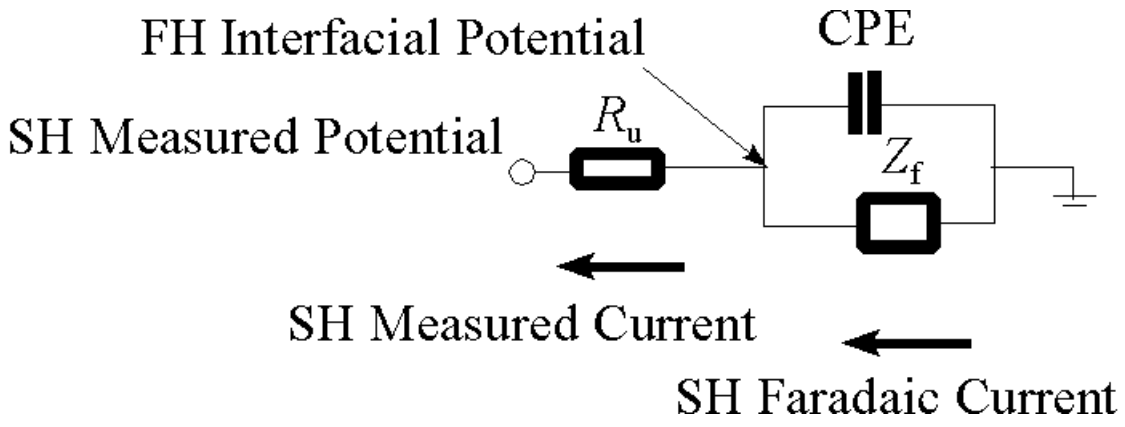

Figure 2.2. Experimental setup includes a computer with a C++ program that incorporates device level functions (NI-488.2M National Instruments Corporation software) and three sets of commands for each instrument. EG&G 5210 LIA is used for FH potential and current measurements. EG&G 7220 DSP LIA is used for SH potential and current measurements.

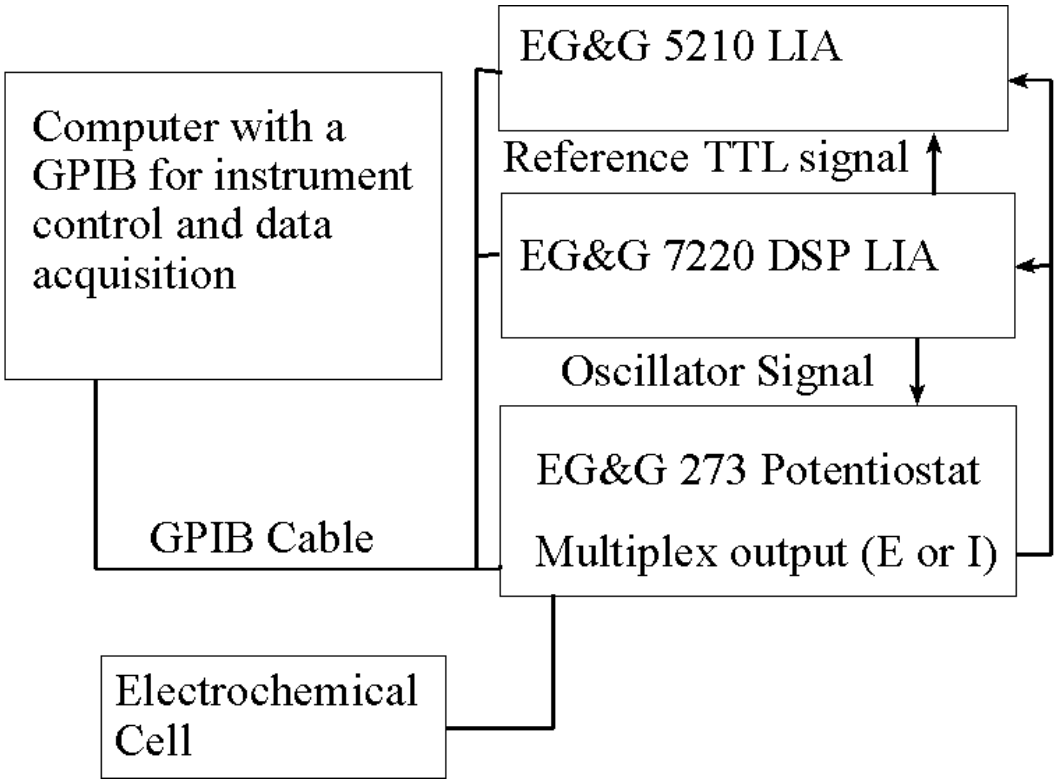

Figure 2.3. FH measured admittance, $Y^{measured}(\omega)$, of $Ru(NH_3)_6^{3+}$ at 1600 Hz. The DC potential range is from -50 mV to -480 mV vs. SCE.

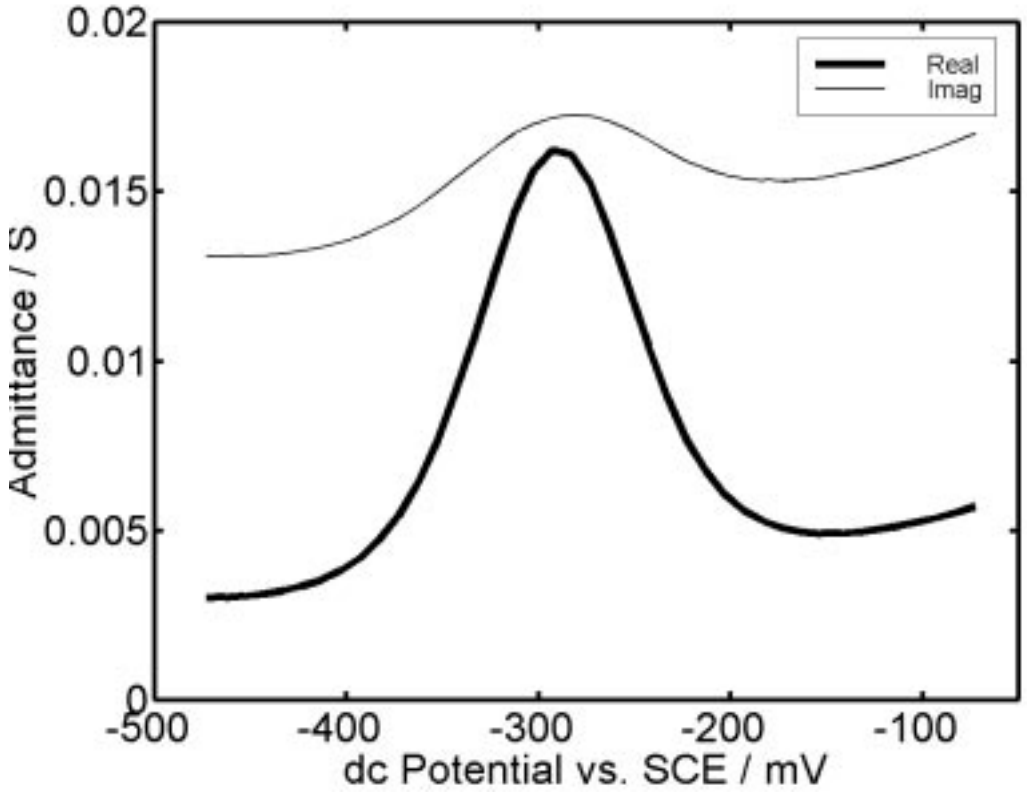

Figure 2.4. FH interfacial admittance, $Y^{inter}(\omega)$. $Y^{inter}(\omega)$ calculated according to Eq. 2.7. R_u = 12.2 Ω.

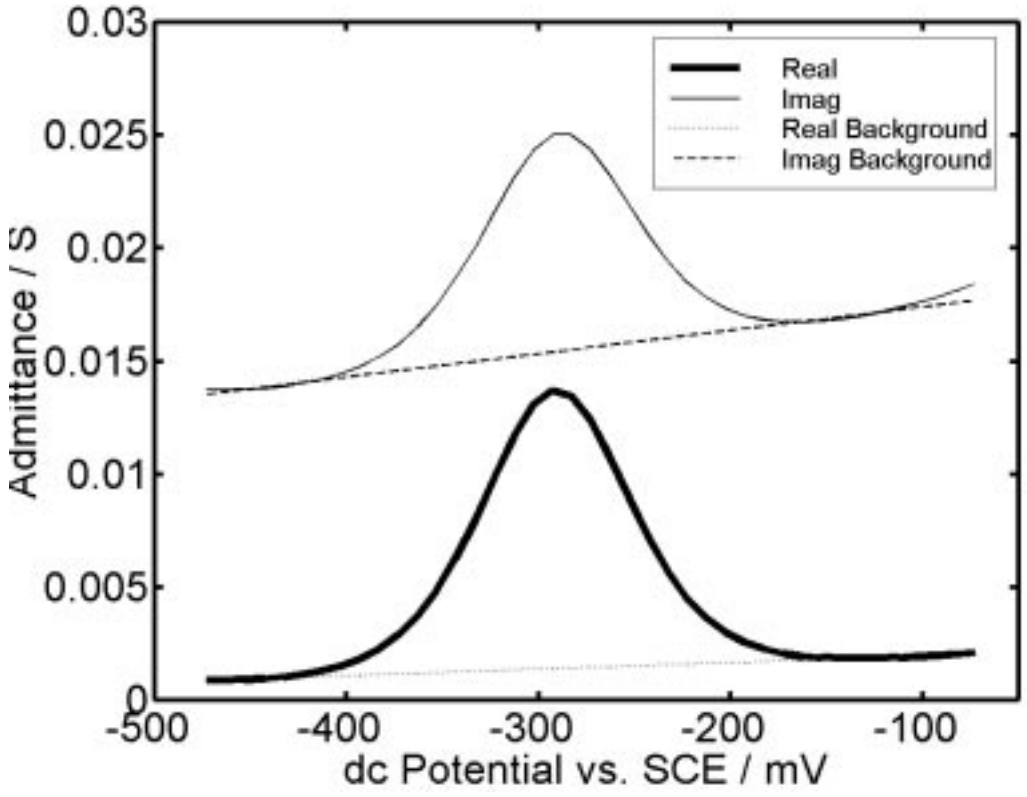

Figure 2.5. FH faradaic admittance, $Y^{far}(\omega)$. In contrast to Figures 2.3 and 2.4, experimental data are shown as points. Theoretical fits over a DC potential range used for optimization are shown as lines.

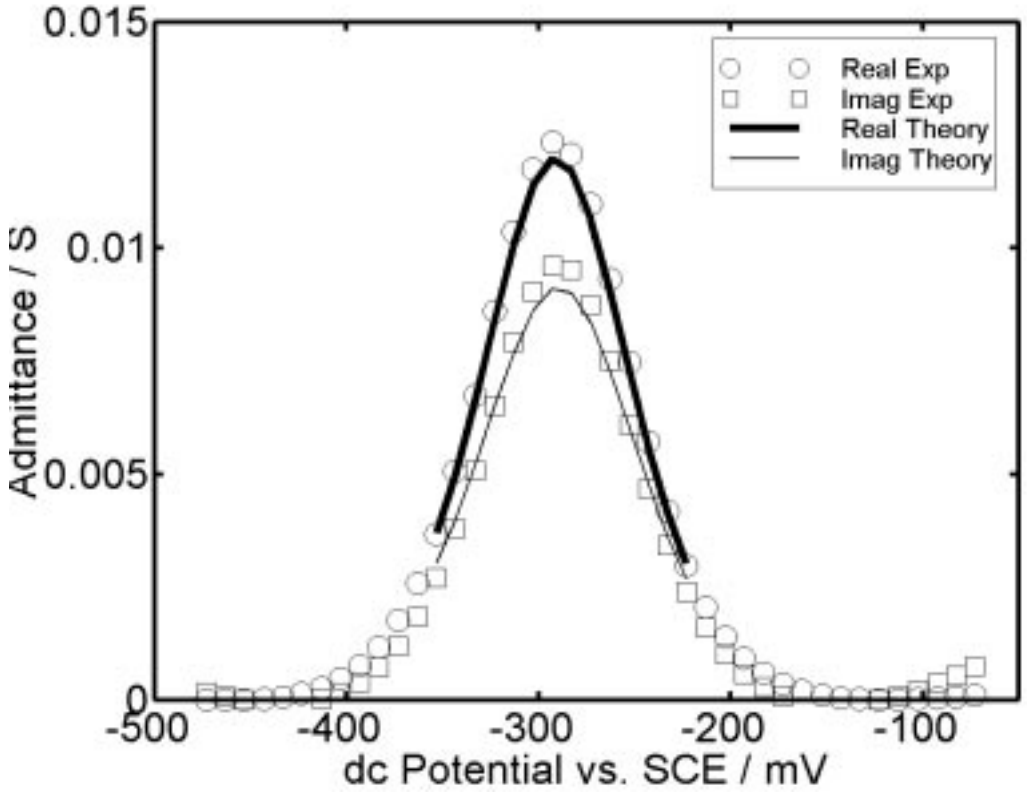

Figure 2.6. Cotangent of the FH faradaic admittance phase vs. angular frequency. Linear Regression results are: intercept 1.003±0.014 and slope 0.0031±0.0002.

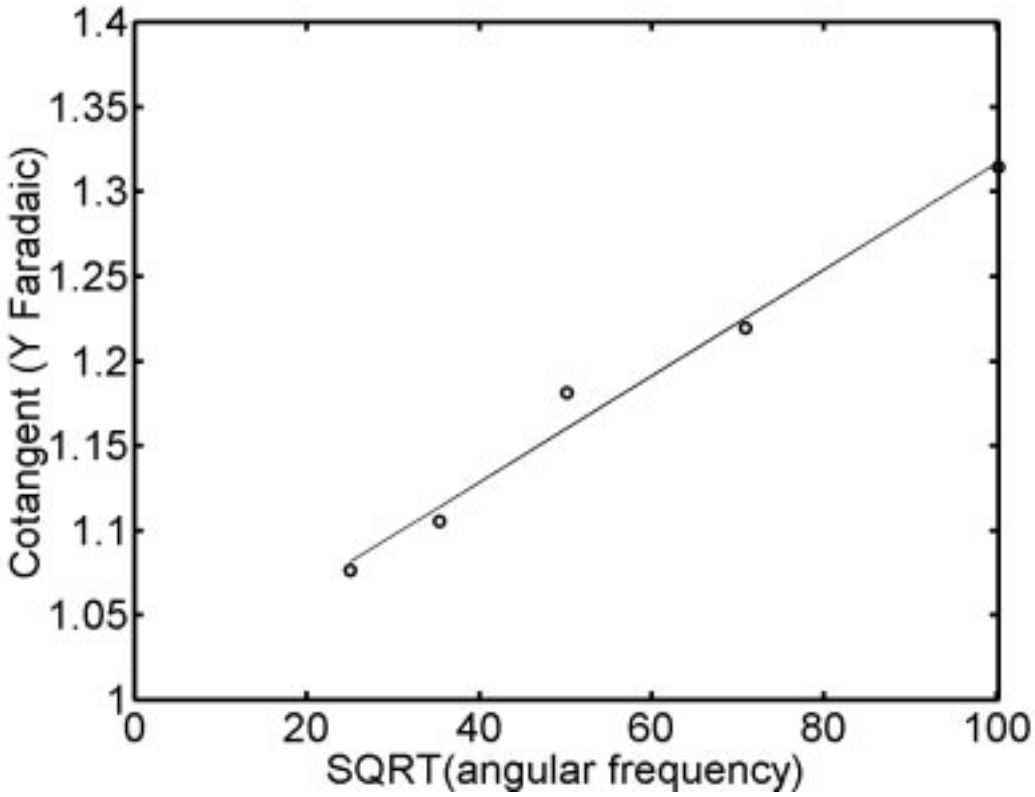

Figure 2.7. SH measured current, $I^{measured}(2\omega)$. $I^{measured}(2\omega)$ is collected at 3200 Hz simultaneously with data in Figure 2.3.

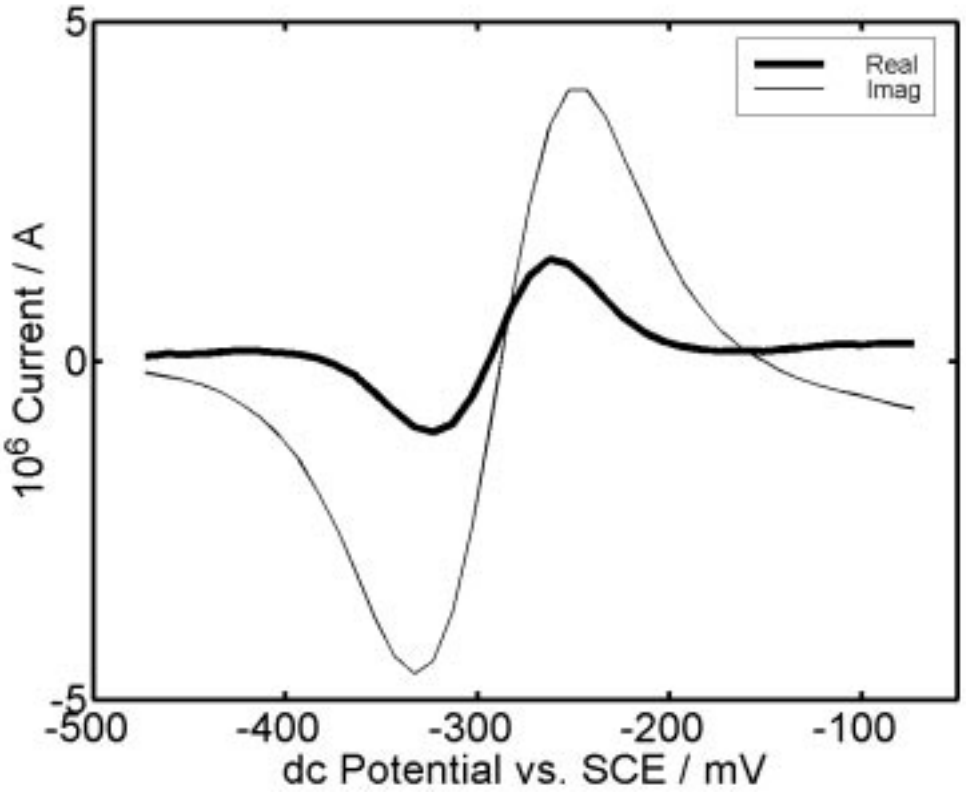

Figure 2.8. SH measured potential, $E^{measured}(2\omega)$. $E^{measured}(2\omega)$ is collected at 3200 Hz simultaneously with data in Figure 2.3.

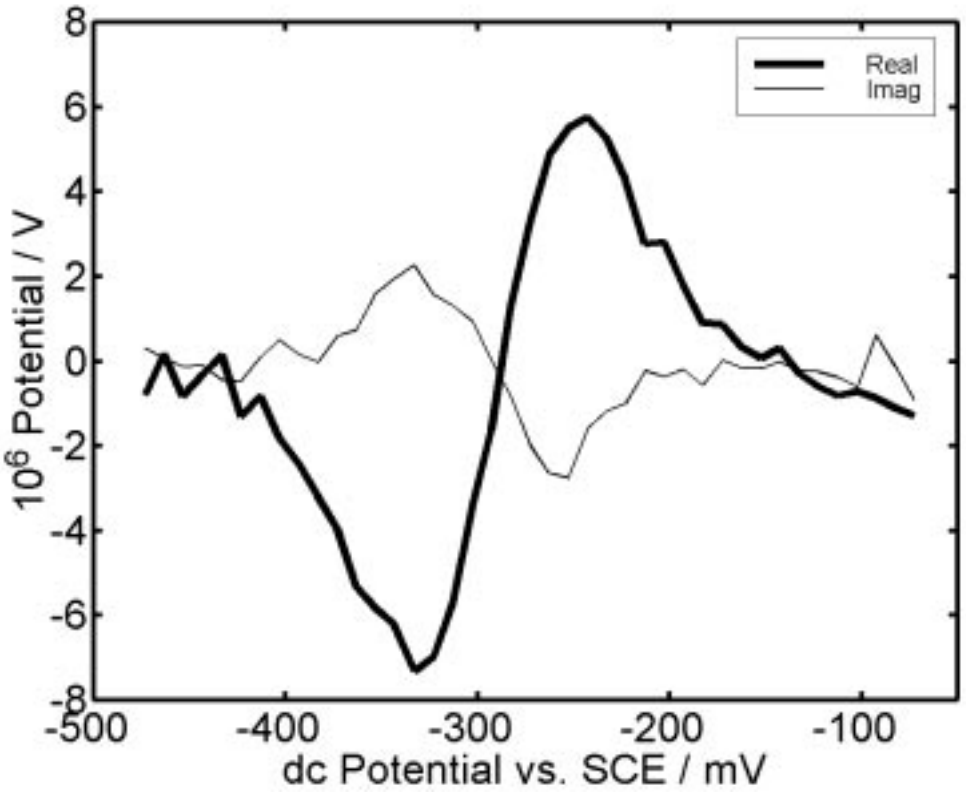

Figure 2.9. SH faradaic current, $I^{far}(2\omega)$. $I^{far}(2\omega)$ is calculated according to Eq. 2.4.

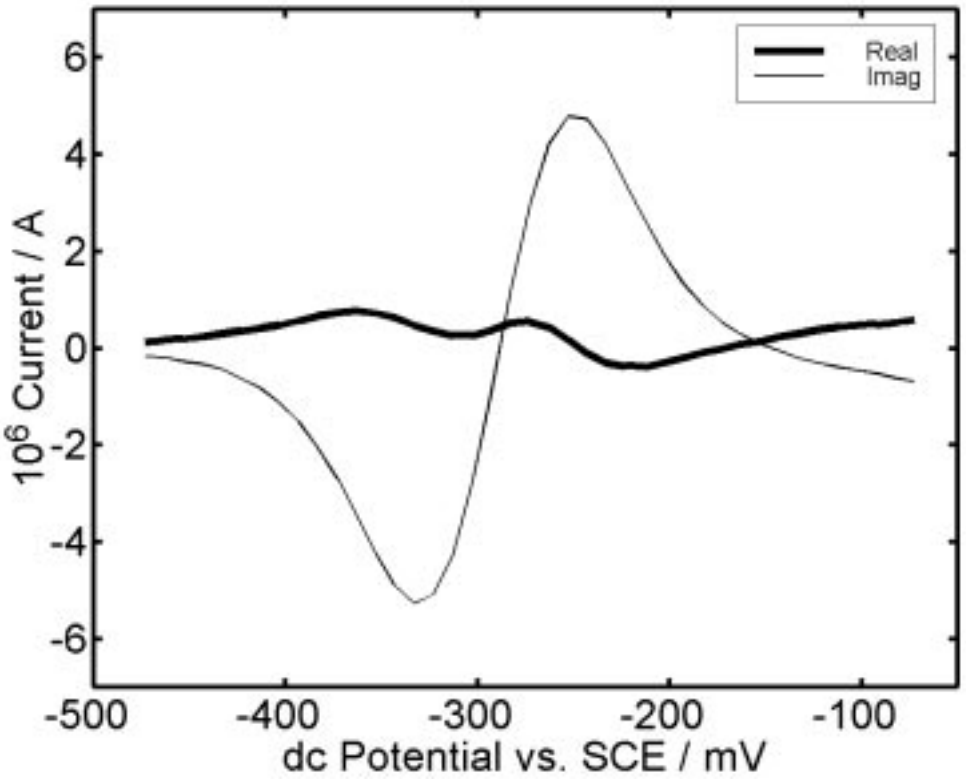

Figure 2.10. FH interfacial potential, $E^{inter}(\omega)$. $E^{inter}(\omega)$ is calculated according to Eq. 2.6.

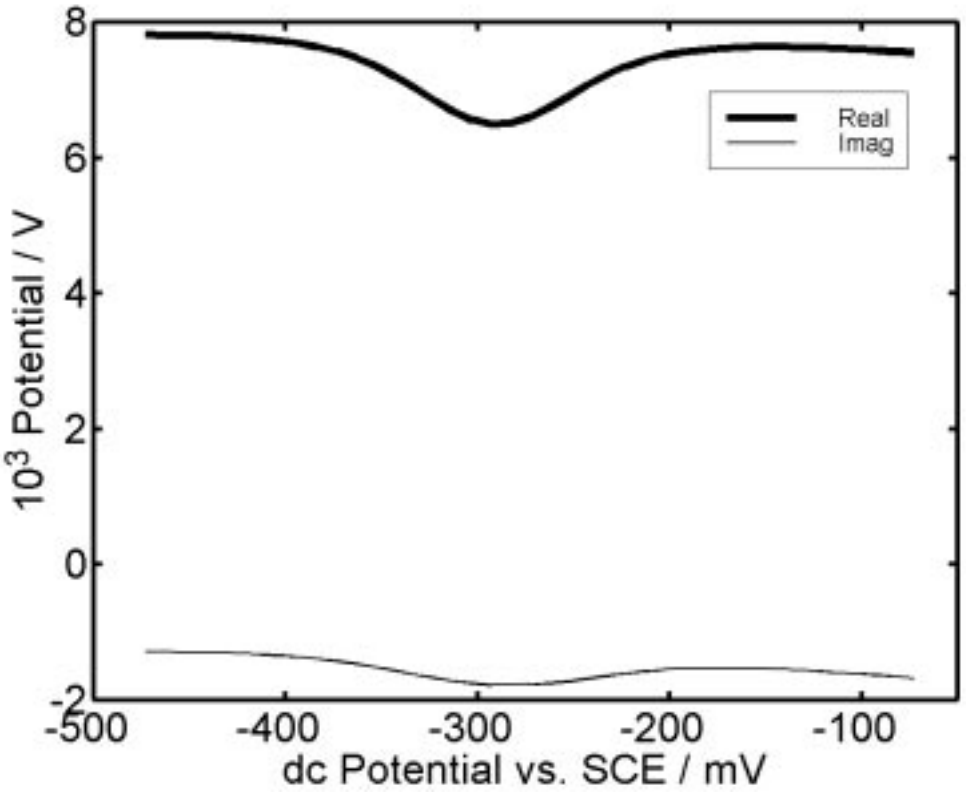

Figure 2.11. SH faradaic admittance, $Y^{far}(2\omega)$. $Y^{far}(2\omega)$ is calculated according to Eq. 2.5.

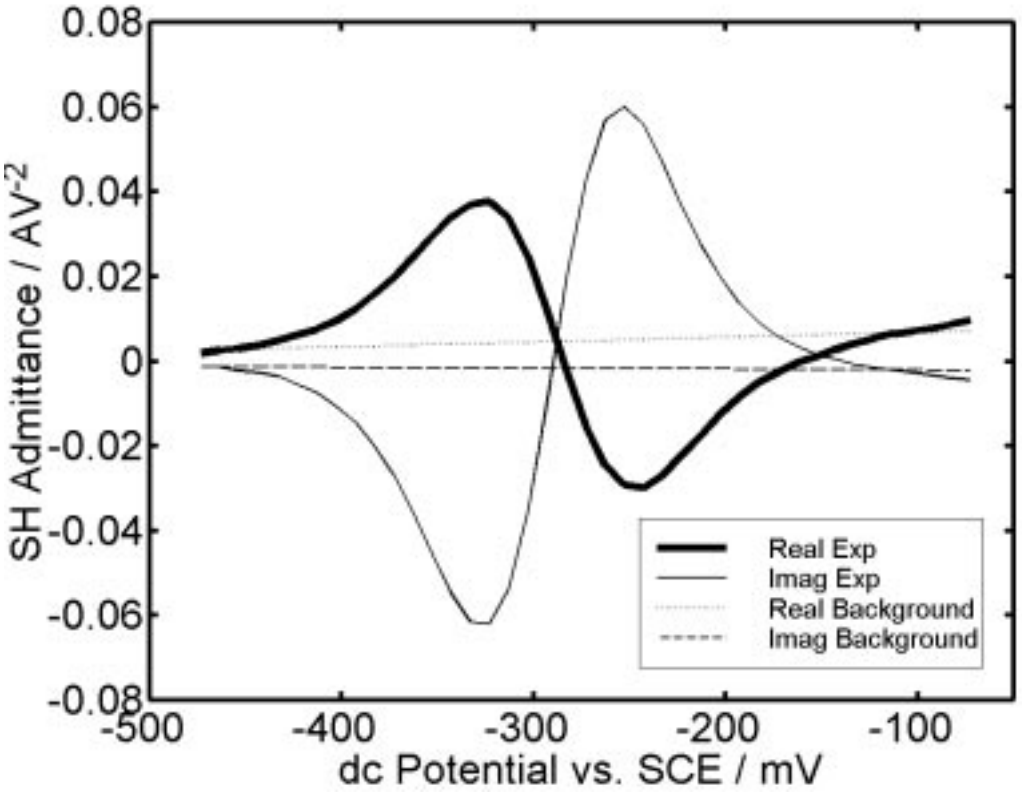

Figure 2.12. SH background corrected, faradaic admittance, $Y^{far,cor}(2\omega)$. In contrast to Figures 2.7-2.11 experimental data are shown as points. Theoretical fits over a DC potential range used for optimization are shown as lines.

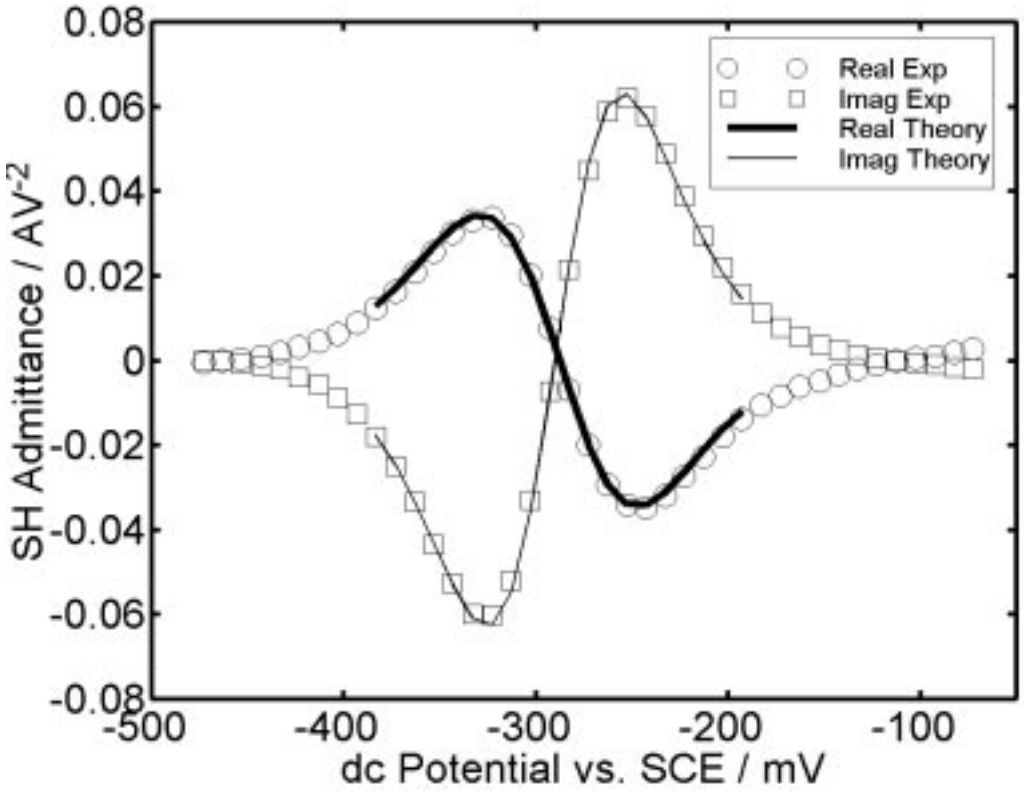

Chapter Three

Electrochemical and Electrochemically Modulated Reflectance AC Voltammetry Studies of Electron Transfer Kinetics between Attached Redox Centers and a Mirror Gold Electrode

1. Introduction

Kinetics of electron transfer between a metal electrode and redox centers attached to the electrode surface via alkanethiols has been the subject of intensive research for the last decade.[1-3] Electrochemical studies of these organized surface layers have been driven by both academic interest and the possibility of their practical applications. On one hand, self-assembled monolayers (SAMs) with attached redox centers (Figure 3.1) are excellent systems to test the Marcus theory of electron transfer.[4] On the other hand, SAMs have been suggested for use, for example, in sensor design, molecular electronics and other areas.[1]

Although many electrochemical methods have been developed to investigate kinetics of surface processes, those methods employing the superposition of a DC potential and the sinusoidal potential perturbation $\triangle E\sin(\omega t)$, such as AC Voltammetry (ACV) and Electrochemical Impedance Spectroscopy (EIS), have a number of experimental advantages: (a) correction for the uncompensated resistance (R_u), (b) correction for the limited bandwidth of the power amplifier of the potentiostat, (c) improved signal-to-noise ratio. The theory for the faradaic admittance $Y^{faradaic}$ of the

strongly adsorbed electroactive species in the case of a Langmuir isotherm was developed by Laviron [5] in the limit of small *ac* potential perturbation. The faradaic impedance $Z^{faradaic}$ is represented as a series combination of frequency-independent R_a and C_a, where R_a, the adsorption resistance, and C_a, the adsorption capacitance, are given by the following equations.[5]

$$R_a = (RT/n^2F^2Ak_s)[\alpha\Gamma_o\eta^{-\alpha} + (1-\alpha)\Gamma_r\eta^{1-\alpha}]^{-1} \quad (3.1)$$

$$C_a^{-1} = k_sR_a(\eta^{-\alpha} + \eta^{1-\alpha}) \quad (3.2)$$

Γ_o and Γ_r, the superficial surface concentrations of the oxidized and reduced forms in the absence of *ac* current, are given by the following equations:

$$\Gamma_o + \Gamma_r = \Gamma_{total} \quad (3.3)$$

$$\Gamma_o/\Gamma_r = \eta = exp[\ (nF/RT)(E_{dc} - E^{0'})\ ] \quad (3.4)$$

The faradaic admittance $Y^{faradaic}$ of the strongly adsorbed electroactive species is given by:

$$Y^{faradaic} = (Z^{faradaic})^{-1} = (R_a - j/(\omega C_a))^{-1} \quad (3.5)$$

In Eqs. 1-5, k_s is the standard rate constant, A is the electrode area, $E^{0'}$ is the formal

potential and α is the transfer coefficient. All other variables have their usual meanings.

In contrast to the large number of publications devoted to EIS, only a few papers have been published on the application of ACV to investigate electron transfer kinetics between either strongly adsorbed electroactive species [5-7] or attached redox centers [8] and metal electrodes. The experimental faradaic admittance data for the surface reactions have been observed to deviate from the theoretical curves applicable in the case of a Langmuir isotherm.[8] These deviations may be explained by redox center interactions due to attraction or repulsion forces between adsorbed molecules, e.g. when the adsorption process obeys a Frumkin isotherm.[6,9,10] An alternative explanation may be a distribution of formal potentials [11] or a distribution of standard rate constants and reorganization energies [8,12-15], so-called thermodynamic or kinetic heterogeneity.

In order to supplement electrochemical methods based upon *ac* potential perturbation and to obtain complementary information on kinetics of the surface electrode processes, different *in-situ* spectroscopic techniques have also been employed. In electroreflectance spectroscopy [16-25], a monochromatic light beam is reflected from a mirror electrode, and the change of the reflected beam intensity in response to the *ac* potential modulation is monitored as a function of either the wavelength of light (λ) or the DC electrode potential (E_{dc}). The *ac* electroreflectance signal can be normalized, and the electromodulation reflectance coefficient [16] is defined in the time domain as:

$$\chi(\lambda, E_{dc}) = 1/R \times dR / dE \tag{3.6}$$

where *R* is the DC reflectance of the electrode surface, *dR* is the *ac* electroreflectance and *dE* is the interfacial *ac* potential (the total cell *ac* potential from the potentiostat electrometer corrected for *iR* drop).

Plieth et al. [17] suggested that the term *Potential Modulated Electroreflectance Spectroscopy* be used if the *ac* electroreflectance signal originates from the first atomic layer of the metal electrode surface. Plieth et al. [17] also recommended use of the term *Electrochemically Modulated Reflectance Spectroscopy* if the *ac* electroreflectance signal originates from electrochemical processes in the double layer. It has been shown that, in the presence of organic molecules adsorbed on a metal electrode, the contribution of the first atomic layer of the metal electrode to the *ac* electroreflectance signal is negligible.[16-25] Therefore, we prefer to use the term *Electrochemically Modulated Reflectance* to describe the spectrophotometric method employed in this project, even though the term *Potential Modulated Electroreflectance* has been applied by other authors [20-25] to describe electroreflectance phenomena in similar electrochemical systems.

In the presence of the SAM, the *ac* electroreflectance signal may originate from two independent phenomena in the interfacial region (the region composed of the the SAM and the adjacent electrolyte layer).[17-19] The first phenomenon results from modulation of the interfacial optical properties $(dR/dE)_\theta$ at a constant electrode coverage θ (where θ can refer to the coverage of either the alkanethiols or the total coverage of the redox centers or the coverage of a particular oxidation state of the redox centers). It is reasonable to assume that the coverage of the alkanethiols in the SAM and the total coverage of the redox centers do not change with applied potential. Electrochromism, the

modulation of the optical constants of the adsorbed molecules with the electric field in the interfacial region, contributes to the first phenomenon. For the investigated system, electrochromism is believed to be dominated by the modulation of the absorption coefficient (dk/dE) where k refers to either the oxidized form or the reduced form of the redox centers. As pointed out by Kim et al.,[26] the wavelength dependence of the absorption coefficient of the adsorbed species can be quite different from that inferred from the homogeneous absorption spectrum. The second phenomenon is due to modulation of the electrode coverage of, for example, the reduced form of the redox centers $\theta_{red} = \Gamma_{red} \times A$ (mol) with the interfacial *ac* potential which is caused by faradaic reactions ($d\theta_{red}/dE$). In this case, the *ac* electroreflectance signal arises if the difference between the absorption coefficients ($\triangle k = k_{red} - k_{oxi}$) of the reduced and oxidized forms is not zero. These two effects are combined in Eq. 3.7.[17-19]

$$\chi(\lambda, E_{dc}) \sim (dR / dE)_{\theta} + (\partial R / \partial \theta)_{E} \times (d\theta_{red} / dE) \sim$$
$$(dk / dE)_{\theta} + \triangle k(E_{dc}) \times (d\theta_{red} / dE) \qquad (3.7)$$

Consequently, Electrochemically Modulated Reflectance AC Voltammetry (EMR ACV) provides access to two types of information about surface redox reactions, electron transfer kinetics and the existence (or absence) of electrochromic effects. The electromodulation reflectance coefficient can be defined in the frequency domain as (X) and connected with χ via Fourier transformation $\mathcal{L}$. It is known that, if the *ac* electroreflectance signal originates only from modulation of the interfacial optical

properties (e.g. from the first term in Eq. 3.7), the phase angle between X and the interfacial *ac* potential E^{inter} is zero. In contrast, if the second term in Eq. 3.7 is the only contribution to the *ac* electroreflectance signal, the phase angle between X and faradaic admittance $Y^{faradaic} = \mathcal{L}\,(dI^{faradaic}/dE^{inter})$ is 90° because of the integral relationship shown in Eq. 3.8.[20]

$$\chi(\lambda, E_{dc}) \sim \Delta k(E_{dc}) \times (d\theta_{red} / dE) = \Delta k(E_{dc}) \times \int dI^{faradaic}/dE^{inter}\, dt / (n \times F) \qquad (3.8)$$

Eq. 3.8 can be rewritten in the frequency domain as:[20]

$$X(\lambda, E_{dc}) \sim \Delta k(E_{dc}) \times Y^{faradaic} / (n \times F \times j\omega) \qquad (3.9)$$

Therefore, the phase of X is located either −90° or +90° relative to the phase of $Y^{faradaic}$ depending upon the sign of $\Delta k(E_{dc})$. This is the condition needed in order to determine kinetic information for attached redox centers from EMR ACV experiments.

Although EMR ACV has been previously applied to investigate kinetics of electron transfer in the case of strongly adsorbed electroactive species[20-25], the merits of this method have not been completely demonstrated due to two reasons. First, EMR ACV is both theoretically and experimentally more complicated than electrochemical methods also based upon *ac* potential modulation (ACV and EIS). Second, kinetic data obtained by EMR ACV have been often difficult to reconcile with data collected by electrochemical methods. This fact may be due to uncertainties associated with the *iR*

drop correction.[20-22] Disagreement among kinetic data may also result from the peculiarities of the faradaic admittance for strongly adsorbed species such as (as stated above) interactions between redox centers and thermodynamic and kinetic heterogeneity. As a result, the faradaic process may appear to proceed with different rates at different time scales. For example, Gaigalas et al.[22] reported discrepancies in the standard rate constants determined by Cyclic Voltammetry (CV), EIS and EMR ACV. Gaigalas et al.[23] proposed a model for the interfacial dielectric properties that includes a series connection of a constant phase element (CPE)[27] to model the Helmholtz capacitance and a capacitor to model the diffuse double layer in order to obtain a frequency-independent standard rate constant. This model is not applicable in our case because the interfacial dielectric properties are dominated by the low dielectric constant of the alkyl chains and consequently the effects of the aqueous diffuse layer are believed to be negligible.

Another complication in the analysis of the EMR ACV data results from the fact that faradaic admittance is defined as a linear function which is, strictly speaking, valid only if the linearity condition is obeyed. However, EMR experiments are usually performed with a large amplitude *ac* potential perturbation (typically 50-100 mV RMS) which is necessary in order to increase the signal-to-noise ratio in the optical measurements. Under these circumstances, the equations derived by Laviron for the faradaic admittance are no longer applicable due to the effect of the nonlinear components on the faradaic current at the fundamental perturbation frequency. In order to overcome this complication, Niki et al.[21] derived equations for the *ac* electroreflectance signal due to the coverage modulation as a function of perturbation frequency using a

large amplitude *ac* potential perturbation. Sagara and Niki employed these equations for the frequency domain analysis of the *ac* electroreflectance signal to obtain the kinetic parameters of the faradaic process.[20,21,25] However, to our knowledge, Sagara has not reported the analysis of kinetic data obtained by simultaneous electrochemical ACV and EMR ACV. This analysis is necessary for comparison of the faradaic admittance phase obtained by the two methods and, therefore, for the valid determination of k_s by EMR ACV.

2. Objectives of this research project

The objectives of this research project are twofold. The first is to implement an accurate electrochemical method with a small amplitude *ac* potential perturbation (ACV) to determine the total coverage of redox centers (θ_{total}), the standard rate constant (k_s) and the transfer coefficient (α) in the presence of *iR* drop for the electron transfer reaction between Ru redox centers attached to the electrode surface and a mirror Au electrode. The second objective is to develop an experimental setup, data collection and processing method for EMR ACV in order to determine the phase correlation between the electromodulation electroreflectance coefficient and the faradaic admittance. As shown in Eq. 3.9, in the absence of the electrochromic effects, the phase angle between X and $Y^{faradaic}$ is expected to be 90°. In addition, k_s can be approximated from EMR ACV data with 20% accuracy [21] using Laviron's equations, [5] even though the experimental EMR ACV data are collected with a large amplitude *ac* potential perturbation at which the

linear relationship between E^{inter} and $I^{faradaic}$ is violated.

3. Experimental Section

Chemicals. All chemicals were used as received. Mercaptoundecanoic acid ($HS(CH_2)_{10}COOH$) and $[Ru(NH_3)_5(4\text{-aminomethylpyridine})]^{2+}$ (PF_6 salt) (abbreviated below as Ru(4AMP)) were available from previous research. The gold mirror electrodes (1×3 cm) were purchased from Evaporated Metal Films (Ithaca, N.Y.). The gold mirror electrodes were produced by evaporating 5 nm of Ti followed by 100 nm of gold onto float glass.

Self-assembled monolayer (SAM) deposition and Ru(4AMP) attachment. The electrode cleaning procedure started with electrode oxidation in the galvanostatic mode with a current density of 20 mA/cm^2 in 0.1 M $HClO_4$. The resulting gold oxide coating was dissolved in a dilute solution of HCl. The cleanliness of the gold electrode was established by performing a CV experiment in 0.1 M $HClO_4$. The sharp current rise at about +1.1 V vs. SCE corresponding to the formation of a gold oxide is indicative of the clean electrode surface. After reducing the oxide, the electrode was rinsed with DI water and then ethanol. Next, the electrode was immersed in a vial containing about 3 mg of $HS(CH_2)_{10}COOH$ in 10 mL of ethanol and stored overnight.

The coupling reaction of Ru(4AMP) to $HS(CH_2)_{10}COOH$ was carried out for 10-15 hours in 5 mM Na_2HPO_4 solution (sparged with argon), pH 7.0 adjusted with a dilute solution of H_3PO_4, with 0.15 g of 1-[3-(dimethylamino)propyl]-3-ethylcarbodiimide

hydrochloride, 0.15 g of KNO_3 and 3 mg of Ru(4-AMP). This procedure forms amide links between the Ru(4AMP) and the pendant COOH with minimum perturbation of the monolayer. Before ACV and EMR ACV experiments, the electrode was rinsed with ethanol and then DI water.

Electrochemical cell. Electrochemical ACV and EMR ACV experiments were performed in 0.5 M NaF (a nonadsorbing electrolyte) with pH adjusted to 5.0 with CF_3COOH. The solution was initially sparged with argon to remove dissolved oxygen and kept under a slow flow of argon during the experiment. Experiments were performed in a three-compartment electrochemical cell with a high surface area platinum mesh counter electrode and a SCE reference electrode. The cell was designed with two flat windows for the incident and reflected light beams. The angle of incidence was about 40°. The estimated area of mirror gold electrode immersed in the solution was 1.8 cm^2 for both ACV and EMR ACV experiments.

Experimental setup for electrochemical ACV and EMR ACV experiments. The small amplitude ACV experiments were performed using an EG&G 273 potentiostat and a 5210 Lock-in Amplifier (LIA). The large amplitude ACV and EMR ACV experiments were performed simultaneously by using the same instrumentation and a second LIA EG&G 7220 DSP. All three instruments were controlled via a GPIB interface using a C++ program. The program incorporated device-level functions (NI-488.2M National Instruments Corporation software for instrument control) and sets of commands specific for each of three instruments. The program performed the setting of all operating parameters for all three instruments according to data in an input file. The collected data

were recorded in an output file for further processing.

The experimental setup is shown in Figure 3.2. A 30 W tungsten lamp powered by a 6 V DC power supply was used as the light source. A tunable interference filter (Oriel 7155) was used to select the wavelength. With a slit width of 4 mm, the FWHM was 28 and 24 nm for 550 and 440 nm, respectively. The incident light beam was collimated and the reflected light beam was focused on the photodetector. No attempt was made to define the polarization of the light. An integrated photodiode and amplifier (Burr-Brown OPT 301) served as photodetector. The specified bandwidth of the photodetector (−3 dB) with the 1 MΩ feedback resistor was 4 kHz.

The potentiostat generated the applied DC potential. The 5210 LIA generated the *ac* potential applied to the *ac* interface input on the rear panel of EG&G 273 and, at the same time, provided a TTL signal to drive the 7220 DSP LIA. The EG&G 273 *ac* multiplex output was switched sequentially between *ac* current and *ac* potential. All three measurements, the total cell *ac* potential, the total cell *ac* current and the *ac* electroreflectance signal were performed with respect to the same reference phase. The time constants on the DSP 7220 LIA and 5210 LIA were 500 and 100 ms, respectively. After each DC potential change, measurements were delayed until signals settled down over a time period equal to 7 time constants. For each *ac* potential and current data point, ten samples were collected and averaged. In contrast, 400 samples were collected over a period of 10 seconds and averaged to get a single *ac* electroreflectance data point in EMR ACV. With this data collection procedure, noise figures for *d*R/R (unitless) were about 1×10^{-6} and 2×10^{-6} at 81 Hz and 31 Hz, respectively. The DC electroreflectance signal

was measured via an auxiliary ADC input on the 7220 DSP LIA. The ACV and EMR ACV measurements were repeated over a DC potential range with a DC potential step being either 10 or 20 mV.

Data processing, representation and comparison of experimental Faradaic admittance with theory. The data analysis procedure is based on an assumed equivalent circuit for the electrochemical cell. The equivalent circuit contains the uncompensated resistance R_u in series with a parallel combination of a CPE[27] and the faradaic admittance element. ACV data are reported in three formats. The first is the total cell admittance, $Y^{totalcell}$, (the ratio of $I^{totalcell}$ to $E^{totalcell}$) as a function of DC potential. The second is the interfacial admittance, Y^{inter}, vs. DC potential. Y^{inter} is calculated as follows:

$$Y^{inter} = ((Y^{totalcell})^{-1} - R_u)^{-1} \tag{3.10}$$

In the third format, data are represented as the faradaic admittance, $Y^{faradaic}$, vs. DC potential. $Y^{faradaic}$ is calculated as Y^{inter} minus the CPE admittance. The CPE admittance is found by first order extrapolation of Y^{inter} from a DC potential before the faradaic wave to a DC potential after the faradaic wave. The DC potential range was extended at least 200 mV beyond the formal potential in both directions in order to define the CPE admittance. This procedure was applied to both the real and imaginary parts of Y^{inter}.

Experimental $Y^{faradaic}$ data were compared with theoretical curves calculated according to Eqs. 1-5. The minimized optimization function was the sum of squared differences between the experimental (real and imaginary parts of $Y^{faradaic}$) and theoretical

data at the same DC potentials. The DC potential range for optimization was limited to $E^{0'} \pm 0.05$ V (the top half of the faradaic wave). The optimization parameters were the formal potential ($E^{0'}$, V), the total electrode coverage ($\theta_{total} = \Gamma_{total} \times A$, mol), the standard rate constant k_s (s^{-1}) and the transfer coefficient (α).

Data processing and representation of Electromodulation Reflectance Coefficient. The electromodulation reflectance coefficient was calculated as the ratio of *ac* electroreflectance signal to both the DC electroreflectance signal and the interfacial *ac* potential, E^{inter}, according to Eq. 3.6. E^{inter} was calculated according to Eq. 3.11.

$$E^{inter} = E^{totalcell} - I^{totalcell} \times R_u \tag{3.11}$$

R_u measurements and Cyclic Voltammetry (CV) experiments. R_u was measured at frequencies between 10 kHz and 100 kHz at DC potentials where there was no faradaic reaction. The measurements were performed by using the EG&G 273 potentiostat and EG&G 5210 LIA controlled via the GPIB interface using EIS M398 software. CV experiments were performed by using the EG&G 273 potentiostat and Headstart® software.

4. Results and Discussion

4.1. Electrochemical ACV

ACV experiments were performed with a small *ac* potential perturbation (4 mV RMS) in order to satisfy the linearity condition. Figures 3.3 (a, b, c) demonstrate total cell admittance $Y^{totalcell}$, interfacial admittance Y^{inter} and faradaic admittance $Y^{faradaic}$ collected with 231 Hz perturbation frequency. Figures 3.3 (a, b) show that correction for R_u (13.0 Ω) is important to obtain the true shape of the faradaic admittance wave. The imaginary part of $Y^{totalcell}$ has the double peak, whereas the imaginary part of Y^{inter} has only a single peak. After subtraction of CPE admittance and fitting $Y^{faradaic}$ to Laviron's equations, Figure 3.3 (c) shows that the experimental data and theoretical $Y^{faradaic}$ curves have slight but noticeable differences. Both the real and imaginary peaks of the experimental $Y^{faradaic}$ are slightly smaller and wider than corresponding theoretical peaks for a simple 1-electron surface redox process. Two of the four optimization parameters: (k_s, θ_{total}) determined over one decade of frequency are summarized in Table 3.1.

Both the formal potential, $E^{0'}$, (0.005 V vs. SCE) and transfer coefficient, α, (0.48) are found to be nearly constant for all frequencies and are not shown in Table 3.1. Although there is some deviation between the experimental and theoretical faradaic admittance data and, thus, some uncertainty in the values reported in Table 3.1, it is clear that the total coverage of redox centers (θ_{total}) appears to decrease and the standard rate constant (k_s) appears to increase as the perturbation frequency increases. Cyclic

voltammetry experiments (0.1 V/s) done immediately after the EMR ACV experiments yielded a coverage of 7×10^{-11} mol, which is comparable to the values reported in Table 3.1. Some evidence is provided below that thermodynamic or kinetic heterogeneity is a likely cause of the observed deviation of the experimental $Y^{faradaic}$ from the theoretical curves derived assuming no interactions between the redox centers (Langmuir isotherm). Kinetic heterogeneity is also believed to be the source of the discrepancy between the CV coverage and the ACV coverage. A more complete analysis of this problem was undertaken in a separated project reported in Chapter Four.

Table 3.1. Parameters for faradaic admittance determined for each perturbation frequency for one self-assembled monolayer.

frequency /Hz	k_s/ s^{-1}	$\theta_{total} = A\times\Gamma_{total}\times10^{11}$/ mole
31	337	8.42
51	354	8.27
81	383	7.81
101	399	7.45
131	423	7.11
171	458	6.61
201	480	6.39
231	478	6.38
Average	410±60	7.3±0.8

The average values of k_s, θ_{total} (Table 3.1) and α can be compared with previous measurements on this system.[13] The average total surface concentration, Γ_{total}, (as

determined by CV) is about 4-7×10^{-11} mol/cm^2, or roughly one-third of the maximum observed for a monolayer assembled with the pure thiol $HS(CH_2)_{10}CON(H)CH_2pyRu(HN_3)_5^{2+}$. At this surface concentration, the mean separation between redox centers is roughly 1.5 nm, which is more than twice as large as the diameter of the redox centers. This observation argues against significant interaction between redox centers as a cause of deviations between data and theory (Figure 3.3 (c)). The average k_s (400 s^{-1}) is significantly higher than the values previously reported (130-220 s^{-1}), obtained by cyclic voltammetry, chronoamperometry and EIS.[13] The source of this discrepancy is not yet known. The transfer coefficient α is close to 0.5, which is consistent with the symmetrical Tafel plots reported previously.[13]

The ACV data can also be analyzed at a single DC potential as a function of frequency. Figure 3.4 demonstrates the cotangent of the $Y^{faradaic}$ phase determined at $E^{0'}$ vs. angular frequency. According to Eq. 3.12, this plot should be linear.

$$Cot(\varphi) = Cot(Y^{faradaic}(E^{0'})) = \omega/(2\times k_s) \qquad (3.12)$$

The curvature is indicative of increasing apparent k_s with increasing frequency. Limiting slopes for low and high frequencies yield k_s values of 410 s^{-1} and 740 s^{-1}. Since the linear plots are expected for not only the Langmuir isotherm but also the Frumkin isotherm,[7] it is unlikely that interactions between redox centers (according to the Frumkin isotherm) cause the observed curvature in this plot (Figure 3.4).

Finally, it is worthwhile to note that the system under investigation possesses

temporal stability only for a period of 30 minutes, which is long enough to perform about 6 ACV experiments. If ACV experiments with the same perturbation frequency are repeated over a six hour period, the total coverage of redox centers (θ_{total}) decreases by about 30% and the standard rate constant (k_s) increases by about 15%. This trend may have some effect on the θ_{total} and k_s values reported in Table 3.1. However, these ACV experiments were completed in less than an hour; hence, the effect of temporal instability on the data in Table 3.1 is believed to be minor.

4.2. Electrochemically Modulated Reflectance ACV (EMR ACV).

Figure 3.5 demonstrates the UV-VIS spectra of soluble reduced and oxidized forms of the Ru(4AMP) complex in 5 mM Na_2HPO_4 solution, pH 7.0. Only the reduced form has an intense absorption band around 430 nm (k_{red} *ca.* 8000 $M^{-1}cm^{-1}$). Thus, the system is quite favorable for EMR ACV experiments because of a large difference in the absorption coefficients $\triangle k(E_{dc})$ at 430 nm (Eq. 3.7).

EMR ACV experiments were performed with a large amplitude *ac* potential perturbation (20 - 60 mV RMS) in order to obtain a high S/N ratio. Figures 3.6 (a, b, c) show the plots of *dR*/*R*, *dE* (both the total cell *ac* potential, $E^{totalcell}$, and interfacial *ac* potential, E^{inter}) and $\boldsymbol{X}$ collected at 440 nm and 81 Hz with 60 mV RMS *ac* potential perturbation. ACV were performed simultaneously with EMR ACV. Figure 3.7 (a) shows a comparison of $Y^{faradaic}$ at two different amplitudes of *ac* potential perturbation. As expected, the shapes of $Y^{faradaic}$ collected with 40 mV and 60 mV are somewhat

different.[21] In particular, both the real and imaginary peaks get broader and the peak heights are diminished for the large amplitude *ac* potential perturbation. Therefore, Eq. 3.12 is no longer accurate for calculating k_s. In discussion of simultaneous EMR ACV and ACV experiments, the term faradaic admittance, $Y^{faradaic}$, represents a ratio of faradaic *ac* current to interfacial *ac* potential for the sake of consistency with ACV alone and for brevity. Since admittance is defined as a linear function under conditions of a small amplitude perturbation, this usage, strictly speaking, is not correct.

Some experimental evidence is provided below that the electromodulation reflectance coefficient, X, is a more useful quantity to represent EMR ACV data than the ratio of the *ac* electroreflectance to DC electroreflectance, dR/R, used by Sagara and Niki [20,21,24,25] and Gaigalas.[22] Figures 3.7 (b, c) demonstrate that dR/R is proportional to the interfacial *ac* potential, E^{inter}. Therefore, it is natural to normalize dR/R with respect to E^{inter}, since E^{inter} is the driving force for the *ac* electroreflectance signal. Figures 3.7(a, c) demonstrate the same effect of a large amplitude *ac* potential perturbation upon both X and $Y^{faradaic}$ (e.g. peaks get broader and peak heights get smaller with a larger amplitude).

Gaigalas [23] performed an equivalent analysis to correct for iR drop but did not demonstrate that the corrected *ac* electroreflectance data scales with E^{inter}. Sagara and Niki [20] reported the analysis of dR/R in the complex plane (the imaginary part vs. the real part) at a single DC potential. In their method, *ac* electroreflectance data (dR/R) were compared with theory incorporating both R_u and the double layer capacitance (the values of these elements were assumed to be frequency-independent). For example, the analysis of dR/R free from the iR_u drop problem resulted in a semicircle analogous to the

semicircle observed for $Z^{faradaic}$ (a series combination of R_a and C_a) plotted in the complex admittance plane and, therefore, confined to a single quadrant in the complex plane. At the same time, incorporation of R_u in the data analysis produced a distorted semicircle which partially extended to another quadrant.[20] However, the usual method in electrochemical data analysis is to separate and analyze $Z^{faradaic}$ alone. In comparison to Sagara and Niki's method, determination of X via the approach suggested here allows the extraction of the phase of $Y^{faradaic}$ from the *ac* electroreflectance data and comparison of EMR ACV results directly with the $Y^{faradaic}$ theory. This approach also does not require explicit assumptions about the equivalent circuit for $Z^{faradaic}$. Consequently, the existence of kinetic heterogeneity is more readily observed (section 4.1 (Chapter Three) and Chapter Four).

An objective of EMR ACV experiments is to determine if there is any phase correlation between X and $Y^{faradaic}$.[28] Since $\triangle k$ is positive for the Ru(4AMP) complex in the homogeneous solution, the phase of X at 440 nm is anticipated to be between 270° and 360°. As shown in Figure 3.6 (c), the real part of X is positive and the imaginary part of X is negative. Both the real and imaginary components of X are almost zero at DC potentials 200 mV away from the half-wave potential (Figure 3.6 (c)). The plots of the X phase plus 90° and the phase $Y^{faradaic}$ are shown in Figure 3.8. The almost perfect overlap between these two plots indicates that, in this wavelength region, X is out-of-phase with $Y^{faradaic}$ within a few degrees of accuracy. In addition, the expression $X \times j\omega / Y^{faradaic}$ $(\sim \triangle k(E_{dc}) / (n \times F))$ at $E^{0'} \pm 100$ mV (Figure 3.7 (d)) has only the real non zero component over the entire DC potential range. This observation again confirms the 90° phase shift

between X and $Y^{faradaic}$. Therefore, for the investigated system at 420-440 nm, the *ac* electroreflectance signal exclusively originates from the second term in Eq. 3.7, specifically $\triangle k(E_{dc}) \times d\theta_{red}/dE$. The *ac* electroreflectance signal is overwhelmingly dominated by the modulation of the electrode coverage of a given redox state with the interfacial *ac* potential. Electrochromic effects are negligible. This result is consistent with the expectation that the strong electric field at the electrode/electrolyte interface resides within the low dielectric alkane region of the monolayer, leaving the redox center in a field-free region. Therefore, for this wavelength region (410 - 440 nm), the first term in Eq. 3.7 can be neglected and the *ac* electroreflectance signal can be described by Eq. 3.9.

As predicted by Eq. 3.9, the expression $X \times j\omega / Y^{faradaic}$ $(\sim \triangle k(E_{dc}) / (n \times F))$ at $E^{0'}$ ± 100 mV is found to be independent of ω (31, 51, 81 Hz) and dependent on wavelength. If the electrochromic effects, the first term in Eq. 3.7, were contributing to the *ac* electroreflectance signal, the $X \times j\omega / Y^{faradaic}$ independence of ω would be broken. This observation augments our conclusion that X is a more useful quantity than *dR/R* to represent the *ac* electroreflectance signal. The frequency dependence of X also supports our conclusion about the origin of *ac* electroreflectance signal. Plots at 31 and 51 Hz (data not shown) are similar to that at 81 Hz (Figures 3.6 (a, c)), except the signal-to-noise ratio is somewhat lower. Table 3.2 shows the phase of X plus 90° determined at $E^{0'}$ and k_s determined according to Eq. 3.12. As stated above, the applicability of Eq. 3.12 is compromised with a 60 mV *ac* potential perturbation and leads to about 10 - 20 % overestimation of k_s.[20] Therefore, the values of k_s reported in Table 3.2 are higher than

corresponding values in Table 3.1.

Table 3.2. The standard rate constants determined from the electromodulation reflection coefficient phase plus 90° at the formal potential with 60 mV *ac* potential perturbation.

frequency /Hz	Phase / degrees	Cotangent	k_s / s^{-1}
31	75	0.27	360
51	69	0.38	420
81	60	0.58	440

EMR ACV experiments were also performed at 540 nm and X is shown in Figure 3.9. In the wavelength region (500 - 600 nm), two phenomena are found to contribute to the *ac* electroreflectance signal. First, around the formal potential, there is a small contribution to the *ac* electroreflectance signal from the second term in Eq. 3.7 $\Delta k(E_{dc}) \times (d\theta_{red}/ dE)$ analogous to that observed at 400 - 440 nm, but with $\Delta k(E_{dc})$ being at least 20 times smaller. The large bandpass of the interference filter probably contributes to this signal. Second, the real component of X is not zero at DC potentials away from the half-wave potential. Separate experiments with an Au mirror coated with $HS(CH_2)_{10}COOH$ but without attached Ru(4AMP) complexes reveal that this signal is still present. The signal is in-phase with E^{inter} and does not depend on the perturbation frequency, but depends upon the wavelength. This component of the *ac* electroreflectance signal is about 5 times smaller at 440 nm than at 550 nm. Its exact physical origin is unknown. Nevertheless, we can conclude that, at 500 - 550 nm, the *ac* electroreflectance signal originates from two phenomena: the modulation of the interfacial optical properties

(dR/dE), which is in-phase with E^{inter}, and the modulation of the electrode coverage of a given redox state $\Delta k(E_{dc}) \times (d\theta_{red}/dE)$, which is out-of-phase with $Y^{faradaic}$.

5. Conclusions

Electrochemical ACV is used to investigate kinetics of electron transfer between a gold mirror electrode and Ru(4AMP) redox centers attached to the electrode surface via C_{10} alkanethiols. Corrections of the total cell admittance for both R_u and CPE admittance are important to determine accurately $Y^{faradaic}$. The standard rate constant, total coverage of redox centers and transfer coefficient are measured by small amplitude ACV with perturbation frequencies in the range 30 - 230 Hz under the assumption that the theoretical expressions developed by Laviron[5] are applicable. The standard rate constant (k_s) appears to increase as the perturbation frequency increases; discussion of this observation will be the subject of another paper.

ACV measurements of electron transfer kinetics are supplemented with EMR ACV measurements. The electromodulation reflectance coefficient, X, is demonstrated to be a more useful quantity than dR/R for representation of the *ac* electroreflectance data and determination of the kinetic status of the surface faradaic process. The phase of X is shown to be exactly out-of-phase with the phase of $Y^{faradaic}$ at wavelengths where the reduced form of the Ru(4AMP) complex strongly absorbs. Therefore, the *ac* electroreflectance signal originates from the coverage modulation of a given redox state with the interfacial *ac* potential and not from any electrochromism associated with the

effect of the electric field on the absorption coefficients of the redox centers.

Although the spectroscopic measurements of the X phase are shown to be in agreement with the measurements of the $Y^{faradaic}$ phase, accurate calculation of the standard rate constant from EMR ACV data is complicated. As is usually the case in the electroreflectance experiments, the need to increase the signal-to-noise ratio in the electroreflectance measurements requires the application of a large amplitude *ac* potential modulation that breaks down the linearity between E^{inter} and $I^{faradaic}$. Thus, $d\theta_{red}/dE$ is not a linear function of E^{inter}, even though $d\theta_{red}/dE$ is still a linear function of $Y^{faradaic}$ as shown in Eq. 3.8. Equations derived under the assumption of a small amplitude perturbation and applied to data collected with a large amplitude perturbation leads to overestimation of k_s. Under our experimental conditions and for the chosen electrochemical system ($Au/SC_{10}COOH$ ~ Ru(4AMP) complex), electrochemical AC Voltammetry is the preferred method to determine the kinetic status of the faradaic process.

Even though in our research project, the effort spent to develop the experimental setup and data processing procedure for EMR ACV definitely outweighed the value of the kinetic information, EMR ACV may prove to be more selective than electrochemical ACV in other circumstances. It is possible to imagine a situation in which ACV does not allow one to separate two faradaic processes that occur at the same thermodynamic and kinetic scales. In contrast, EMR ACV response may be selective, since in this case X is proportional to the sum of two weighted responses. Therefore, two faradaic processes may be separated due to a difference between $\Delta k_1(E_{dc})$ and $\Delta k_2(E_{dc})$. Ideally, a wavelength

can be selected at which one of the $\Delta k(E_{dc})$ terms is larger than the other one and kinetic information is obtained for one faradaic process. However, in order to completely realize this advantage, noise levels in both the light source and the photodetector must be diminished. In addition, a correction for *iR* drop (as reported in this paper) and an accurate estimate of the contribution of the first term in Eq. 3.7, $(dR/dE)_\theta$, (e.g. the modulation of the interfacial optical properties with the interfacial *ac* potential) to the *ac* electroreflectance signal are necessary in order to obtain kinetic information on the faradaic process.

Acknowledgment

This work was supported by the National Science Foundation grant CHE-9711779. The authors acknowledge some preliminary EMR ACV experiments with Au/S$(CH_2)_n$COOH ~ Ru complex performed by Prof. Takasama Sagara at Nagasaki University (Japan).

References

1. H. O. Finklea, in: A. J. Bard & I. Rubinstein (Eds.), Electroanalytical Chemistry, Marcel Dekker, vol. 19, 1996, p. 109.
2. C. E. D. Chidsey, Science 251 (1991) 919.
3. H. O. Finklea and D. D. Hanshew, J. Am. Chem. Soc. 114 (1992) 3173.
4. R. A. Marcus, J. Chem. Phys. 43 (1965) 679.
5. E. Laviron, J. Electroanal. Chem. 97 (1979) 135.
6. E. Laviron, J. Electroanal. Chem. 105 (1979) 25.
7. E. Laviron, J. Electroanal. Chem. 105 (1979) 35.
8. S. E. Creager and T. T. Wooster, Anal. Chem. 70 (1998) 4257.
9. A. P. Brown and F. C. Anson, J. Electroanal. Chem. 92 (1978) 133.
10. R. W. Murray, in: A. J. Bard & I. Rubinstein (Eds.), Electroanalytical Chemistry, Marcell Dekker, vol. 13, New York, 1984, p. 192.
11. R. A. Clark and E. F. Bowden, Langmuir, 13 (1997) 559.
12. M. S. Ravenscroft and H. O. Finklea, J. Phys. Chem. 98 (1994) 3843.
13. H. O. Finklea, L. Liu, M. S. Ravenscroft and S. Punturi, J. Phys. Chem. 100, (1996) 18858.
14. G. K. Rowe, M. T. Carter, J. N. Richardson and R. W. Murray, Langmuir, 11 (1995) 1797.
15. T. M. Nahir and E. F. Bowden, J. Electroanal. Chem. 410 (1996) 9.
16. R. Adzic, E. Yeager and B. D. Cahan, J. Electrochem. Soc. 121 (1974) 474.

17. W. Plieth, W. Kozlowski and T. Twomey, in: J. Lipkowski and P. N. Ross (Eds.), Adsorption of Molecules at Metal Electrodes, 1992, VCH Publishers, p. 239.

18. W. Plieth, P. Schmidt and P. Keller, Electrochimica Acta, 31 (1986) 1001.

19. P. H. Schmidt and W. J. Plieth, J. Electroanal. Chem. 201 (1986) 163.

20. Z. Q. Feng, T. Sagara and K. Niki, Anal. Chem. 67 (1995) 3564.

21. Z. Q. Feng, S. Imabayashi, T. Kakiuchi and K. Niki, J. Electroanal. Chem. 408 (1996) 15.

22. T. Ruzgas, L. Wong, A. K. Gaigalas and V. L. Vilker, Langmuir, 14 (1998) 7298.

23. A. K. Gaigalas and T. Ruzgas, J. Electroanal. Chem. 465 (1999) 96.

24. T. Sagara, T. Midorikawa, D. A. Shultz and Q. Zhao, Langmuir 14 (1998) 3682.

25. T. Sagara, S. Igarashi, H. Sato and K. Niki, Langmuir, **7** (1991) 1005.

26. S. Kim, Z. Wang, D. A. Scherson, J. Phys. Chem., 101 (1997) 2735.

Figure 3.1. Self-assembled monolayer with attached redox centers.

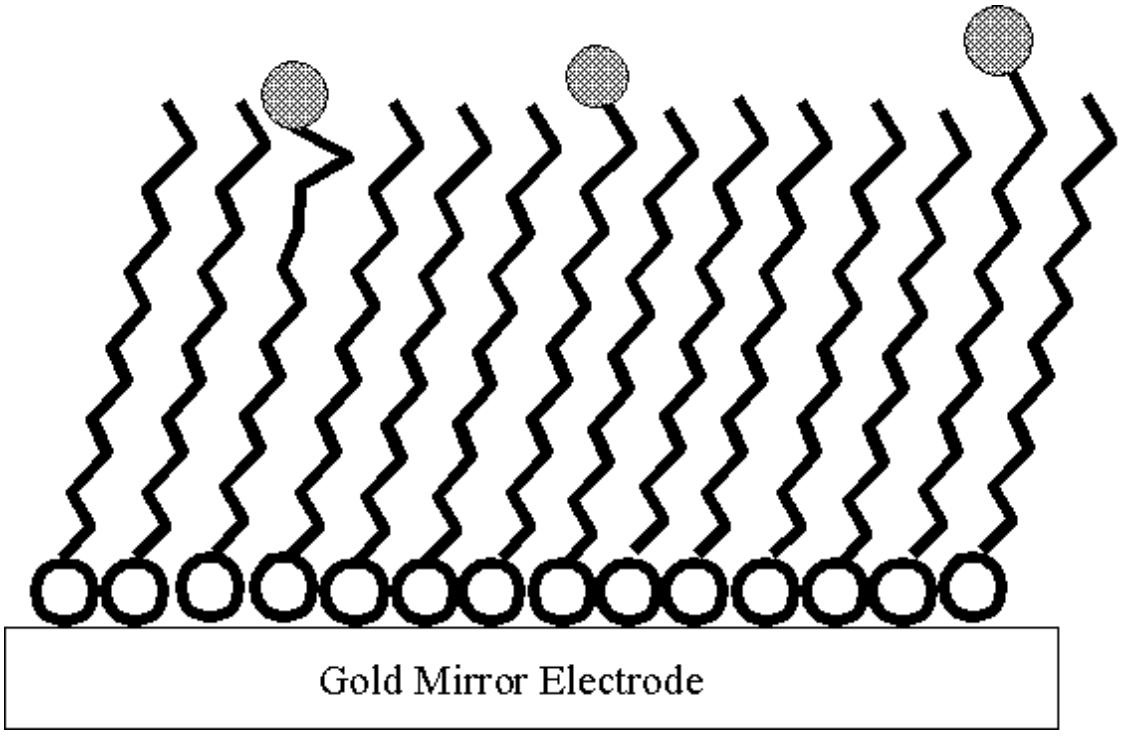

Figure 3.2. Experimental setup for simultaneous ACV and EMR ACV.

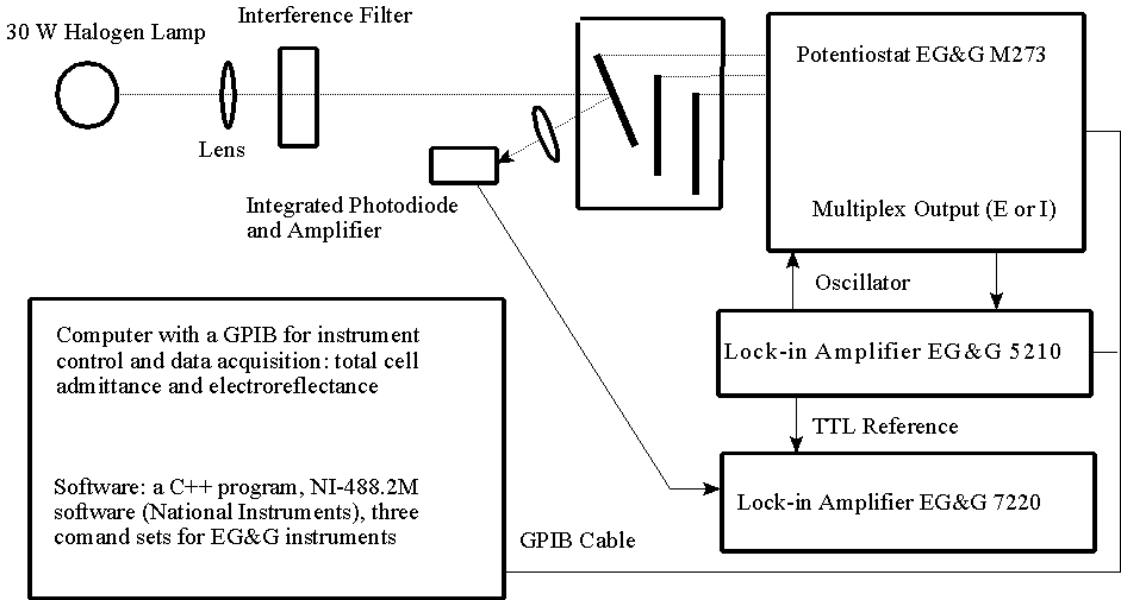

Figure 3.3 (a). ACV with 4 mV RMS at 231 Hz. Total cell admittance.

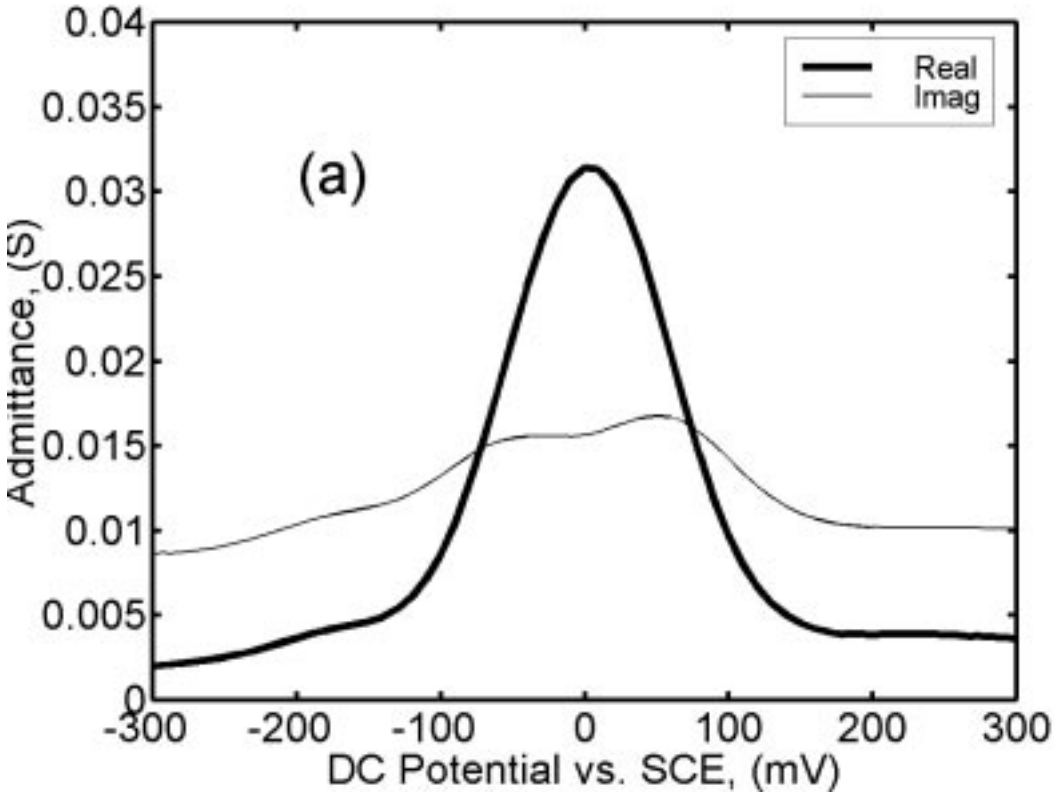

Figure 3.3 (b). ACV with 4 mV RMS at 231 Hz. Interfacial admittance corrected for R_u = 13.0 Ω.

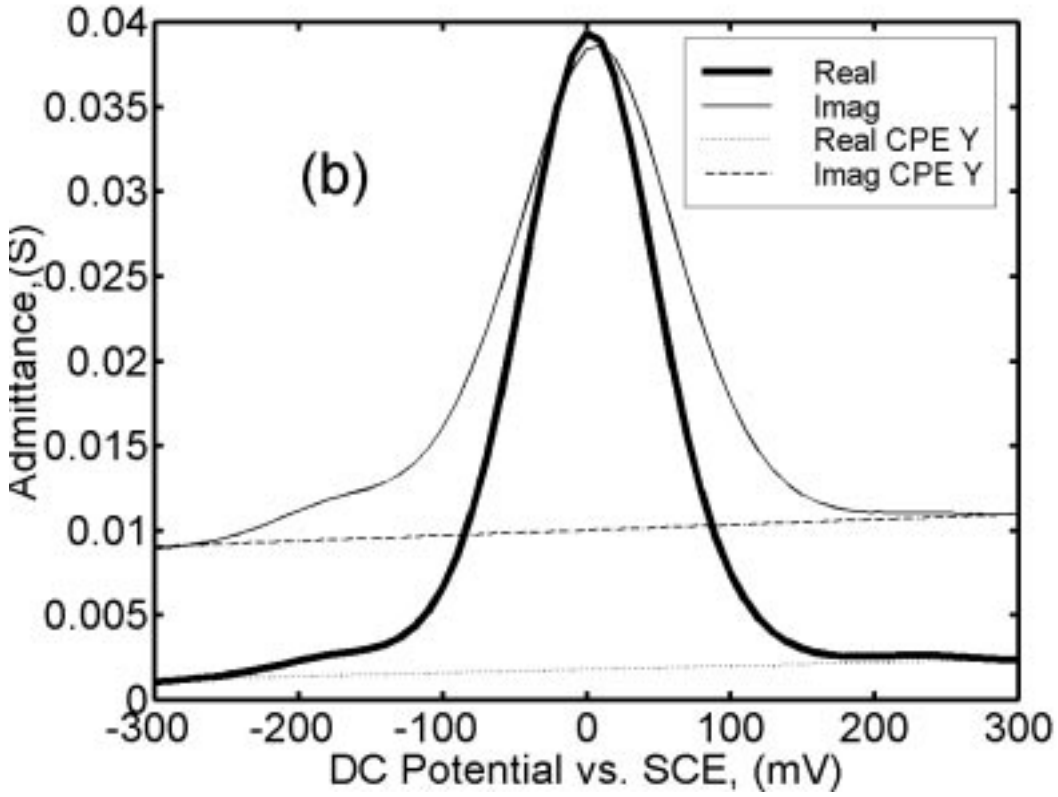

Figure 3.3 (c). ACV with 4 mV RMS at 231 Hz. Faradaic admittance. In contrast to 3.3 (a, b) experimental data are shown as points. Theoretical fits over a DC potential range used for optimization are shown as lines.

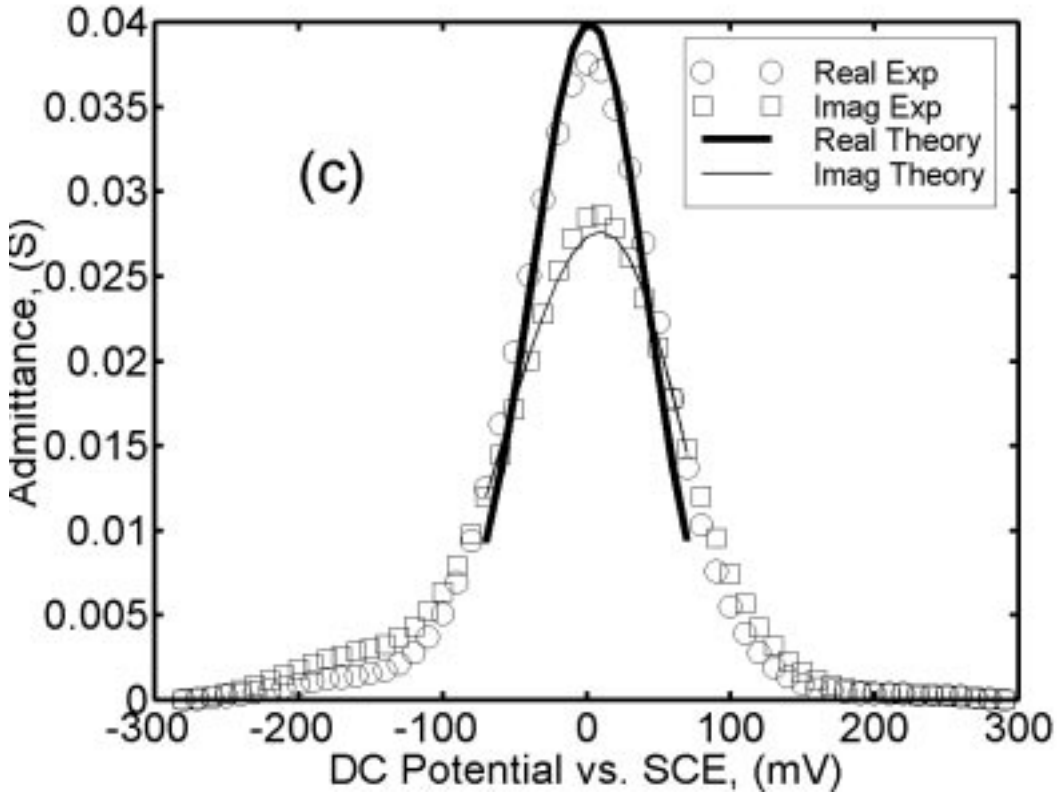

Figure 3.4. Cotangent of the faradaic admittance phase determined at $E^{0'}$ vs. ω.

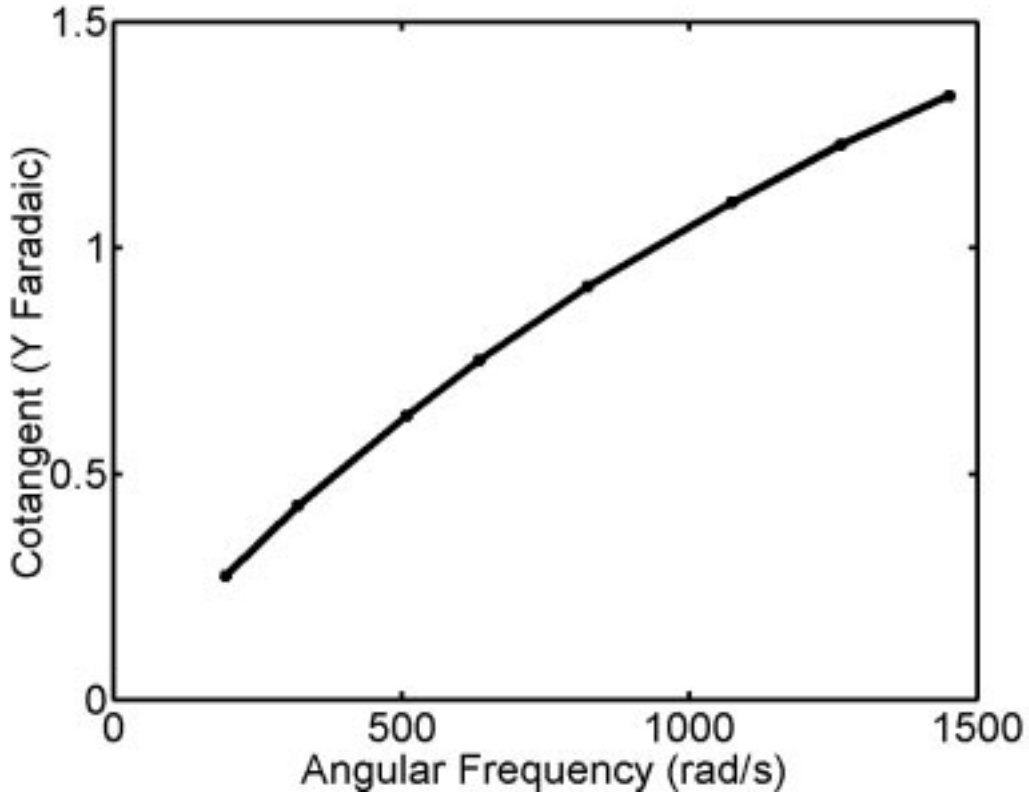

Figure 3.5. UV-VIS spectra of soluble reduced and oxidized forms of the Ru(4-AMP) complex.

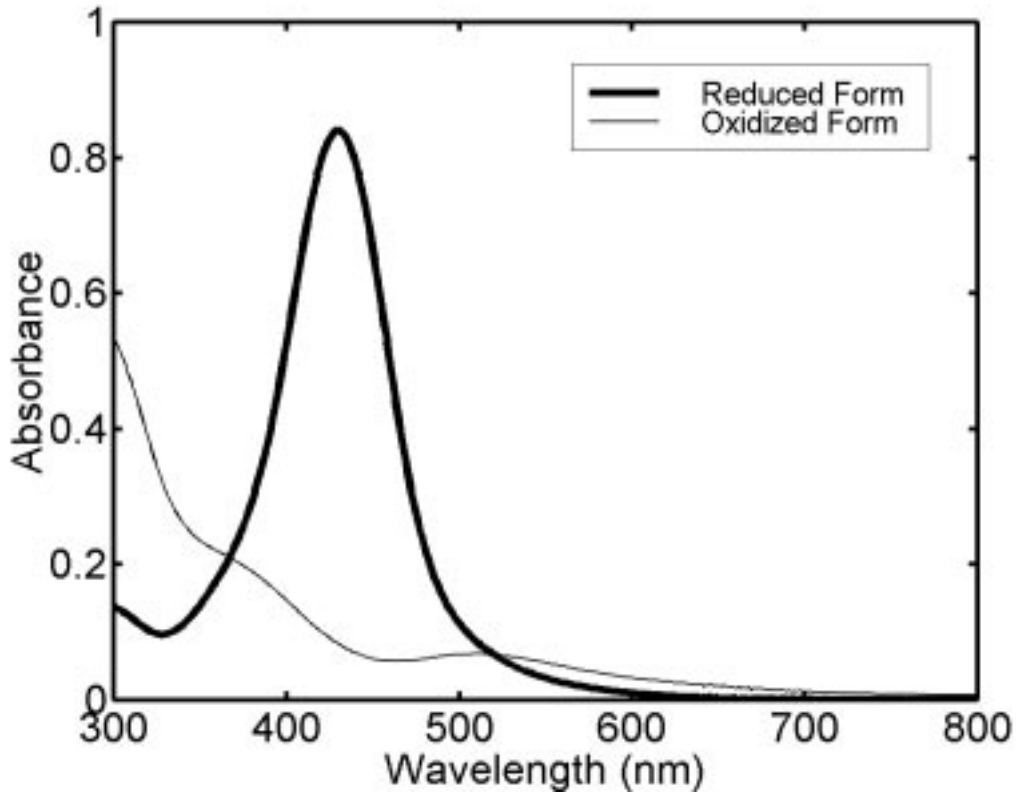

Figure 3.6 (a). EMR ACV at 440 nm and 81 Hz. Ratio of *ac* electroreflectance to DC electroreflectance, *dR*/*R*.

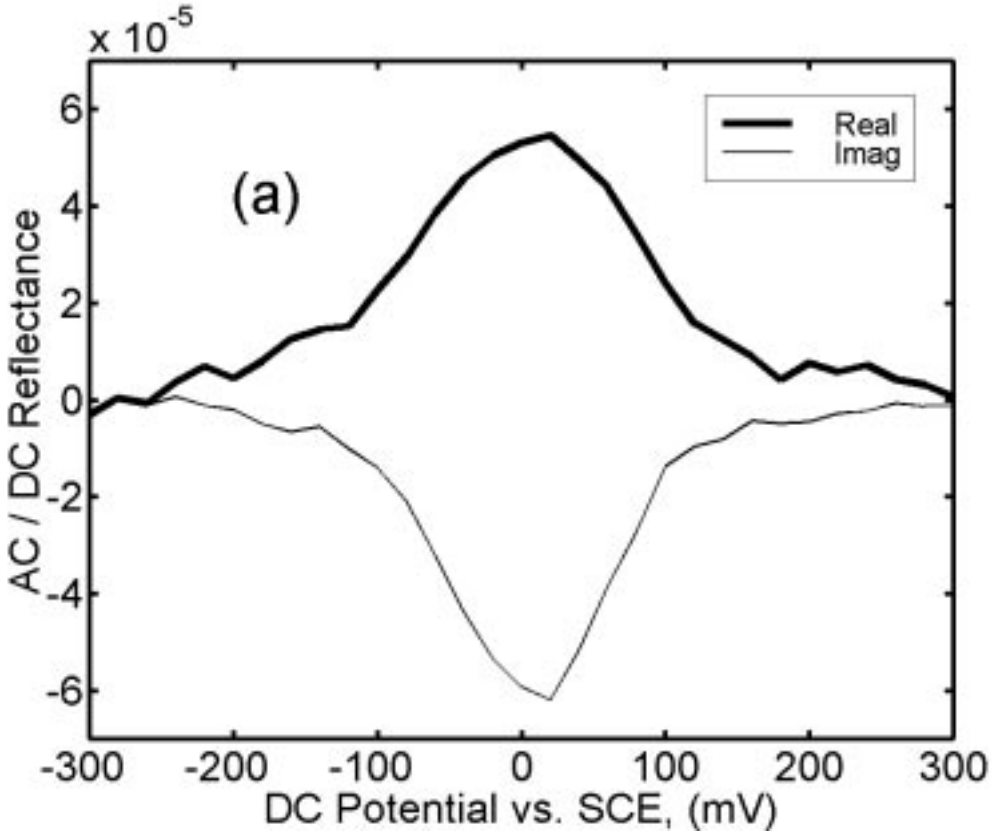

Figure 3.6 (b). EMR ACV at 440 nm and 81 Hz. Total cell and interfacial *ac* potential.

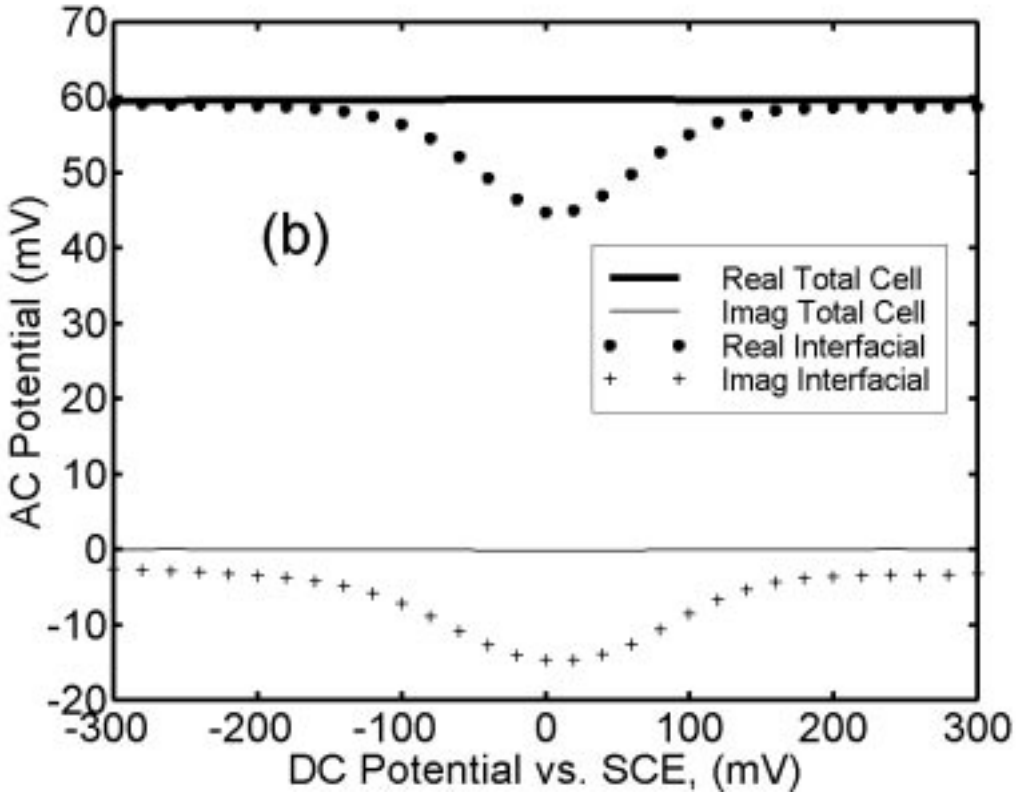

Figure 3.6 (c). EMR ACV at 440 nm and 81 Hz. Electromodulation reflectance coefficient, *X*.

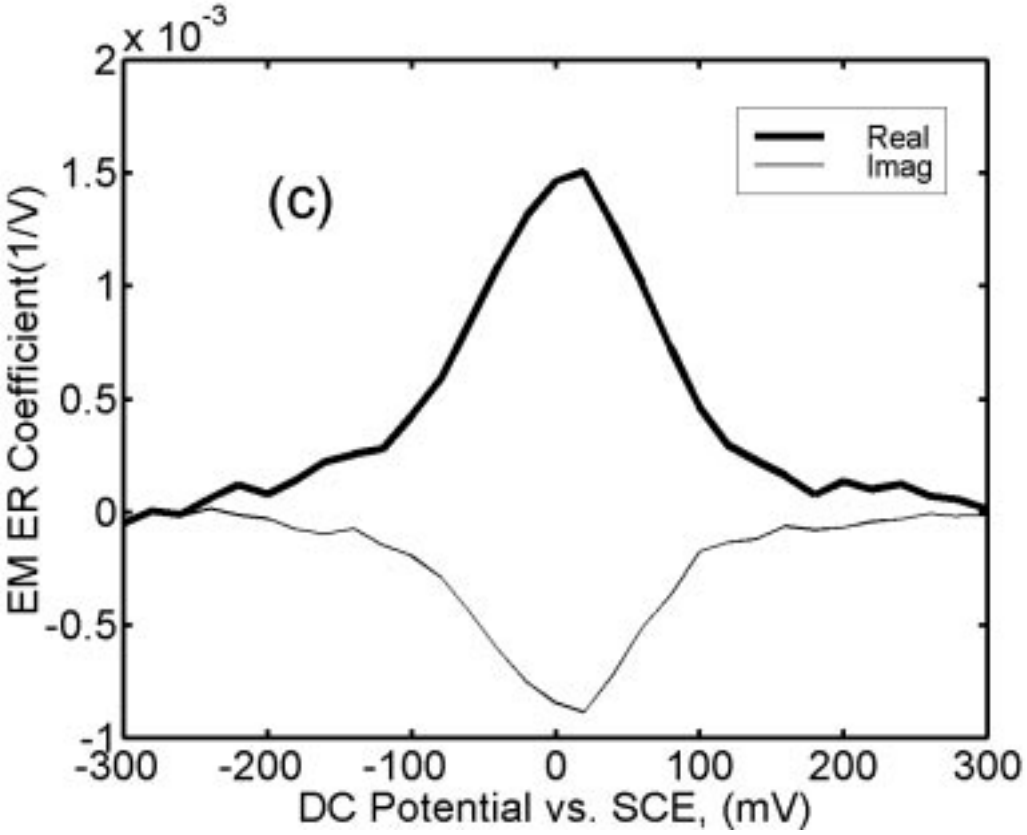

Figure 3.7 (a). ACV and EMR ACV measurements at 440 nm and 81 Hz with 40 and 60 mV *ac* potential perturbation, $Y^{faradaic}$.

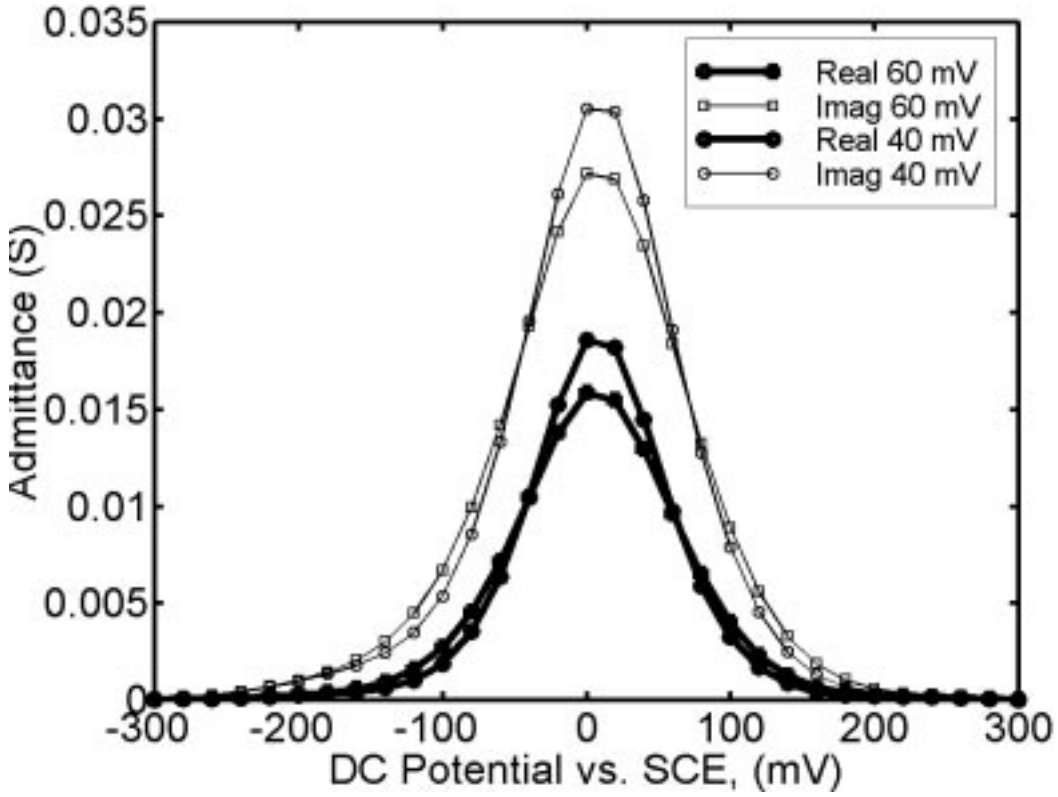

Figure 3.7 (b). ACV and EMR ACV measurements at 440 nm and 81 Hz with 40 and 60 mV *ac* potential perturbation. Ratio of *ac* electroreflectance to DC electroreflectance.

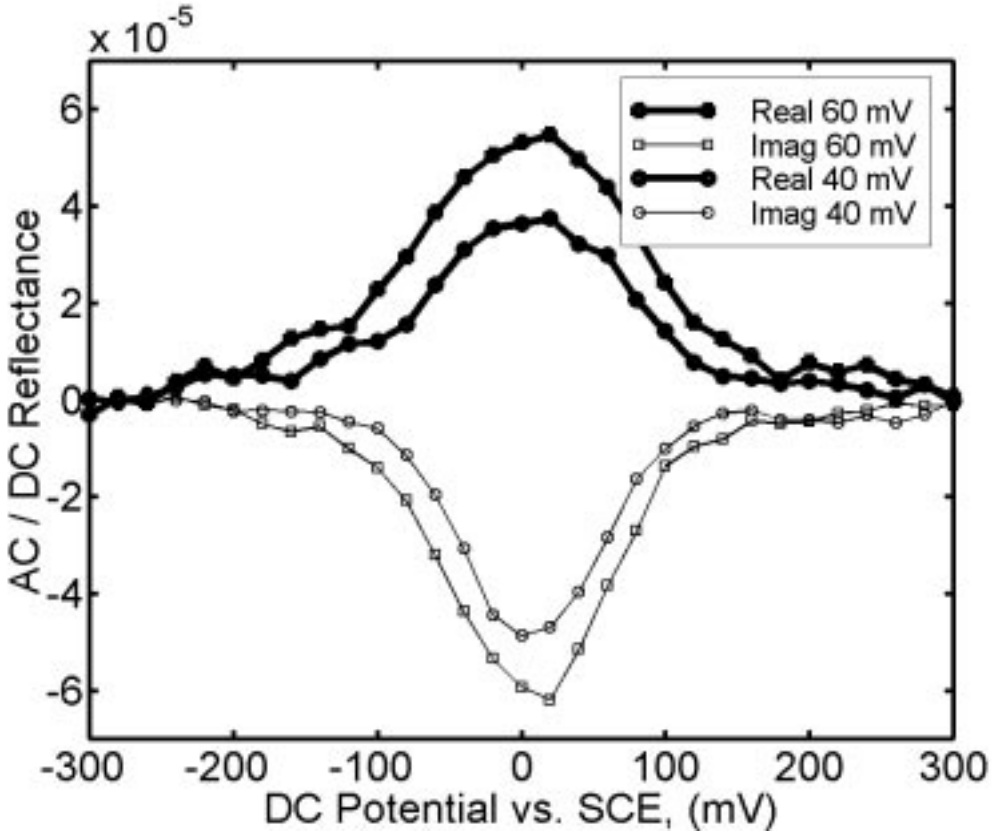

Figure 3.7 (c). ACV and EMR ACV measurements at 440 nm and 81 Hz with 40 and 60 mV *ac* potential perturbation, electromodulation reflectance coefficient, *X*.

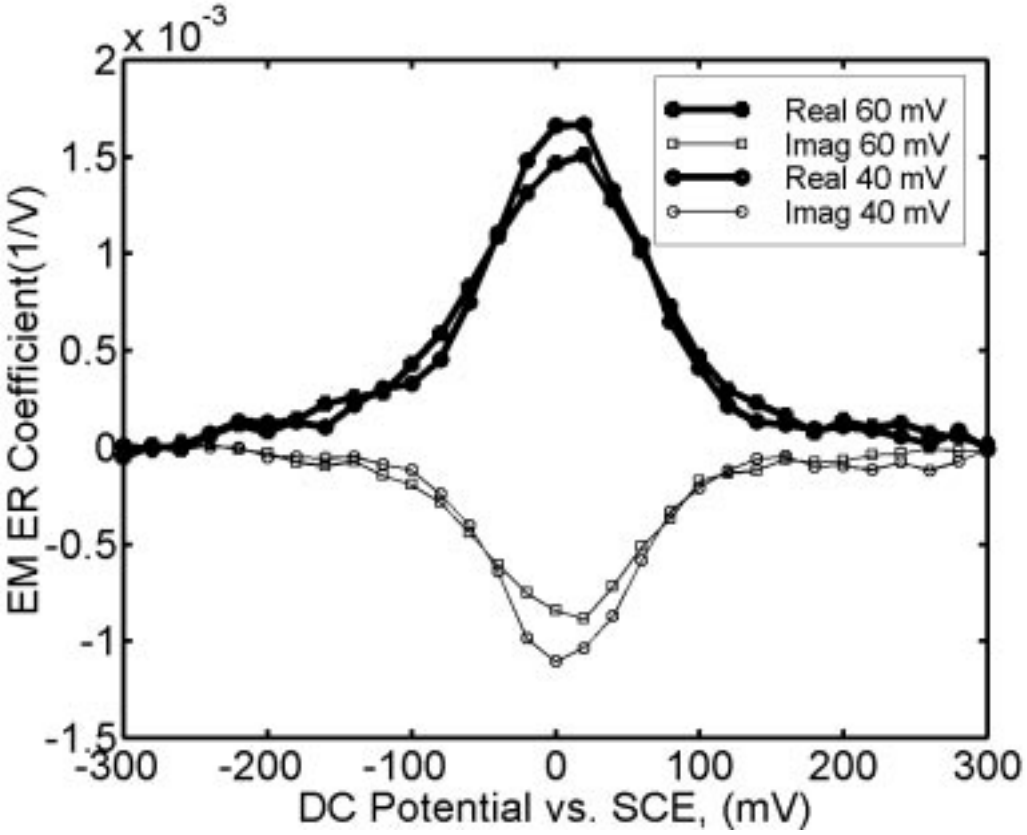

Figure 3.7 (d). ACV and EMR ACV measurements at 440 nm and 81 Hz with 40 and 60 mV *ac* potential perturbation, $X \times j\omega / Y^{faradaic}$.

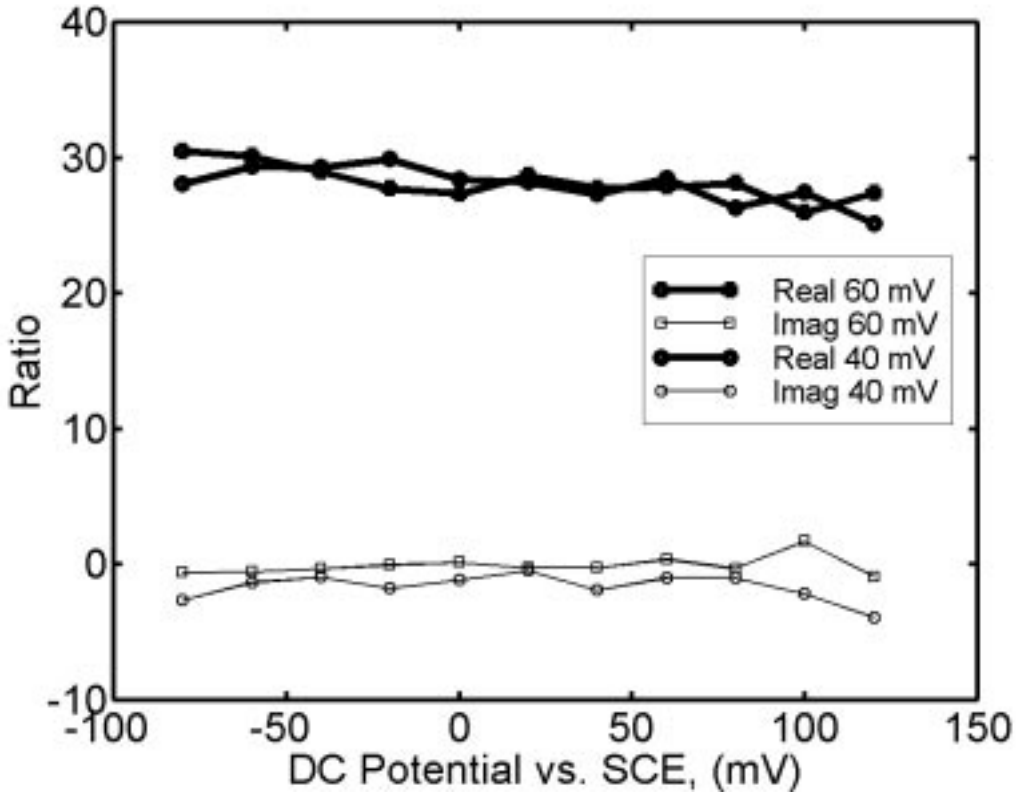

Figure 3.8. Phase of Electromodulation reflectance coefficient plus 90° at 440 nm and 81 Hz and phase of faradaic admittance at 81 Hz.

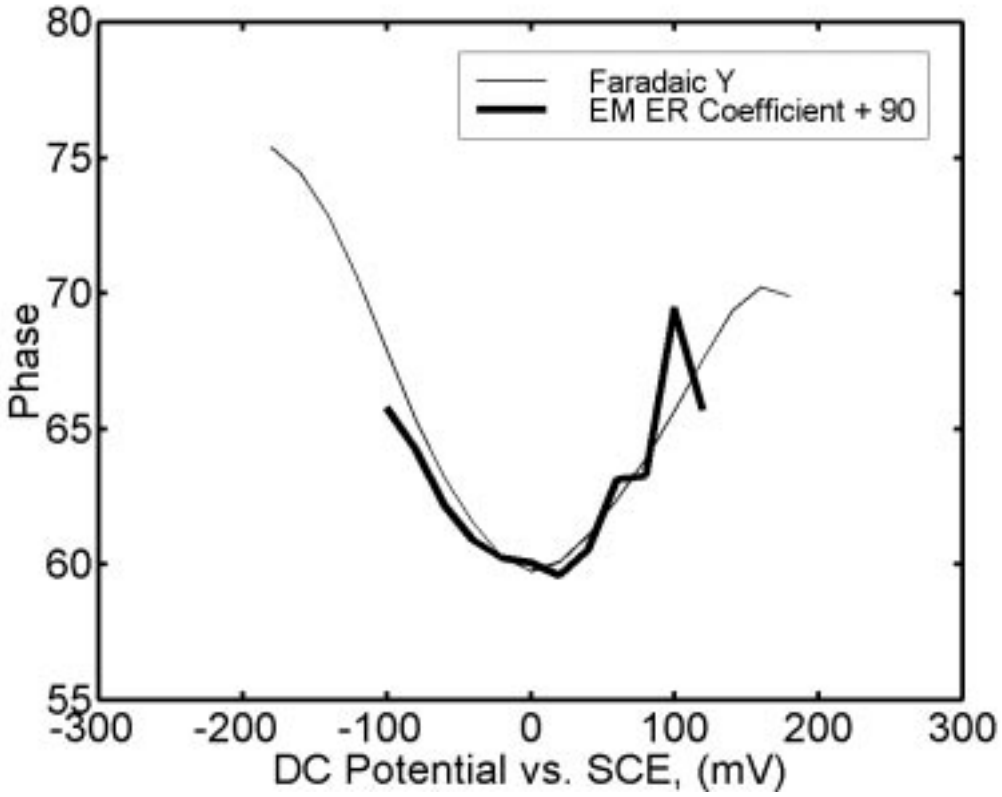

Figure 3.9. Electromodulation reflectance coefficient at 550 nm and 81 Hz.

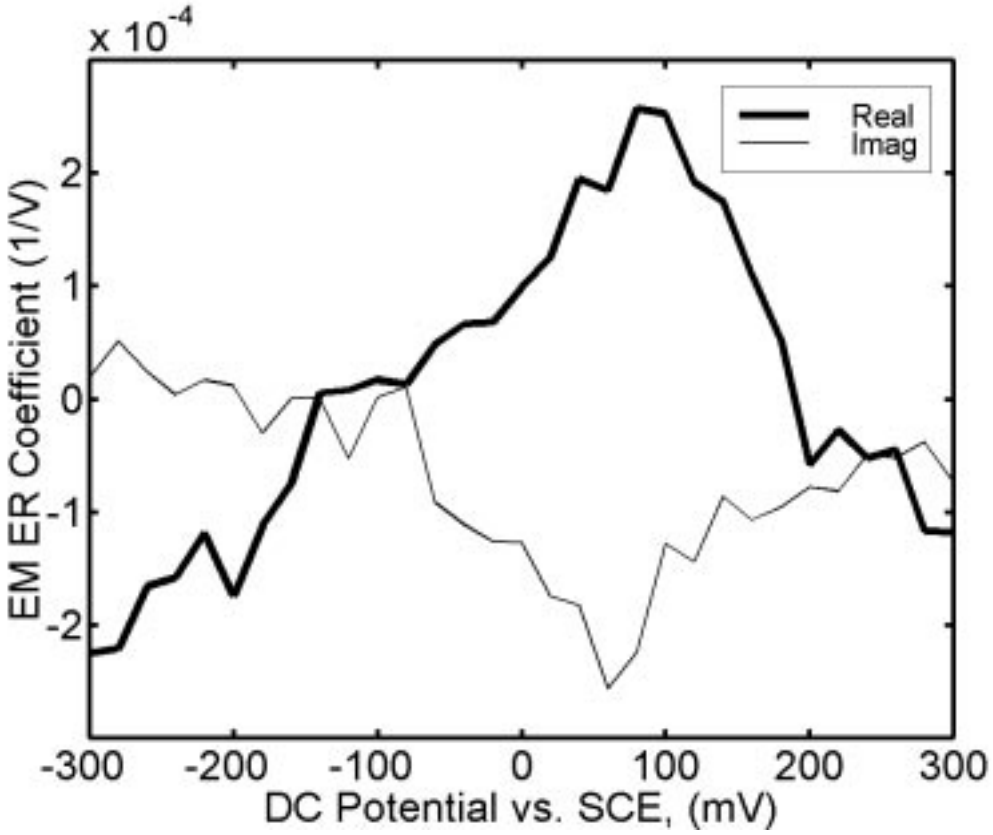

Chapter Four

AC Voltammetry studies of electron transfer kinetics for a redox couple attached via short alkanethiols to a gold electrode

1. Introduction

Kinetics of electron transfer between a metal electrode and redox centers attached to the electrode surface via alkanethiols has attracted considerable attention during the last decade.[1] Self-assembled monolayers (SAMs) are widely used structures for studying electrochemical kinetics because the distance between redox centers and a metal electrode can be precisely controlled by varying the chain length of alkanethiols. Measurement of the electron transfer kinetics in SAMs as a function of chain length[2-7], potential[2,8], and temperature[9,10] has provided elegant tests for the theory of heterogeneous electron transfer across the dielectric films.

Transient, time-domain electrochemical methods, fast scan Cyclic Voltammetry (CV) and Chronoamperometry (CA), have been widely used for kinetic studies in SAMs because of their simplicity and availability with standard electrochemical equipment. However, quantitative application of these methods is usually restricted to systems in which the standard rate constants (k_s) are significantly lower than the inverse of time constants associated with the non-faradaic elements.[11] Frequency-domain methods, such as Electrochemical Impedance Spectroscopy (EIS),[3,9] AC Voltammetry (ACV)[12] and

spectroelectrochemical Potential Modulated Electroreflectance (PM ER),[7,13] have been less frequently applied to SAMs in comparison with the time-domain methods. Frequency-domain methods are more suitable for determination of high k_s values because of their advantages: (a) correction for the limited bandwidth of potentiostat power amplifier, (b) facile correction for non-faradaic elements and, as a result, (c) more accurate separation and analysis of the faradaic signal. The frequency domain methods are better suited for kinetic measurements at low overpotentials, while CV and CA methods are necessary to obtain kinetic measurements at large overpotentials (potentials 100 mV away from the formal potential).

The theory for the faradaic admittance $Y^{faradaic}$ of a covalently bonded or strongly adsorbed electroactive species was developed by Laviron[14] in the limit of small *ac* potential perturbation and the absence of any intermolecular interactions (Langmuir isotherm). The faradaic impedance $Z^{faradaic}$ is represented as a series combination of frequency-independent R_a and C_a, where R_a, the adsorption resistance, and C_a, the adsorption capacitance, are given by Eqs. 3.1-3.3 listed in Chapter Three. In order to extract the $Y^{faradaic}$ information, the total cell admittance has to be corrected for both the uncompensated resistance (R_u) and the double layer or Constant Phase Element (CPE) admittance. The CPE admittance is defined as $Q = Q_0(j\omega)^x$, where Q_0 is the CPE constant and x is less than unity.

Previous kinetic studies by electrochemical methods have been mainly limited to SAMs with long alkyl chains (C_{10} - C_{15}) that significantly attenuate the rate of electron transfer.[1-3, 5, 8-10] Therefore, measurements of k_s were performed over long time scales

(seconds or milliseconds) at which the effects of non-faradaic elements are minimal and accurate corrections for their presence are not crucial. The plot of $\ln(k_s)$ vs. $\boldsymbol{n}$ (the number of methylene units) was linear for long alkyl chains, with a slope of -1.0 to -1.2 per CH_2. The primary determinate of k_s was the chain length.[2,4,6]

The rate of electron transfer via short ($<C_{10}$) alkanethiols was measured by fast scan CV for ferrocene-containing SAMs adsorbed at microelectrodes.[6] Similar to the experiments with long chain SAMs, the slope of -1.1 per CH_2 was obtained.[6] In addition, k_s for short chain SAMs were determined by electrochemical methods combined with other methods. Examples include the laser-induced temperature jump method for covalently attached ferrocene[4] and PM ER ACV[7] for electrostatically attached cytochrome *c*. In the former case, $\ln(k_s)$ was found to be linear with respect to the chain length with a slope of -1.2 per CH_2.[4] In contrast, the plot of $\ln(k_s)$ vs. $\boldsymbol{n}$ for cytochrome *c* on SAMs of $HS(CH_2)_nCOOH$ became independent of chain length for $\boldsymbol{n} < 8$. This result was modeled as a CE mechanism, with the preceding chemical step being rate-determining for short chain lengths.[7]

The experimental faradaic data for attached redox couples often deviate from the theoretical predictions.[1,9,15] For example, in CV and ACV plots under reversible conditions, the current peak is smaller and the peak half-width is larger than predicted.[3,15] These observations can be explained by thermodynamic heterogeneity (formal potential distribution).[15,16] Another possible explanation is lateral interactions because of either attraction or repulsion forces between adsorbed molecules (equivalent to an adsorption process which obeys a Frumkin isotherm).[17] A third possible explanation is double-layer

effects, in which the changing charge of the redox centers modulates the local electrostatic potential at the plane of the redox centers.[18,19] Double layer effects are anticipated to become more prominent for shorter chain length SAMs.

Similarly, faradaic signals from kinetically controlled currents often deviate from theory. For example, semi-log plots of current vs. time for a simple potential step are often curved rather than linear.[9,15] These deviations are attributed to kinetic heterogeneity, (e.g., a spread of k_s values about an average value). The causes of kinetic heterogeneity are still a matter of speculation. Protocols of data analysis have been developed to track the kinetic behavior of a specific population of kinetically uniform redox centers within the total population.[9,15] However, a method has not yet been applied to map the presumably continuous distribution of k_s values in electrochemically active SAMs for a given perturbation. The solutions for the inverse problem in electrochemistry (to determine a distribution from impedance data) can be found in the literature. Macdonald reported a software program that allows one to estimate a distribution of relaxation times.[20] Lasia applied a software package for the Matlab environment to determine distribution functions of electrochemical processes by means of regularization methods.[21]

2. Objectives of this research project

The objective of this research project is to examine the kinetics of electron transfer for the redox center [(4-aminomethylpyridine)$Ru(NH_3)_5]^{2+}$ (subsequently abbreviated as (Ru(4AMP)) attached to a gold electrode via short alkanethiols (C_{10}, C_7, C_5). ACV is chosen as a method most suitable for fast k_s measurements because of its capability of separating faradaic from non-faradaic signals even at high frequencies and, thus, looking at the processes at shorter time scales than time domain methods. Another objective of this research project is to differentiate among different possible origins of non-ideal voltammetric shapes observed for electrochemically active SAMs.

3. Experimental Part

Preparation of short chain alkanethiols and Ru(4AMP). Short alkanethiols $HS(CH_2)_nCOOH$ (***n***=5,7) were obtained from Prof. Ryswyk (Harvey Mudd College, Claremont, CA) and used as received. Ru(4AMP) and $HS(CH_2)_{10}COOH$ was available from previous research performed in Prof. Finklea's laboratory.[22]

Au bead electrode preparation, self-assembled monolayer (SAM) deposition and Ru(4AMP) attachment. The electrode cleaning procedure was analogous to that used in the previous project (Chapter Three). The only difference was a higher current density of 100 mA/cm^2 used to oxidize a gold bead electrode.

Electrochemical cell. ACV experiments were performed in 0.5 M NaF (a

nonadsorbing electrolyte) with pH adjusted to 5.0 with CF_3COOH. The solution was initially sparged with argon to remove dissolved oxygen and kept under a slow flow of argon during the experiment. Experiments were performed in a three-compartment electrochemical cell with a high surface area platinum mesh counter electrode and a SCE reference electrode. To minimize R_u for high-frequency measurements, a quasi-reference platinum wire electrode was connected in parallel with the SCE via a 1μF capacitor and positioned close to the gold bead electrode. The estimated area of gold bead electrode immersed in the solution was 0.1 cm^2.

Experimental setup for ACV experiments. The ACV experiments were performed using an EG&G Model 273 potentiostat and an EG&G Model 5210 Lock-in Amplifier (LIA). Both instruments were controlled via a GPIB interface using a C++ program. The program incorporated device-level functions (NI-488.2M National Instruments Corporation software for instrument control) and sets of commands specific for each of the instruments. The program performed the setting of all operating parameters for both instruments according to data in an input file. The collected data were recorded in an output file for further processing.

The potentiostat generated the applied DC potential. The 5210 LIA generated the *ac* potential applied to the *ac* interface input on the rear panel of EG&G 273. The EG&G 273 *ac* multiplex output was switched sequentially between *ac* current, $I^{totalcell}$, and *ac* potential, $E^{totalcell}$, and the corresponding signal measured by the LIA. A typical cell *ac* potential amplitude was 4 mV RMS. The time constant on the 5210 LIA was 30 ms. After each DC potential step, measurements were delayed until signals settled down over

a time period equal to 7 time constants. Ten samples were collected and averaged to get a single data point in ACV. The ACV measurements were repeated over the selected DC potential range with a DC potential step of 10 mV.

The uncompensated resistance R_u was measured using the same equipment running M398 Electrochemical Impedance Spectroscopy software. The real part of the total impedance was measured between 10 kHz and 80 kHz at a DC potential away from the faradaic wave. Extrapolation of the data on a complex-plane impedance plot to the real axis intercept yielded a value for R_u with an estimated uncertainty of ±0.5 Ω. The uncertainty in R_u was determined by R_u measurements before and after ACV experiments.

Data processing, representation and comparison of experimental Faradaic admittance with theory. ACV data are demonstrated in three formats, the total cell admittance $Y^{totalcell}$, interfacial admittance Y^{inter} and faradaic admittance $Y^{faradaic}$, as previously reported at the experimental section of Chapter Three. Y^{inter} was calculated according to Eq. 3.10. Experimental $Y^{faradaic}$ data were compared with theoretical curves calculated according to Eqs. 3.1-3.5. The minimized optimization function was the sum of squared differences between the experimental (both the real and the imaginary parts of $Y^{faradaic}$) and theoretical data at the same DC potentials. The DC potential range for optimization was limited to $E^{0'}$ ± 0.05 V (the top half of the faradaic wave). The optimization parameters were the formal potential ($E^{0'}$, V), the total electrode coverage ($\theta_{total} = \Gamma_{total} \times A$, mol), the standard rate constant k_s (s^{-1}) and the transfer coefficient (α).[23]

4. Results

The EDC-catalyzed coupling reaction affords an easy and flexible route to an electroactive monolayer without requiring the co-adsorption of two disparate thiols. The structure of the SAM suffers minimal perturbation, because the capacitance of the electrode/electrolyte interface does not perceptively change after the coupling reaction. The coverage of the redox center can be controlled through the time and temperature of the coupling reaction. In this work, the time was adjusted to achieve a coverage of redox centers comprising 30-50% of the maximum coverage ($3\text{-}5\times10^{-11}$ mol/cm^2 as determined by slow scan CV).

Table 4.1. Interfacial dielectric properties for one C_{10}, one C_7 and one C_5 SAMs. Q_0 and x are the two parameters of CPE.

Chain Length	$Q_0\times10^7$	x
10	3.1	0.95
7	5.3	0.99
5	7.8	0.99

Table 4.1 contains the interfacial dielectric properties determined for three chain lengths over frequency range of 100 Hz - 1 kHz at 400 mV vs. SCE, which is 350 mV positive of the formal potential. Because the CPE is a more accurate model for the dielectric interface (especially at low frequencies) than a pure capacitor, the total cell impedance data at this potential were modeled as a series combination of R_u and CPE with R_u being fixed to a value determined at high frequencies. It would be more

appropriate to compare, the CPE magnitude, Q_0, normalized to the electrode area. However, the electrode areas were not precisely controlled from one experiment to another. Table 4.1 shows that as the chain length decreases, Q_0 increases and the CPE exponent x remains close to 1 (nearly ideal capacitance). The trend of Q_0 vs. chain length is consistent with other measurements of SAM capacitance with chain length.[24] Both Q_0 and x are reported with two significant figures, with the relative error (as reported by the Equivalent Circuit optimization program) being less than 4%. The measurements for two SAMs demonstrate that Q_0 varies around 5%.

Figure 4.1 illustrates $Y^{totalcell}$, Y^{inter} and $Y^{faradaic}$ collected with a 2200 Hz perturbation frequency for a C_7 SAM. At this high frequency, distortion of $Y^{faradaic}$ peak is noticeable in Figure 4.1(a). After correction for an R_u of 18.8 Ω (Figure 4.1(b)) and the CPE baseline (Figure 4.1(c)), $Y^{faradaic}$ exhibits the expected shape. Figure 4.1(c) shows that the experimental data and theoretical $Y^{faradaic}$ curves from Eqs. 3.1-3.3 (Chapter Three) have slight but noticeable differences. Both the real and imaginary peaks of the experimental $Y^{faradaic}$ are slightly smaller and wider than corresponding theoretical peaks for a simple 1-electron surface redox process.

Two of the four optimization parameters: (k_s, θ_{total}) determined over more than one decade of frequency are summarized in Tables 4.2 and 4.3 for one C_{10} and one C_7 SAM, respectively. Both the formal potential, $E^{0'}$, (+0.020 V vs. SCE) and transfer coefficient, α, (0.5±0.1) are found to be nearly constant for all frequencies and are not shown in Tables 4.2 and 4.3. Although there is some deviation between the experimental and theoretical $Y^{faradaic}$ peaks and, thus, some uncertainty in the values reported in Tables 4.2

and 4.3, it is clear that the total coverage of redox centers (θ_{total}) appears to decrease and the standard rate constant (k_s) appears to increase as the perturbation frequency increases. This phenomenon could be a manifestation of thermodynamic heterogeneity and/or kinetic heterogeneity. Therefore, it is helpful to look at a reversible AC voltammogram to distinguish the two possibilities.

Table 4.2. Optimization parameters for $Y^{faradaic}$ determined for each perturbation frequency for one C_{10} SAM.

frequency /Hz	k_s/ $10^{-2}\times s^{-1}$	$\theta_{total} = A\times\Gamma_{total}\times10^{12}$/ mole
16	2.0	3.6
25	2.2	3.3
33	2.4	3.1
42	2.7	2.9
75	3.0	2.8
100	3.3	2.6
250	4.2	2.3
350	4.6	2.1
450	4.9	2.0

Figure 4.2 exhibits the $Y^{faradaic}$ peak near 0 V vs. SCE determined at 81 Hz for a C_5 SAM. The faradaic wave at about 250 mV vs. SCE is attributed to an impurity present in Ru(4AMP) (probably the bis(pyridine) complex) formed during synthesis. This impurity is believed not to interfere with the main faradaic wave near 0 mV. Because the C_5 SAM exhibits very fast kinetics, the response of this system is essentially reversible at 81 Hz; the $Y^{faradaic}$ phase near $E^{0'}$ is close to 90°.

Table 4.3. Optimization parameters for $Y^{faradaic}$ determined for each perturbation frequency for one C_7 SAM.

frequency /Hz	k_s/ $10^{-4}\times s^{-1}$	$\theta_{total} = A\times\Gamma_{total}\times10^{12}$/ mole
431	0.88	4.7
831	0.98	4.6
1231	1.02	4.4
1831	1.06	4.3
2200	1.10	4.2
3200	1.19	4.0
4200	1.28	3.8
5200	1.36	3.6
6200	1.45	3.5

For this kinetically reversible case, the fit between the experimental $Y^{faradaic}$ and theoretical Y^{model} data over a DC potential range of $E^{0'}$ ± 50 mV demonstrates approximately the same relative error as that in Figure 4.1 (c). The relative errors as defined by Eq. 4.1 are equal to 0.16 and 0.17 in Figures 4.2 and 4.1(c), respectively.

$$\text{Relative Error} = 1/N \times [\sum(\text{abs}(\text{Real}(Y^{faradaic}) - \text{Real}(Y^{model})))/ \text{Real}(Y^{faradaic}) + \sum(\text{abs}(\text{Imag}(Y^{faradaic}) - \text{Imag}(Y^{model})))/ \text{Imag}(Y^{faradaic})] \quad (4.1)$$

where N is a number of points used for optimization.

The same two optimization parameters, k_s and θ_{total} are summarized for a C_5 SAM in Table 4.4. ACV experiments were restricted to frequencies up to 20 kHz. At frequencies between 20 kHz and 50 kHz, the imaginary part of Y^{inter} becomes significantly

depressed around $E^{0'}$. At frequencies higher than 50 kHz, the imaginary part of Y^{inter} becomes negative which is formally indicative of some inductance. This behavior is inconsistent with the parallel combination of CPE and $Z^{faradaic}$ (a serial combination of R_a and C_a). At frequencies higher than 20 kHz, the impedance data are believed to be distorted by the limited bandwidth of the current follower, even when the potentiostat current sensitivity is set to 100 mA/V. Lower frequencies were not analyzed because the system approaches reversible behavior.

Table 4.4. Optimization parameters for $Y^{faradaic}$ determined for each perturbation frequency for one C_5 SAM.

frequency /Hz	k_s/ $10^{-5}\times$ s^{-1}	$\theta_{total} = A\times\Gamma_{total}\times10^{12}$/ mole
3000	0.66	5.0
5000	0.85	4.5
8000	1.1	4.1
10000	1.2	3.9
20000	1.3	3.7

In addition to being frequency dependent (similar to the C_{10} and C_7 SAMs), the experimental values of k_s for C_5 are very sensitive to the value of R_u used in the data analysis. For example, at 10 kHz, k_s is calculated to be 1.2×10^5 s^{-1} when an R_u of 16.0 Ω is substituted into Eq. 3.10 (Chapter Three). Data analysis with an R_u of 16.5 Ω and 15.5 Ω results in k_s values of 3.3×10^5 s^{-1} and 7.5×10^4 s^{-1}, respectively. Consequently, a small error in R_u results in a substantial uncertainty in k_s reported in Table 4.4. The same error in R_u results in a negligible uncertainty in k_s for C_{10} and a small uncertainty in k_s for C_7 as

reported in Table 4.5. In Table 4.5 k_s for C_{10} and C_7 SAMs are reported with three significant figures in order to demonstrate the effect of uncertainty in R_u.

Table 4.5. Summary of k_s determined at a frequency at which the $Y^{faradaic}$ phase is closest to 70° for two C_{10}, four C_7 and two C_5 SAMs.

Chain Length	frequency / Hz	k_s/sec^{-1}	R_u /Ω	k_s/sec^{-1} with R_u + 0.5 Ω	k_s/sec^{-1} with R_u - 0.5 Ω
10	33	244	31.5	244	244
10	33	233	30.5	233	233
7	1231	10600	23.5	11500	9800
7	1231	12500	26.5	13100	11400
7	1231	9000	19.5	9400	8700
7	1231	10200	18.8	10600	9600
5	12000	1.7×10^5	20.5	6.0×10^5	1.0×10^4
5	10000	1.2×10^5	16.0	3.3×10^5	7.5×10^4

The $Y^{faradaic}$ data can also be analyzed at a single DC potential as a function of the radial frequency, ω. The cotangent of the $Y^{faradaic}$ phase at $E^{0'}$ vs. ω is plotted, in Figures 4.3-4.4 for the C_7 and C_5 SAMs, respectively. The analogous plot for a C_{10} SAM is shown in Figure 3.4 (Chapter Three). According to Eq. 4.2 (the same as Eq. 3.12 reported in Chapter Three), this plot should be linear with a slope reciprocally related to k_s.

$$Cot\,(\varphi) = Cot\,(Y^{faradaic}\,(E^{0'})) = \omega / (2k_s) \qquad (4.2)$$

The curvature is indicative of increasing apparent k_s with increasing frequency. Limiting slopes of this plot for the lowest and highest frequencies yield k_s values of 1.0×10^4 s^{-1} and 2.5×10^4 s^{-1}, respectively. These values are slightly higher than those reported in Table 4.3 because the fit of $Cot(Y^{faradaic}(E^{0'}))$ at one DC potential $E^{0'}$ does not take in account the faradaic wave non-ideality over a wider DC potential range.

Finally, it is worthwhile to note that all three systems under investigation possess temporal stability only for a period of an hour, which is long enough to perform about 9 ACV experiments at different frequencies. If ACV experiments with the same perturbation frequency are repeated over a three hour period, the total coverage of redox centers decreases by about 15% and the standard rate constant increases by about 5%. All results reported in Tables 4.2-4.4 were collected with individual SAMs. Results with other SAMs demonstrated similar kinetic data (Table 4.5) and the same frequency dependance of k_s and θ_{total}.

5. Discussion

The SAMs described here are designed to minimize the deviations from ideal behavior in order to validate the kinetic measurements. The surface coverage of the redox centers is held in a range that yields faradaic current comparable to the non-faradaic current under most experimental conditions while avoiding crowding of the redox centers along the surface of the monolayer (coverages in the range of $3\text{-}5\times10^{-11}$ mol/cm^2). The electrolyte ions are highly hydrophilic and should have the least tendency to penetrate the

hydrocarbon domain of the SAM and to form ion-pairs with the redox centers. The electrolyte concentration is high to minimize both double layer effects and the uncompensated resistance.

In addition to the chemical manipulations, valid kinetic measurements of the fast electron transfer are possible because of the ACV instrumental and data processing advantages. The procedure used here to correct for both R_u and the CPE baseline allows one to determine the rate of fast faradaic processes that occur on a time scale comparable with the time constant associated with non-faradaic elements. For example, in the C_5 SAM, $1/k_s$ is about 60 μs while the cell time constant is about 20 μs. In addition, corrections for both R_u and the CPE do not require any explicit assumptions about the equivalent circuit for $Y^{faradaic}$. Another advantage of the data processing method used here is that the $Y^{faradaic}$ phase can be used to detect the presence of kinetic heterogeneity (Figure 4.3). The $Y^{faradaic}$ phase is less sensitive to the SAM temporal instability, since the $Y^{faradaic}$ phase depends only on k_s, but not θ_{total}. Therefore, the procedure to separate $Y^{faradaic}$ from the total cell response has a wider applicability than the procedure suggested by Creager.[12] Creager's method ignores the $Y^{faradaic}$ phase and is applicable in situations at which the effect of the cell time constant is negligible.[12]

There are slight but persistent discrepancies between the theory for simple 1-electron transfer and the experimental $Y^{faradaic}$ peaks. Since ACV experiments were performed with low surface concentrations, lateral interactions among redox centers are unlikely to be a reason for the observed discrepancy. In addition, linear plots of $Cot(\theta)$ vs. ω (Figure 4.3) are expected for not only the Langmuir isotherm but also the Frumkin

isotherm.[17] Thus, it is unlikely that lateral interactions between redox centers (according to the Frumkin isotherm) cause the observed curvature in the plot. The almost ideal fit of $Y^{faradaic}$ to theory (Figure 4.1(c) and 4.2) under both reversible and quasi-reversible conditions supports the hypothesis that the redox centers are nearly thermodynamically homogeneous. The same experiments also provide evidence that the double layer effects, which would cause peak broadening,[18,19] are negligible in 0.5 M NaF, even for the short C_5 SAM.

It is likely that a distribution of the standard rate constants is the source of both the slight discrepancy between the experimental and theoretical $Y^{faradaic}$ determined at a single ω and the nonlinear plot of $Cot(\theta)$ vs. ω, as demonstrated, for example, for a C_7 SAM (Figure 4.3). A distribution of k_s may arise from several causes. Variations in chain structure or contact of the redox centers with adjacent diluent thiols could affect the electronic coupling between the redox centers and the electrode. Similarly, differences in solvation around the redox centers, with some redox molecules partially buried in the SAM and others fully solvated by water, would result in a distribution of reorganization energies (λ). A distribution of reorganization energies will result in a distribution of k_s, even in ACV experiments performed at low overpotential, because k_s is proportional to $\exp(-\lambda/(4RT))$.[25]

No attempt was made here to extract a distribution of k_s from the faradaic impedance data. $Z^{faradaic}$ at $E^{0'}$ can be fitted to a model containing a series combination of an ideal capacitance, C_a, and a CPE with x being slightly above zero.[3] The physical reasoning for this model is that a distributed element, k_s, appears only in the expression

for R_a in the Laviron model.[14] Unfortunately, these data are not diagnostic of a particular form of k_s distribution. Almost all suggested k_s distributions demonstrate a response in the frequency domain that is close to the fractional power-law over a finite-frequency range.[26]

Because of the observed kinetic heterogeneity, it is difficult to assign a single rate constant to a given chain length. For CA and CV experiments, a more kinetically uniform sub-population of the redox centers can be selected based on the percentage of the reactant remaining during the kinetically controlled current transient.[1,5] For ACV, the best method for comparing k_s for different chain lengths is to fix the $Y^{faradaic}$ phase. Eq. 4.2 shows that the $Y^{faradaic}$ phase defines the relationship between k_s and ω independent of the chain length. The choice of 70° $Y^{faradaic}$ phase suggested as a reference point is dictated by two facts. On one hand, the Imaginary part of $Y^{faradaic}$ is relatively insensitive to the value of k_s at higher phase angles. On the other hand, with the shortest chain length C_5, in order to achieve lower phase angles, high perturbation frequencies (>10 kHz) are necessary. At these high frequencies, the calculated $Y^{faradaic}$ data are very sensitive to the measured value of R_u. In addition, the bandwidth limitation of the potentiostat current follower becomes apparent.

Table 4.5 contains the perturbation frequency at which the $Y^{faradaic}$ phase is closest to 70°, k_s for all of the SAMs examined, and high and low values of k_s as a result of a ±0.5 Ω uncertainty in R_u. A semilog plot of the average values of k_s for each chain length vs. $\boldsymbol{n}$ (Figure 4.5) is found to be linear with a linear regression slope of -1.2±0.1 per CH_2. The high standard deviation in the linear regression analysis results from the uncertainty

associated with the value of k_s determined for the shortest chain length C_5. The uncertainties for all k_s measurements are included in Fig. 4.5 as high and low points at each chain length. If these data are combined with the standard rate constant of 1 s^{-1} for the C_{15} SAM,[2] the linear regression slope of the semilog plot is -1.2 ± 0.1 per CH_2. The same slope (-1.2) is obtained if k_s is determined at 45° $Y^{faradaic}$ phase. k_s is about 345 s^{-1} at 120 Hz, and 1.28×10^4 s^{-1} at 4200 Hz for a C_{10} and C_7 SAMs, respectively. There is no evidence that k_s is approaching an adiabatic limiting value postulated by other theory.[27] This theory claims that k_s becomes independent of distance at short distances. These results are in agreement with the results of Smalley et al., who found a slope of -1.2 per CH_2 for the short chain SAMs (C_5 - C_9) with pendant ferrocenes[4] and Weber at al., who measured a slope of -1.1 per CH_2 for (C_7 - C_{10}).[6]

6. Conclusions

Standard rate constants for simple electron transfer between gold bead electrodes and attached ruthenium complexes are determined as a function of the chain length for C_{10}, C_7 and C_5 SAMs. A procedure is used for correction of experimental ACV data and determination of $Y^{faradaic}$. This procedure allows one to investigate faradaic processes that occur on the time scale comparable the cell time constant. Kinetic heterogeneity is suggested to be a probable reason for non-ideal shapes of $Y^{faradaic}$ in ACV experiments and curvature in the plot of $Cot(\theta)$ vs. ω. Lateral interactions between redox centers and double layer effects appear to be negligible. The accurate determination of k_s for C_5 is

compromised by the uncertainty in the value of R_u. Like ferrocene and unlike cytochrome *c*, the ln(k_s) plot vs. ***n*** for Ru(4AMP) remains linear to short chain length (estimated to be about 10 Å for C_5). No sign of k_s becoming independent of distance (adiabatic electron transfer) is observed.

References

1. H. O. Finklea, in: A. J. Bard and I. Rubinstein (Eds.), Electroanalytical Chemistry, Marcel Dekker, vol. 19, New York, 1996, p.109.
2. H. O. Finklea, D. D. Hanshew, J. Am. Chem. Soc., 114 (1992) 3173.
3. S. Song, R. A. Clark, E. F. Bowden, M. J. Tarlov, J. Phys. Chem., 97 (1993) 6564.
4. J. F. Smalley, S. W. Feldberg, C. E. D. Chidsey, M. R. Linford, M. D. Newton, Y.-P. Liu, J. Phys. Chem., 99 (1995) 13141.
5. H. O. Finklea, L. Liu, M. Ravenscroft, S. Punturi, J. Phys. Chem., 100 (1996) 18852.
6. K. Weber, L. Hockett, S. Creager, J. Phys. Chem. B, 101 (1997) 8286.
7. Z. Q. Feng, S. Imabayashi, T. Kakiuchi, K. Niki, J. Chem. Soc., Faraday Trans., 93 (1997) 1367.
8. C. E. D. Chidsey, Science, 251 (1991) 919.
9. H. O. Finklea, M. S. Ravenscoft, D. A. Snider, Langmuir, 9 (1993) 223.
10. H. O. Finklea, M. S. Ravenscoft, Israel J. Chem. 37 (1997) 179.
11. E. Laviron, in: A. J. Bard (Ed.), Electroanalytical Chemistry, Marcel Dekker, vol. 12, New York, 1982, pp. 53-157.
12. S. E. Creager, T. Wooster, Anal. Chem. 70 (1998) 4257.
13. D. Brevnov, H. O. Finklea, submitted.
14. E. Laviron, J. Electroanal. Chem., 97 (1979) 135.
15. G. K. Rowe, M. T. Carter, J. N. Richardson, R. W. Murray, Langmuir, 11 (1995)

1797.

16. R. A. Clark, E. F. Bowden, Langmuir, 13 (1997) 559.

17. E. Laviron, J. Electroanal. Chem., 105 (1979) 25.

18. C. P. Smith, H. S. White, Anal. Chem. 64 (1992) 2398.

19. R. Andreu, J. J. Calvente, W. R. Fawcett, M. Molero, J. Phys. Chem. B, 101 (1997) 2884.

20. For a complete list of papers and a downloadable version of the program, see http://www.physics.unc.edu/~macd/

21. F. Dion, A. Lasia, J. Electroanal. Chem. 475 (1999) 28-37.

22. H. O. Finklea, D. D. Hanshew, J. Electroanal. Chem. 347 (1993) 327.

23. Because the fitted function only extended over the range of ±50 mV overpotential, α was considered to be potential independent.

24. M. D. Porter, T.B. Bright, D. Allara, C. E. D. Chidsey, J. Am. Chem. Soc., 109 (1987) 3559.

25. C. J. Miller, in: I. Rubinstein (Ed.), Physical Electrochemistry (Principles, methods, and applications), Marcel Dekker, New York, 1995, p. 27.

26. J. R. Macdonald, J. Appl. Phys., 62 (1987) R51.

27. J. T. Hupp, M. J. Weaver, J. Phys. Chem., 88 (1984) 1463.

Figure 4.1 (a). Total cell admittance for a C_7 SAM at f = 2200 Hz.

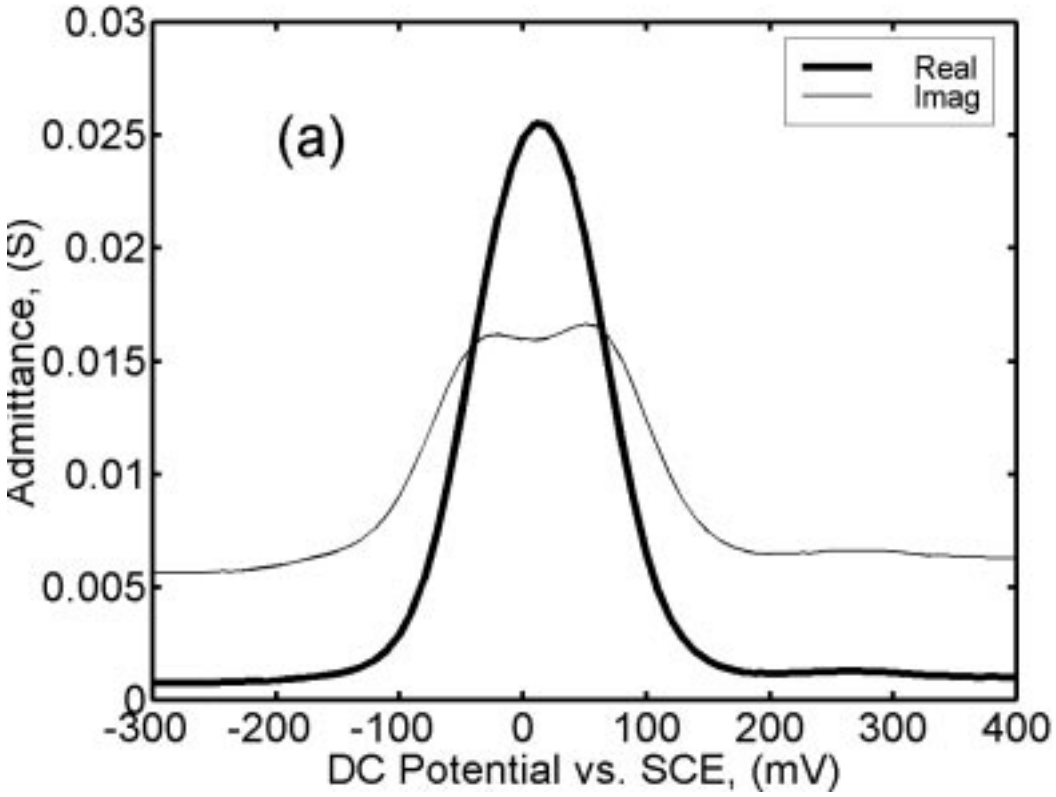

Figure 4.1 (b). Interfacial admittance for a C_7 SAM at f = 2200 Hz after correction for R_u = 18.8 Ω.

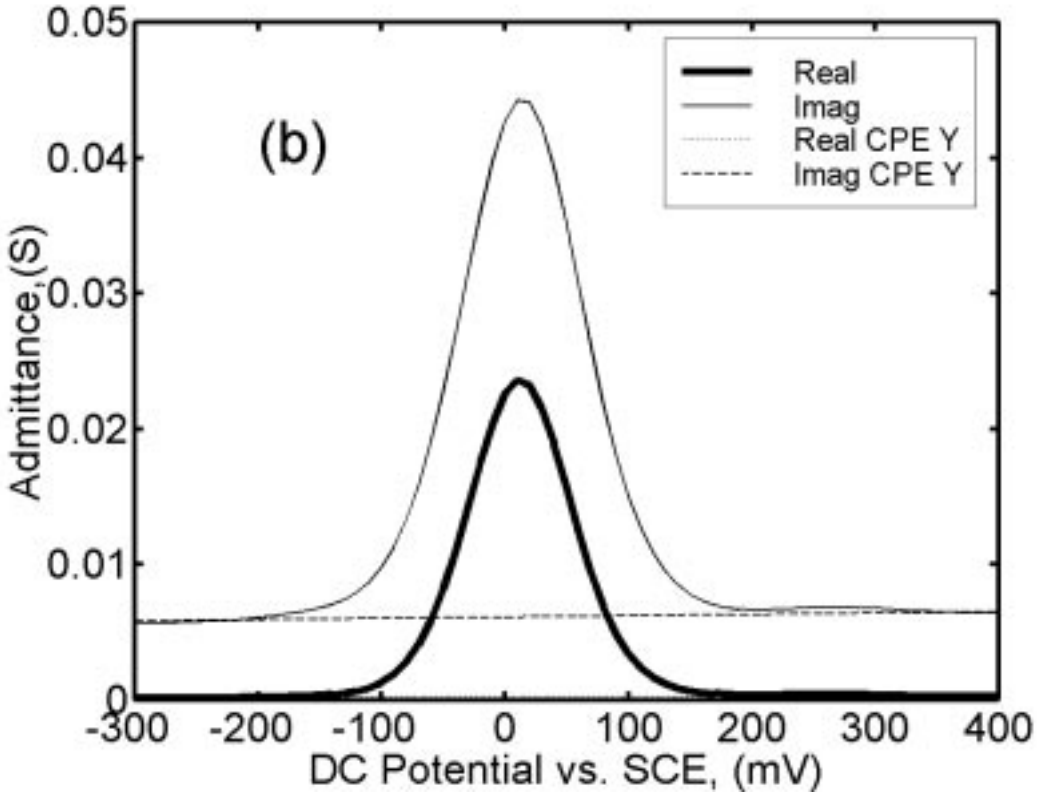

Figure 4.1 (c) Faradaic admittance for a C_7 SAM at f = 2200 Hz after baseline correction for CPE admittance. In contrast to 4.1 (a) and 4.1 (b), experimental data are shown as symbols in 4.1 (c). Theoretical fits over a DC potential range used for optimization are shown as lines in 4.1 (c).

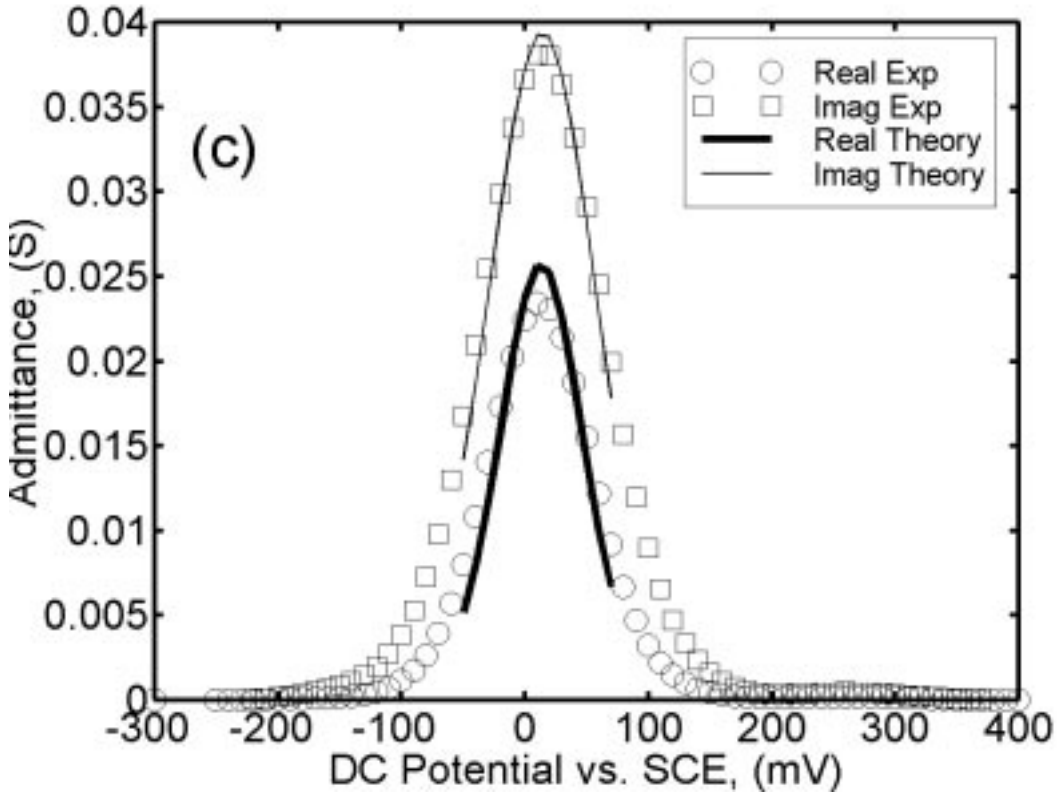

Figure 4.2. Faradaic admittance for a C_5 SAM at 81 Hz.

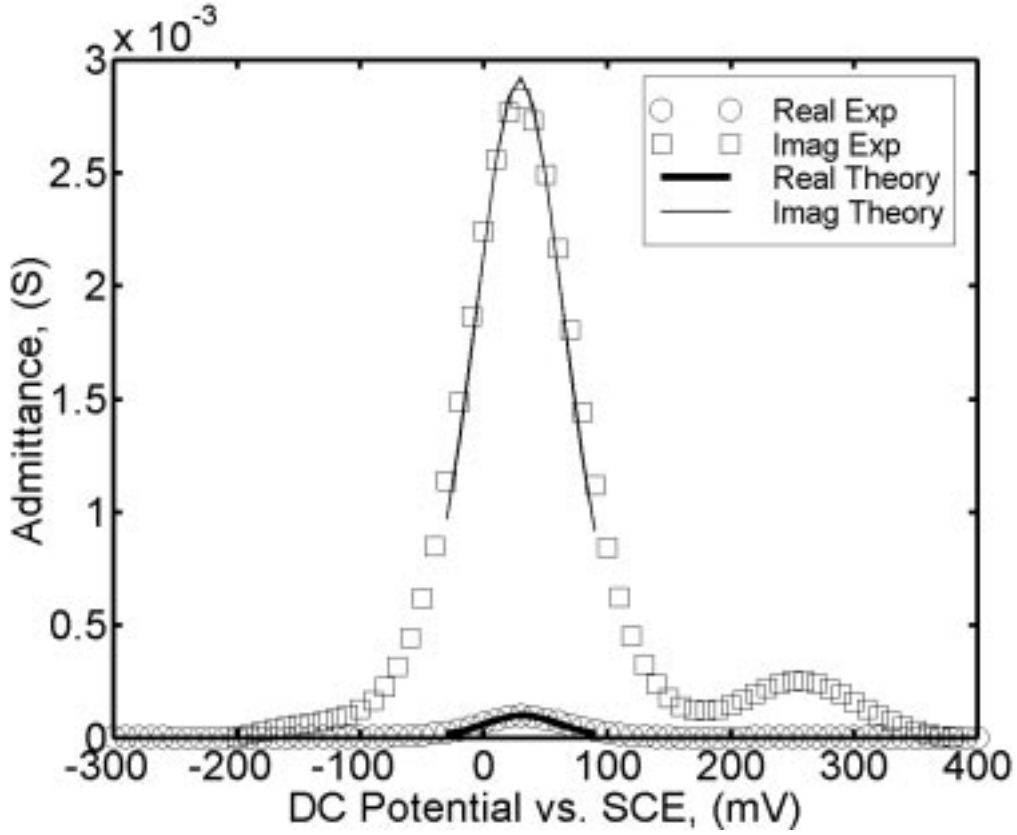

Figure 4.3. Cotangent of the $Y^{faradaic}$ phase for a C_7 SAM vs. angular frequency.

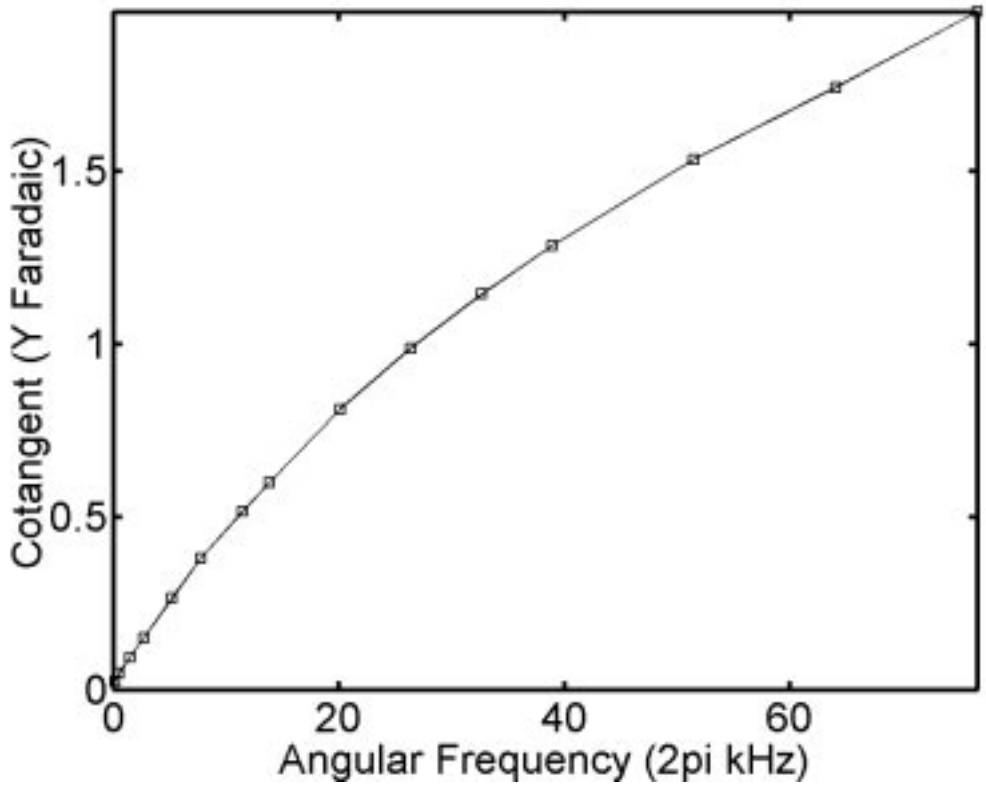

Figure 4.4. Cotangent of the $Y^{faradaic}$ phase for a C_5 SAM vs. angular frequency.

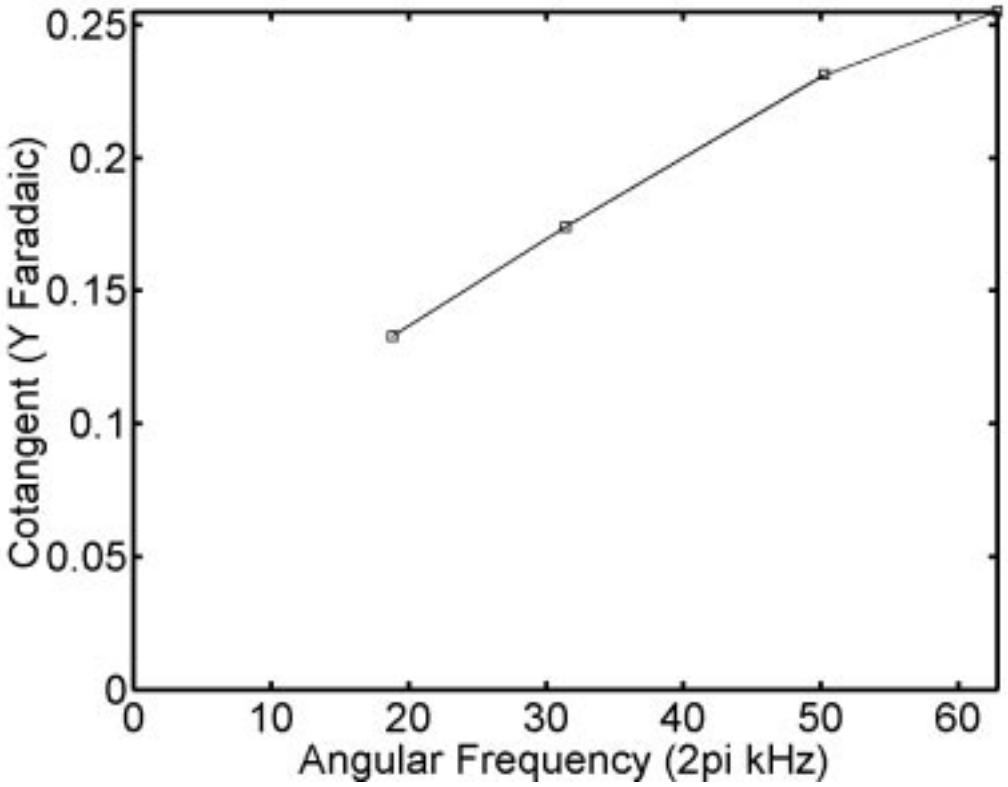

Figure 4.5. ln(k_s) vs. ***n*** (the number of methylene units). Linear regression results are: slope -1.2±0.1 and intercept 17.8±0.8.